

**Imaging and Probe Techniques for Wave Dispersion
Estimates in Magnetized Plasmas**

by

A. D. Light

B.A./B.S., Case Western Reserve University, 2005

A thesis submitted to the
Faculty of the Graduate School of the
University of Colorado in partial fulfillment
of the requirements for the degree of
Doctor of Philosophy
Department of Physics

2013

This thesis entitled:
Imaging and Probe Techniques for Wave Dispersion Estimates in Magnetized Plasmas
written by A. D. Light
has been approved for the Department of Physics

Prof. Tobin Munsat

Prof. Martin Goldman

Date _____

The final copy of this thesis has been examined by the signatories, and we find that both the content and the form meet acceptable presentation standards of scholarly work in the above mentioned discipline.

Light, A. D. (Ph.D., Physics)

Imaging and Probe Techniques for Wave Dispersion Estimates in Magnetized Plasmas

Thesis directed by Prof. Tobin Munsat

Fluctuations in magnetized laboratory plasmas are ubiquitous and complex. In addition to deleterious effects, like increasing heat and particle transport in magnetic fusion energy devices, fluctuations also provide a diagnostic opportunity. Identification of a fluctuation with a particular wave or instability gives detailed information about the properties of the underlying plasma. In this work, diagnostics and spectral analysis techniques for fluctuations are developed and applied to two different laboratory plasma experiments.

The first part of this dissertation discusses imaging measurements of coherent waves in the Controlled Shear Decorrelation Experiment (CSDX) at the University of California, San Diego. Visible light from ArII line emission is collected at high frame rates using an intensified digital camera. A cross-spectral phase technique allows direct visualization of dominant phase structures as a function of frequency, as well as identification of azimuthal asymmetries present in the system. Experimental dispersion estimates are constructed from imaging data alone. Drift-like waves are identified by comparison with theoretical dispersion curves, and a tentative match of a low-frequency spectral feature to Kelvin-Helmholtz-driven waves is presented. Imaging measurements are consistent with previous results, and provide non-invasive, single-shot measurements across the entire plasma cross-section. Relationships between imaging and electrostatic probe measurements are explored.

The second part of this dissertation discusses the design and construction of diagnostics for the Colorado Field-Reversed Configuration (CFRC), as well as preliminary results. A triple probe, a Mach probe, a multi-chord heterodyne interferometer, Rogowski coils, a single-point, three-axis magnetic probe, and a 16-point, three-axis magnetic probe have been constructed. Each diagnostic is designed for fluctuation measurements up to the data acquisition Nyquist frequency of 20 MHz.

A histogram cross-spectral analysis technique allows experimental dispersion estimates to be made from multi-channel magnetic measurements. Hints of waves in the range of ion-cyclotron frequency harmonics are observed, but lack of global information about the plasma objects formed in CFRC prevents definitive interpretation.

Dedication

To anyone who might find this work useful, and to the taxpayers who funded it.

Acknowledgements

You know who you are.

Contents

Chapter

1	Introduction and General Background	1
1.1	Overview and Organization of Dissertation	1
1.2	Spectral Density Estimation	2
1.2.1	Overview	2
1.2.2	Spectral Density	3
1.2.3	The Two-Point Technique	4
1.2.4	Two-dimensional Fourier Transform Technique	6
2	Imaging Measurements of Fluctuations in the Controlled Shear Decorrelation Experiment	7
2.1	Motivation	7
2.2	Theoretical Background	8
2.2.1	Instabilities in a Linear, Magnetized Plasma Column	8
2.3	CSDX-U Device	16
2.3.1	Overview	16
2.3.2	Device Hardware	17
2.4	Imaging Measurements of Coherent Modes	24
2.4.1	Cross-spectral-density Phase Mapping	24
2.4.2	Dispersion estimates from intensity	28
2.4.3	Implications for Dynamics	35

2.4.4	Discussion of Imaging Results	38
2.5	Relationship between Probe and Imaging Measurements	39
2.5.1	Intensity as a Proxy for Density	39
2.5.2	Correlations Between Intensity and Electrostatic Quantities	40
3	The Colorado FRC Experiment	51
3.1	Motivation and Overview	51
3.2	Theoretical Background	53
3.2.1	The Spheromak and the Woltjer-Taylor Relaxation Paradigm	53
3.2.2	The Field-Reversed Configuration - High β	55
3.3	Device and Diagnostics	61
3.3.1	Plasma Guns	62
3.3.2	Discharge Diagnostics	67
3.3.3	Plasma Diagnostics	69
3.3.4	CFRC Plasma Properties and Machine Status	89
3.4	Wave Measurements Using High-Resolution Magnetics	109
	Bibliography	118

Tables

Table

- 2.1 Comparison of partial derivatives of with respect to normalized electron temperature fluctuation amplitude. If the dynamics are adiabatic ($V_p \sim n_e$), the high sensitivity of $(\hat{V}_f - \hat{V}_p)$ to the temperature fluctuation level should make it obvious when temperature fluctuations cannot be neglected. 48

Figures

Figure

2.1	Illustration of the drift wave mechanism. (a) Initial conditions: An ion perturbation in the presence of a background magnetic field and density gradient. (b) The accompanying potential perturbation generates a local $E \times B$ circulation. (c) The $E \times B$ brings higher density towards one side of the perturbation and lower density to the other. (d) Thus the density perturbation propagates in the electron diamagnetic direction.	10
2.2	An annotated copy of Fig. 2 of Ref. 53, showing the points used for computation of the b parameter. A parabola fit to these points is used to extrapolate b values beyond $m = 5$	12
2.3	Time average profiles for plasma parameters. (a) Electron density and temperature profiles. The black solid line is a Gaussian fit to the density data (gray dots). (b) Measured plasma potential and resulting azimuthal $E \times B$ velocity.	17
2.4	Technical drawing of the CSDX device. Labeled distances are as follows: (a) Length of experimental section. (b) Axial distance from $z = 0$ to location of 4-tip probe. (c) Axial distance from location of 4-tip probe to end window (optical path length from the camera focal plane to the window). (d) Magnet spacing. (e) Diameter of experimental section.	18

2.5	Background axial magnetic field properties. (a) Axial profile of background magnetic field at $I_{\text{mag}} = 330$ A. (b) Calibration data for background magnetic field as a function of coil current. Uncertainties in measured values are within the size of the data markers for both (a) and (b).	20
2.6	(a) Layout of the electrostatic probe used for measuring fluctuations. The view is end on, from the center of the plasma column. Tips 2, 3, and 4 are in the same (radial) plane while tip 1 protrudes farther into the plasma (darker shading). This geometry allows radial and azimuthal electric fields to be estimated from differences in floating potential. (b) Photograph of the actual probe (side view), including stabilizer disk to ensure that the geometry remains fixed even if the probe stalk droops.	20
2.7	(a) Raw image example (single frame). White corresponds to zero intensity. (b) Normalized radial profiles of mean I_{488} (solid black), RMS I_{488} fluctuation amplitude (dashed black), and mean I_s (solid gray).	23
2.8	Time-average radial profiles of electron density (n_e), ion saturation current (I_s), and intensity (I_{488}). A Gaussian fit to the density is a convenient and reasonably accurate representation of the profile shape.	24
2.9	The average coherence spectrum of the plasma column compared with the average power spectrum. Error bars in the cross-spectral power are statistical uncertainty in the discrete CSD estimate. Note that the power spectrum is plotted on a logarithmic scale. (a)-(d) are the four most prominent peaks, corresponding to the phase maps in Fig. 2.10.	26
2.10	Sample phase maps for the four most prominent coherent modes. Vertical bars in Fig. 2.9 highlight the frequency component corresponding to each map, (a), (b), (c) and (d).	26
2.11	Standard-deviation maps (Eq. 1.6) corresponding to Fig. 2.10. Note that particularly asymmetric parts of the phase maps seem to coincide with high uncertainty.	26

- 2.12 (a) Time-average frame. (b) RMS frame. (c) Azimuthal variation at $r = 3$ cm for time-average (mean) I_{488} , RMS I_{488} , and the radial gradient (negative) of I_{488} . Intensity is normalized to its maximum value in the image sequence. 28
- 2.13 Normalized spectral density and measured dispersion relations at $r = 3$ cm from (a) 2D auto-spectral density of image data, (b) average of 32 two-point estimates from pixel data, (c) two-point floating-potential data (probe), and (d) two-point pixel data. The color scale for each plot indicates the power relative to the total spectral power at the given radius. White circles represent the maxima of the k-spectra for frequencies where the total spectral power is more than 1% above background. The dashed line in (a) represents the raw theoretical expectation [Eq. (2.16)] calculated from the profiles in Fig. (2.3). The hashed region in (a) indicates likely bounds for Doppler-shifted theory curves based on the $E \times B$ profile of Fig. 2.3(b). The solid line in each plot is the theoretical expectation including the best-fit Doppler shift for (a). 31
- 2.14 Comparison of dispersion estimates at various radii: (a) 2 cm, (b) 4 cm, and (c) 6 cm. The solid line is the theoretical curve from the Ellis model including the Doppler shift from the best-fit $E \times B$ velocity. Best fit values for $v_{E \times B}$ are $v_{\text{best}}(2 \text{ cm}) = 66 \text{ m/s}$, $v_{\text{best}}(4 \text{ cm}) = 222 \text{ m/s}$, $v_{\text{best}}(6 \text{ cm}) = 49 \text{ m/s}$. White circles represent the maxima of the k-spectra for frequencies where the total spectral power is more than 1% above background. The dashed line in (c) is the Kelvin-Helmholtz dispersion curve calculated from Eq. (2.17). 33
- 2.15 Frequency spectra of image sequences filtered in mode number, demonstrating shared frequency content. Shaded regions (a), (b), and (c) correspond to the frequency pass bands used for for the filtered sequences in Fig. 2.16. 36

2.16	Time evolution of $m = 2$ image component with various frequency filters applied. The rows (a,b,c) correspond to the pass-bands around the peaks distinguished in Fig. 2.15. The color scale for each mode is normalized to the maximum intensity value in the entire image sequence.	37
2.17	Examples of the correlation between I_s and visible light in previous experiments. (a) Time series in the Mirabelle device (Fig. 3 of Ref. 38). (b) Correlation functions in the Mirabelle device (Fig. 4 of Ref. 38). (c) Time series in the original CSDX source (Fig. 2 of Ref. 33). (d) Correlation functions in the original CSDX source (Fig. 2 of Ref. 33). (a)-(b) reprinted with permission from S. Oldenbürger, C. Brandt, F. Brochard, N. Lemoine, and G. Bonhomme, Review of Scientific Instruments, 81, 063505 (2010). Copyright 2010, AIP Publishing LLC. (c)-(d) reprinted with permission from G. Y. Antar, J. H. Yu, and G. Tynan, Physics of Plasmas, 14, 022301 (2007). Copyright 2007, AIP Publishing LLC.	41
2.18	Comparison of (a) I_{488}/I_s and (b) I_{488}/V_f time-lag correlation functions at $r = 3.0$ cm. Data is taken over a small radial range because the probe is moving. This correlation calculation uses approximately 3000 time points covering nearly 60 ms.	42
2.19	I_{488}/I_s time-lag correlation functions across the plasma radius. Pixels are chosen to match the probe radial position for each radial bin of width 1 mm. The time-average normalized I_s profile is shown at left for comparison.	42
2.20	I_{488}/V_f time-lag correlation functions across the plasma radius. Pixels are chosen to match the probe radial position for each radial bin of width 1 mm. The time-average normalized $-V_f$ profile is shown at left for comparison.	43
2.21	Image sequence showing fluctuations with coherent spatial structure in the [7.6, 7.9] kHz band.	44
2.22	Radial fluctuation amplitude profiles for visible light and probe quantities (shot label 12228).	45

2.23	Comparison of (a) I_s and (b) I_{488} frequency spectra at various radii. The innermost radial trace is not shifted, while each successive radial trace is shifted downward by a factor of ten to allow all traces to be visible.	45
2.24	Comparison of experimental intensities with collisional-radiative model for the relevant 488-nm argon line (reproduced from Fig. 6.11 of Ref. 85). Note that temperatures are normalized to 3 eV.	48
2.25	Finite difference estimate of emission sensitivity to electron temperature derived from Fig. 6.11 of Ref. 85.	48
2.26	Comparison of time-lag correlation functions for field-aligned probe tips at $r = 2.9$ cm.	50
3.1	Sketch of a spheromak flux surface and accompanying field lines.	53
3.2	Diagram of FRC magnetic field structure in cylindrical geometry.	56
3.3	Illustration of counter-helicity merging. (a) Two spheromaks are launched towards the center of the chamber, with the same poloidal field direction but opposing toroidal fields (indicated by orange and blue shading). (b) The outer flux surfaces reconnect, creating a new poloidal flux surface around the remaining private flux regions and annihilating toroidal field. (c) The reconnection process proceeds, heating the ions (primarily) and establishing a new equilibrium. (d) When the merging process is complete, the toroidal field has been completely annihilated, leaving a purely poloidal field.	60
3.4	CAD cross-section of vacuum vessel showing dimensions of coaxial guns and diagnostic ports.	61

3.5	Illustration of plasma gun operation [after Ref. 126, Fig. 4]. (a) Gas is puffed into the gap between the cylindrical conductors and a high voltage is applied. (b) Arc breakdown occurs, forming plasma that carries a radial current. The plasma is pushed along the gun by the magnetic pressure of the field generated behind the current ($J \times B$ force). (c) The plasma is pushed out of the gun, and the stuffing fields are distended by the induced currents in the plasma being ejected. (c) Distended flux reconnects around plasma and a detached spheromak is formed (reconnected fields now supported by plasma currents).	62
3.6	Circuit diagram for gas valve driver.	65
3.7	Circuit diagram for capacitor bank operation.	66
3.8	Photograph of a Rogowski coil built for measuring the plasma gun current.	69
3.9	Schematic for triple Langmuir probe measurements.	70
3.10	Circuit for measuring triple probe quantities in CFRC. The probe tips are labeled “ V_+ ”, “ V_- ”, and “ V_f ”, according to convention. The actual quantities measured are labeled V_+ , V_s , and V_f , proportional to positive-bias potential, ion saturation current, and floating potential (respectively).	71
3.11	Frequency response curves for the key components of the triple probe circuit. Phase measurements also show the data with a linear fit subtracted, since the inherent time delay in the circuit will give a linear phase lag as the frequency increases. (a) Gain and (b) phase response for the I_s toroid. (c) Gain and (d) phase response for a representative capacitive voltage divider.	72
3.12	Photograph of the triple probe assembly.	72
3.13	Mach probe bias and signal collection circuit. A detail of the transformer connection to the digitizer is shown for one tip. The other three tips use identical transformer arrangements.	74
3.14	Photograph of the Mach probe head.	75

3.15	Optical table layout, courtesy of L. Ellison. a)CO ₂ laser. b)40MHz acousto-optic modulator. c)Set of reference beam splitters. d)Set of measurement beam splitters. e)Diagonal array of beam recombining optics. f)Periscope beam-steering elements . . .	78
3.16	3D SolidWorks model of interferometer, courtesy of L. Ellison.	79
3.17	a) CAD drawing of Macor stalk showing arrangement of winding holes. b) Complete probe head.	82
3.18	O-ring seal for connecting glass envelope to stainless tube.	83
3.19	Diagram of aluminum support structure and linear actuator.	84
3.20	a) Fast amplifier circuit diagram. The theoretical gain is approximately five with a bandwidth of 100 MHz. b) Gain and phase lag versus frequency for a typical amplifier.	85
3.21	Calibration data for a single $3\mu H$ coil.	86
3.22	Comparison of magnetic field traces for a single triplet of coils at $r = 27$ cm (a)-(c) before and (d)-(f) after isolating the channel grounds from each other. The signals in the first column are dominated by pickup from the discharge current (cf. Fig. 3.26).	88
3.23	Photograph of single B-dot probe installed in machine.	89
3.24	Calibration data for a single 8-turn coil.	90
3.25	Matrix of possible merging arrangements for CFRC. Each diagram indicates poloidal (in-plane) and toroidal (out-of-plane) fields. Only the final object is indicated for cases where merging is expected.	91
3.26	Typical waveforms of the current (a) for the stuffing flux magnet and (b) for the gun discharge. The stuffing flux is approximately constant on the timescale of the gun. The stuffing flux current appears quantized because the amplitude of the signal is only ~ 10 digitizer bits peak-to-peak (Rogowski coils designed for the high current in the guns).	92
3.27	Most recent interferometer traces, demonstrating shot-to-shot variation in line-integrated density during seven identical, consecutive shots.	92

3.28	Magnetic field traces for one channel of the 48-channel probe array located at $r = 23.4 \text{ cm} = 0.6r_w$ in the midplane. Three consecutive shots at the same parameters are shown and field components are labeled in cylindrical (chamber) geometry. . . .	93
3.29	Time-lag correlation function for toroidal field measurements separated by 45.5 cm. Positive delay indicates that the probe farther from the gun receives the signal later in time.	94
3.30	Comparison of spheromak launch threshold with plasma density. (a) Calculated spheromak eigenvalue, $\lambda(t)$. The dashed horizontal line represents the threshold gun value, $\lambda_c = 20.1 \text{ m}^{-1}$, calculated in Section 3.3.1. The dotted horizontal line represents the threshold value calculated for the chamber outside the gun, $\lambda_w = 10.2 \text{ m}^{-1}$. Dashed and dotted vertical lines indicate where $\lambda(t)$ exceeds each threshold as it increases in time. (b) Line-integrated density, shifted by the propagation time calculated from Figure 3.29. Density increases seem to coincide with eigenvalue threshold crossings.	95
3.31	Magnetic traces in the midplane for $r = 27.4 \text{ cm}$. Data may be consistent with formation of a flipped spheromak equilibrium.	97
3.32	Magnetic traces in the midplane for $r = 27.4 \text{ cm}$. The abrupt change in the azimuthal field direction near $t = 95 \mu\text{s}$ may indicate the formation of a second spheromak. . .	98
3.33	Projection of magnetic field in the r - z plane as a function of time and radius. The abrupt flip of both components near $t = 50 \mu\text{s}$ is present along the length of the probe. The axial field is not observed to reverse as a function of position, suggesting that the probe does not cross the magnetic axis.	99
3.34	Projection of magnetic field in the r - ϕ plane as a function of time and radius. The field evolution appears nearly uniform over the measured radii.	100

- 3.35 Evolution of line-average density for two-gun discharge (merged). (a) Time evolution of λ for west gun. (b) Time evolution of line-integrated plasma density. A trace for a single-gun discharge using the same gun parameters is shown for contrast in light gray. Merged timestamp = 'dt2009.10.27_hr14.18', single-gun timestamp = 'dt2009.10.27_hr11.22'. 102
- 3.36 Magnetic traces in the midplane for $r = 27.4$ cm. The lighter (grey) trace in (a) shows the λ value for the second gun. In the time period shortly after $t = 150 \mu\text{s}$ axial field (b) increases while the azimuthal field (c) decays, indicating a possible FRC-like object with zero toroidal (azimuthal field) but finite poloidal (radial/axial) field. 103
- 3.37 Projection of magnetic field in the r - z plane as a function of time and radius. The rotation of \mathbf{B} near $t = 125 \mu\text{s}$ varies strongly along the probe. Both the radial variation and the fast temporal scale for the motion suggest that a localized magnetic structure is passing by the probe. The increase in B_z after $t = 150 \mu\text{s}$ may indicate the formation of a merged object. 104
- 3.38 Projection of magnetic field in the r - ϕ plane as a function of time and radius. The change in B_r near $t = 125 \mu\text{s}$ is again visible, but B_ϕ is more or less uniform in radius. The strong reduction of B_ϕ just after $t = 150 \mu\text{s}$ may indicate annihilation of toroidal field. 105
- 3.39 Evolution of (a) line-average density, (b) local magnetic energy density, and (c) plasma β . The temperature used for estimating β is 10 eV. Density timestamps = 'dt2010.02.15_hr + ['14.30', '14.35', '14.39', '14.51', '14.56', '15.05', '15.12', '15.17', '15.21', '15.31']. Magnetic timestamps = 'dt2010.11.02_hr' + ['11.17', '11.35', '11.45', '12.15', '12.54']. 106
- 3.40 Evolution of (a) line-average density, (b) local magnetic energy density, and (c) plasma β . The temperature used for estimating β is 10 eV. Density timestamps = 'dt2009.10.27_hr' + ['10.34', '10.38', '10.41', '11.22', '11.25', '11.28', '11.31']. Magnetic timestamps = 'dt2010.09.28_hr' + ['10.27', '10.30', '10.33', '10.40', '10.44', '10.48']. 108

- 3.41 Spectral intensity plot demonstrating fluctuations suggestive of ion-cyclotron-harmonic or ion Bernstein waves. The time frame used is $[130,210] \mu\text{s}$ 113
- 3.42 Comparison of spectral intensity derived from different time windows. (a) Line-average density trace. The vertical dashed line indicates the onset time of the density rise in (a)-(c). (b) Intensity plot of raw $\partial_t B_\phi$ data surrounding a single magnetic ‘event’. Hashed regions indicate the two different time blocks used for spectral intensity calculations. (c) Zoomed in plot of data during the event. (d) Spectral intensity derived from a time window centered on the event, $t = 93 - 153 \mu\text{s}$ (45° hash). (e) Zoomed in plot of data after signature of propagating structure subsides. (f) Spectral intensity derived from a time window including only the latter part of the event, $t = 131 - 191 \mu\text{s}$ (135° hash). 115
- 3.43 Comparison of spectral intensity plots using (a) only the outer 8 channels and (b) only the inner 8 channels. The time frame used is $[130,210] \mu\text{s}$. The feature with harmonic features in the ion-cyclotron frequency range is localized to the inner half of the probe. 117

Chapter 1

Introduction and General Background

1.1 Overview and Organization of Dissertation

This dissertation describes work from two distinct projects, related by the theme of spectral analysis. Fluctuations are a ubiquitous feature of plasma systems, both in nature and in the laboratory. Of particular interest are fluctuations that correspond to linear waves, since these can be described by a characteristic dispersion relation. The major contribution of this work is the development and application of techniques to measure dispersion properties experimentally.

Chapter 2 discusses the measurement of fluctuation using high-frame-rate visible-light imaging in the Controlled Shear Decorrelation Experiment (CSDX) at the University of California, San Diego. CSDX produces a cold ($T_e \sim 3 \text{ eV}$), dense ($n_e \sim 10^{18} \text{ m}^{-3}$), plasma column in a static solenoidal background field using a helicon source. The details of the experiment and imaging system are described, and a technique for measuring two-dimensional spectral density is elaborated. The technique is validated in the case of previously-identified electron drift waves, and a new type of fluctuation is observed. We present a tentative identification of these new modes with the Kelvin-Helmholtz instability. A discussion of the strengths and weakness of visible light as a representation of plasma fluctuations is provided in the context of comparison with probe measurements.

Chapter 3 discusses the construction and preliminary results from the Colorado Field-Reversed Configuration experiment (CFRC). CFRC is a merged-spheromak device designed to produce prolate field-reversed configurations (FRCs). Work performed towards the completion of this dissertation includes development and construction of pulsed-power hardware, high-vacuum compo-

nents, plasma diagnostics, data acquisition software, and analysis software. Preliminary results are given for operational diagnostics, and two-dimensional spectral densities are calculated from multi-channel magnetic measurements. For future reference, ‘status notes,’ describing the state of current hardware and any known issues, are included for most of the sections in this chapter.

Work on both experiments makes heavy use of two-dimensional spectral-density estimation, so an overview is given next to orient the reader.

1.2 Spectral Density Estimation

1.2.1 Overview

It is increasingly apparent that waves and fluctuations play a central role in many plasma phenomena, especially for confinement of laboratory plasmas. Waves in plasma are often presented as a complicated ‘zoo’ of solutions to the combined Maxwell-plasma system of equations. Although the complexity of this zoo can be intimidating [1], the ubiquity of waves in both natural and laboratory settings is a rich diagnostic opportunity. In this thesis, ‘fluctuation’ is taken to mean any departure from an average value (defined as appropriate in each particular situation) in the sense of a Reynolds decomposition [2]: $x = \langle x \rangle + \tilde{x}$. The term ‘wave’ is reserved for fluctuations that have characteristic frequencies for a given wavelength. This means that a wave obeys a dispersion relation, $\omega(\mathbf{k})$. The definition of a particular wave incorporates the plasma model employed as well as the approximations and limits used to obtain a solution for the dispersion relation. As such, an experimental measurement of a dispersion relation allows both identification of a class of waves and a direct check on the validity of various approximations ¹.

Experimental measurement of dispersion curves is not a well-defined task; to the best of our knowledge, it has not been attempted previously in a plasma context. For the purposes of this dissertation, we define a ‘measured’ dispersion relation as a map of the spectral power of fluctuations as a function of both frequency and wavenumber. In the case where multiple modes on a given dispersion branch are unstable or excited, spectral power is localized along the relevant

¹ See, for example, the discussion of the drift-wave dispersion relation in Section 2.4.2.

dispersion curve. Although the techniques described may operate effectively in other situations, for the following discussion we assume that multiple modes are oscillating and that the plasma is not (fully) turbulent. This section gives an overview of two techniques used for estimating two-dimensional spectral densities, with the goal of measuring dispersion relations.

1.2.2 Spectral Density

There are various (equivalent) ways of defining the spectral density (SD) in the case of discretely-sampled signals, but we choose the Fourier transform method for its clarity and ease of implementation. The calculation proceeds as follows [3]: Two time series $x(t_j)$ and $y(t_j)$ of length $T = N\Delta t$ are sampled at points $t_j, j = 0, 1, \dots, N$ and transformed into the frequency domain using a fast Fourier transform (FFT). The resulting amplitudes $X_i(f_j)$ and $Y_i(f_j)$ are multiplied together to construct a raw estimate of the SD at each frequency f_j :

$$G_{xy}(f_j) = C_j X^*(f_j) Y(f_j). \quad (1.1)$$

If $x(t_j)$ and $y(t_j)$ are the same signal, G_{xx} is called the autospectral density (ASD) and represents the power in each Fourier mode contributing to the signal. In this case, $C_j = 2/T$ for $j = 1 \dots N/2 - 1$ and $C_j = 1/T$ for $j = 0, N/2$ (the factor of two overcounts for first and last points if the signals are the same). If $x(t_j)$ and $y(t_j)$ are distinct, G_{xy} is called the cross-spectral density (CSD) and represents the power in *shared* frequency content. In this case, $C_j = C = 2/T$ for all j .

This single estimate of spectral density is not sufficient for quantitative measurements. In fact, if each time series is modeled as a Gaussian random variable, the relative statistical uncertainty in G_{xy} is unity[3]. In order to recover a ‘smooth’ estimate of the true spectrum, a number of raw estimates are typically averaged together. When a true ensemble of repeated measurements is unavailable, the signals for each raw estimate can be constructed by either dividing $x(t_j)$ and $y(t_j)$ into shorter time records (for signals with time-stationary statistics), or using simultaneous signals separated in space (for a spatially uniform system). For evenly sampled data, a straight average across estimates is appropriate. For unevenly sampled data, histogramming provides the required

smoothing. Using an ensemble of n_d distinct measurements of $x(t_j)$ and $y(t_j)$, the smooth estimate is defined to be:

$$\hat{G}_{xy}(f_j) = \frac{C_j}{n_d} \sum_{i=1}^{n_d} X_i^*(f_j) Y_i(f_j). \quad (1.2)$$

where i is the index of each raw estimate. The relative statistical uncertainty in the spectral power given by a discrete ASD estimate is $1/\sqrt{n_d}$, where n_d is the number of distinct estimates in the ensemble. For the CSD[3], the relative uncertainty is $1/|\gamma_{xy}|\sqrt{n_d}$, where γ_{xy} is the cross coherence of the smoothed estimate:

$$\gamma_{xy}^2(f_j) = \frac{|\hat{G}_{xy}(f_j)|^2}{\hat{G}_{xx}(f_j)\hat{G}_{yy}(f_j)} \quad (1.3)$$

The spectral density technique described thus far are functions of frequency, but yield no wavenumber information. In order to extract information about the spatial structure of fluctuations in addition to frequency information, time series data from multiple locations is required. In the following sections, we describe the details of the two techniques implemented in Chapters 3 and 2 to obtain two-dimensional spectral density estimates (functions of both ω and k).

1.2.3 The Two-Point Technique

Many studies over more than 25 years [4, 5, 6, 7, 8, 9, 10, 11, 12, 13, 14, 15] have used probe pairs to estimate the wavenumber spectrum and statistical dispersion relation [16] for plasma fluctuations. The ‘‘two-point technique’’ estimates the power spectral density, $s(k, \omega)$, using a conditional wavenumber spectral density, $s(K|\omega) = S(K, \omega)/S(\omega)$, where K is the local estimate of the wavenumber. This approximation holds under the condition that the fluctuations being measured can be represented by a superposition of wave packets[16]. The procedure involves calculating the cross-phase between two signals with known spatial locations. The CSD defined by equation (1.2) is a complex quantity, and the cross-phase as a function of frequency is given by the phase angle of $\hat{G}_{xy}(f_j)$:

$$\tan\phi_{xy} = \text{Im} \hat{G}_{xy} / \text{Re} \hat{G}_{xy}. \quad (1.4)$$

For two probe signals (time series), a local wavenumber can be calculated for each frequency

by dividing the cross-phase by the separation between the probe locations \mathbf{r}_x and \mathbf{r}_y :

$$K_l = \frac{\phi_{xy}}{(\mathbf{r}_x - \mathbf{r}_y)_l}. \quad (1.5)$$

The spacing of the probe tips must be smaller than the true wavelength of the fluctuations to avoid aliasing. For one pair of time-series, the above method produces a single K value at each frequency f_j . This limitation means that only the **average** K (power-weighted) and its uncertainty is measured. The statistical uncertainty in K comes from the uncertainty in the cross-phase (disregarding position and other measurement uncertainties), and is an estimate of the spectral width:

$$\sigma_\phi = \frac{(1 - \gamma_{xy}^2)^{1/2}}{|\gamma_{xy}| \sqrt{2n_d}} \quad (1.6)$$

For a single coherent wave, or a collection of coherent waves all lying on a single-valued dispersion curve, interpretation of $K(f_j)$ is straightforward. In cases where multiple bands of coherent fluctuations are present in the (k, ω) plane, the average K value may not describe any of the fluctuations present. In a turbulent case, K and σ_ϕ provide limited information about the location of the fluctuations in spectral space and the width of the spectrum, respectively.

Alternatively, the local wavenumber at each frequency can be calculated from each raw CSD estimate, rather than from the smooth estimate. The resulting ensemble of $(|G_{xy}|, K, \omega)$ triplets are then assembled into a histogram, summing the power in each bin (K_m, f_j) and dividing by n_d . Construction of the histogram is analogous to the ensemble averaging discussed above and produces a smooth estimate $\hat{H}_{xy}(K_m, f_j)$. Although the histogram technique provides a two-dimensional result, it still reflects only the mean K and spectral width at each frequency. This is a fundamental limitation of using only two measurement locations; a single pair can provide only two constraints on the spatial properties. A little-cited work by Carlson [17] illustrates this by calculating the distribution of K values for fluctuations in the Gaussian random-phase model. The two point estimate of $\hat{G}(K) = \sum_\omega \hat{G}_{xy}$ always drops off as K^{-5} for fluctuations represented by Gaussian random variables, independent of K and σ_ϕ [17]. Thus, although $\hat{H}_{xy}(K_m, f_j)$ seems to contain information on the shape of the wavenumber spectrum, this is in fact an artifact of the technique used to construct the estimate.

In order to circumvent this limitation, multiple probe pairs with unequal spacing can be employed. Carlson discusses this in terms of the “orthogonality” or independence of cross-spectra from sets of probe measurements. Under the spatially-uniform, time-stationary assumptions that lend validity to the two-point technique, \hat{G}_{xy} is only a function of the separation $|\mathbf{r}_x - \mathbf{r}_y|$ [17]. Using multiple probe pairs with the same spacing improves the estimates of K and σ_ϕ , but does not give more information on the the shape of the K spectrum. Thus, in order to extract a fully two-dimensional spectral density estimate, multiple pairs of signals with distinct spatial separations must be employed. Implementation of a multi-point histogram technique for estimates of the spectral density of magnetic fluctuations is discussed in Chapter 3.

1.2.4 Two-dimensional Fourier Transform Technique

In the case where fluctuations are well-sampled in both time and space, such as with imaging or large arrays of probes, the histogram technique is unnecessary. Each estimate of the spectral density can simply be extended by performing the FFT along both the time and space dimensions. A single raw estimate is now defined from the two-dimensional transforms of $x(t_j, r_l)$ and $y(t_j, r_l)$ as

$$\hat{G}_{xy}(f_j, k_l) = C_j X^*(f_j, k_l) Y(f_j, k_l) \quad (1.7)$$

where the signals are now functions of (discrete) position r_l , and $k_l = 2\pi l/N\Delta r$ indicates the corresponding spatial Fourier component (wavenumber). A smooth estimate is obtained by averaging, since each estimate in the ensemble has the same length (by construction). The smooth two-dimensional CSD is thus given by:

$$\hat{G}_{xy}(f_j, k_l) = \frac{C_j}{n_d} \sum_{i=1}^{n_d} X_i^*(f_j, k_l) Y_i(f_j, k_l) \quad (1.8)$$

Chapter 2

Imaging Measurements of Fluctuations in the Controlled Shear Decorrelation Experiment

2.1 Motivation

One of the most useful features of imaging is the ability to measure a two-dimensional array of signals simultaneously. The advent of commercially available fast-framing digital cameras has opened the possibility of imaging studies using visible light in small, low-temperature laboratory plasma experiments, where diagnostics such as microwave imaging reflectometry [18], electron cyclotron emission imaging (ECEI) [19], and beam emission spectroscopy [20] are impractical. Many studies have used visible fast-imaging techniques in both qualitative and quantitative measurements of spatial structure and plasma motion in tokamaks and stellarators [21, 22, 23, 24, 25, 26, 27, 28, 29, 30, 31], basic confinement machines [32, 33, 34, 35, 36, 37, 38, 39, 40, 41, 42], and other plasma devices [43, 44, 45]. The conventional method of measuring spatial properties of fluctuations in low-temperature plasma uses the phase lag between multiple probe tips to estimate the size and velocity of structures moving past [16], as discussed in Sections 1.2.3 and 3.4. This procedure is robust for sufficient record length and stationarity, but a single pair of probes can provide only limited information [17]. Global measurements using many probes are possible [10, 46, 47], but limited port space and probe-induced perturbations [43] are severe obstacles to making measurements of this kind. Visible-light imaging, on the other hand, is non-perturbative, can have broad spatial coverage, and can be robust to asymmetries when the full cross-section of the plasma is imaged (as in this study). The major limitation of imaging is the absence of a formulaic link across param-

eter regimes between visible light fluctuations and plasma property fluctuations. Nevertheless, if the fluctuations at hand influence a property on which light emission depends (e.g. temperature, density, etc.), we can extract their spectral properties using imaging.

In this chapter, we present a study of the spectral properties of low-frequency modes in a linear, magnetized plasma column using fluctuation data from fast imaging in the Controlled Shear Decorrelation eXperiment - Upgrade (CSDX-U)[48]. We also construct a detailed comparison between imaging and probe measurements of fluctuations, including temporal, spatial, and spectral properties.

2.2 Theoretical Background

2.2.1 Instabilities in a Linear, Magnetized Plasma Column

The classes of fluctuations naturally present in a plasma often correspond to the sources of free energy that may be tapped by perturbations. A brief overview of relevant plasma instabilities is given here to provide context for the analysis presented in Sections 2.4 and 2.5. The current work is focused on the dispersion of steady, saturated fluctuations. Therefore, the real frequency is generally of more interest than the growth rate. Where dispersion relations are given, the frequency is denoted by ω , the wavenumber by k , and the growth rate by $\gamma = \text{Im } \omega$. For the purposes of comparison with CSDX-U, we consider a cylindrical plasma column (r, θ, z) immersed in a uniform magnetic field aligned with the column axis ($\mathbf{B} = B\hat{z}$). We assume that both ions and electrons are magnetized to a significant degree ($\omega_{ci,ce} > \nu_{\text{coll}}$). Centrally-peaked density and electron temperature profiles are common, and are assumed here for simplicity. The plasma β is typically below 0.1% in CSDX, so that an electrostatic treatment ($\mathbf{E} = -\nabla\phi$) is sufficient to capture the relevant physics. Ions are treated as cold ($T_i = 0$), and the plasma is collisional (no resonant particles). Because the plasma is weakly ionized in the edge region [49], we include collisions with neutrals where relevant. In keeping with observations in the device, we look for fluctuations with low frequencies ($\omega \ll \omega_{ci} \ll \omega_{ce}$), and assume long parallel wavelengths ($k_z \sim 0$). Equations of motion for fluctuations in a two-fluid

description under the above assumptions yield terms for four instability mechanisms [50, 51, 52]: Electron drift [53], Simon-Hoh [54, 55], Centrifugal Rayleigh-Taylor [50, 51], and Kelvin-Helmholtz [50, 51].

2.2.1.1 Collisional Electron Drift Instability

The drift instability consists of transport-inducing density and potential perturbations driven by a pressure gradient. It is often termed the “universal instability,” because it is nearly ubiquitous in laboratory plasma devices [56]. Indeed, drift waves are observed routinely in CSDX [57].

As described in many texts and reviews (see, for example, Refs. [58, 59]), the physical mechanism for drift waves involves $E \times B$ advection of particles across a pressure gradient (taken to be in the vertical direction for this illustration). Because CSDX is cold and the temperature profile is rather flat (see Figure 2.3a), we neglect the contributions from any temperature gradient. The wave exists in the frequency range where the phase velocity is much faster than the ion thermal speed and much slower than the electron thermal speed: $kv_{ti} \ll \omega \ll kv_{te}$. Boltzmann response means that electron density and electrostatic potential fluctuations are proportional (in-phase). The electron motion is primarily along the field lines on the time scale of the wave. The lowest-order response for the ions is the $E \times B$ drift, since they are considered to be cold (no parallel motion on the timescale of the wave). As illustrated in Figure 2.1a-b, a localized increase in electron density causes an $E \times B$ advective cell to form. Because of the density gradient, fewer particles are advected into the right edge of the perturbation than are advected into the left edge (Figure 2.1c). The increase in ion density on the left edge of the cell increases corresponds to a proportional change in electron density and thus potential. Thus, the initial perturbation propagates in the electron diamagnetic direction due to the combination of parallel electron motion and perpendicular ion motion (Figure 2.1d).

If the electron response deviates from the in-phase Boltzmann dynamics described above, drift waves can become unstable. In particular, if the electron parallel motion is inhibited by collisions (among other effects), the potential perturbation lags behind the density perturbation.

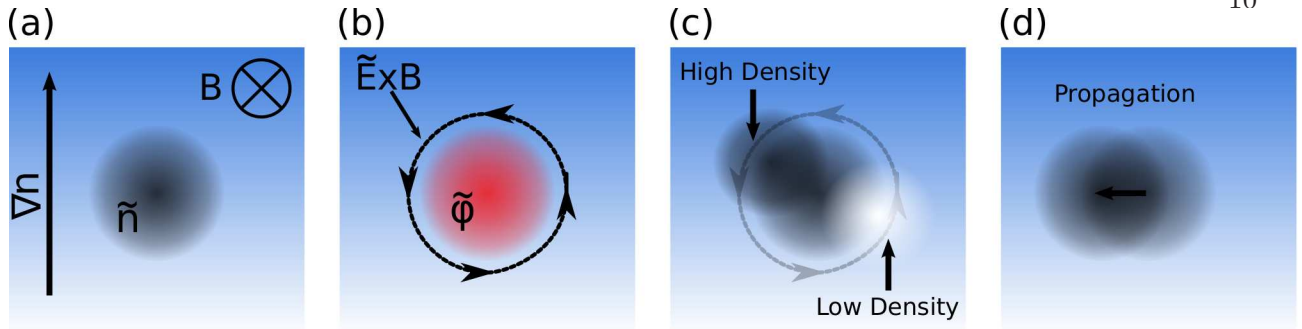


Figure 2.1: Illustration of the drift wave mechanism. (a) Initial conditions: An ion perturbation in the presence of a background magnetic field and density gradient. (b) The accompanying potential perturbation generates a local $E \times B$ circulation. (c) The $E \times B$ brings higher density towards one side of the perturbation and lower density to the other. (d) Thus the density perturbation propagates in the electron diamagnetic direction.

With proper phasing (a lag of $0 < \delta\phi \lesssim \pi/4$), $E \times B$ advection is still moving high-density fluid elements into the space at the edge of the original perturbation when the peak of the perturbation arrives there. Thus, the initial disturbance both propagates and is continually reinforced by the influx of particles from the high-density side of the gradient.

In a slab geometry, the dispersion relation can be derived in a two-fluid treatment [58]. Here, the static magnetic field is along \hat{z} , the density variation is along \hat{x} , and \hat{y} is the direction of propagation. Retaining the ion polarization drift in addition to the $E \times B$ drift allows this model to capture finite-Larmor-radius (FLR) effects to some degree. Since the ion Larmor radii are on the order of the wavelengths we observe in CSDX, this correction is necessary. The real frequencies for drift waves in this model are given by [58]

$$\omega = \frac{\omega_*}{1 + k_y^2 \rho_s^2}, \quad \text{where } \omega_* = k_y v_{de} = k_y \frac{k_B T_e}{eB} \frac{1}{n} \frac{\partial n}{\partial r}. \quad (2.1)$$

The two relevant scales are the ion sound gyroradius, $\rho_s = \sqrt{T_e/m_i \omega_{ci}^2}$, and the density gradient scale length, $L_n^{-1} = \frac{1}{n} \frac{\partial n}{\partial r}$. For $k_y \rho_s \ll 1$, the phase speed of the wave is the electron diamagnetic velocity, v_{de} .

In the steady-state plasma produced by CSDX, observed drift waves are saturated. This means that the imaginary part of the dispersion relation (growth rate) is less useful for comparing

with experiment. It is, however, useful to note whether there is a maximum growth rate, and for what value(s) of k it occurs. A peak in the growth rate generally predicts the modes most likely to appear in an experimental context, since the fastest-growing modes can use up the available free energy before slower-growing modes become large. For the slab model, the imaginary part of the drift dispersion is given by [58]:

$$\gamma = \omega_* (\omega_* \tau_{\parallel}) \frac{k_y^2 \rho_s^2}{(1 + k_y^2 \rho_s^2)^3} \quad (2.2)$$

Since the factor $k_y^2 \rho_s^2 / (1 + k_y^2 \rho_s^2)^3$ has a maximum for $k_y \rho_s = 1/\sqrt{2}$, the most unstable modes have relatively large wavelengths. For the canonical CSDX case, the fastest growing mode has $\lambda \sim 25 \rho_{Li} \sim 2\pi r_0$, where r_0 is the Gaussian width of the density profile. Thus, in the slab model we expect the $m = 1$ mode to be dominant.

Although the slab model is adequate for describing the wave in certain contexts, it is not directly applicable to CSDX. In addition to the cylindrical geometry, CSDX is likely to exhibit non-local effects because $k_{\theta}^{-1} \sim \rho_s \sim L_n$ for much of the parameter space. For these reasons, in Section 2.4.2 we employ a cylindrical model described by Ellis, et al. [53]. In cylindrical geometry, the dispersion relation is found by solving an eigenvalue equation for the potential fluctuation, $\psi = e\tilde{\phi}/k_B T_e$:

$$\frac{d^2 \psi}{dr^2} + \left(\frac{1}{r} + \frac{1}{n} \frac{dn}{dr} \right) \frac{d\psi}{dr} + \left(Q(r) - \frac{m^2}{r^2} \right) \psi = 0. \quad (2.3)$$

Here, m is the azimuthal mode number, $k \equiv m/r$, and $Q(r)$ is an effective value for k_{\perp}^2 . Solutions are tabulated in Ref. 53 for a Gaussian density profile. The eigenvalues determining Q in the Gaussian model depend only on m and on the ratio of the column width, a , to the Gaussian profile width, r_0 . The ion saturation current profile presented in the following section is nearly Gaussian, so that no new numerical computation is necessary to apply the Ellis model. The resulting dispersion relation is the same as 2.1, but with $k_{\theta}^2 \rho_s^2$ replaced by $b = Q \rho_s^2$:

$$\omega = \frac{\omega_*}{1 + b}. \quad (2.4)$$

Values of b are determined from Fig. 2 of Ref. 53. An annotated version of the figure is shown

Ellis, et al. Plasma Phys. (22) 113 (1980)

For $f \sim e^{-\frac{1}{2}\left(\frac{x-x_0}{\sigma}\right)^2}$
 $\frac{a^2}{r_0^2} \rightarrow \frac{a^2}{2\sigma^2}$

for 12.15,
 best fit has
 $\sigma = 2.9$ cm
 so for $a = [8, 9]$ cm
 $\frac{a^2}{r_0^2} = [3.8, 4.8]$

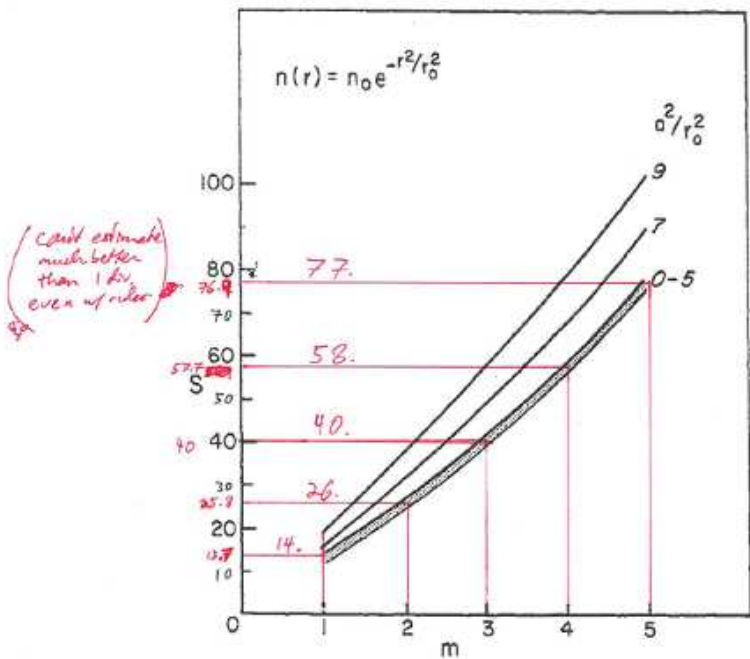


FIG. 2.—Eigenvalue S for the gaussian density profile versus azimuthal mode number with a^2/r_0^2 as parameter. From numeric solution of equation (14).

Figure 2.2: An annotated copy of Fig. 2 of Ref. 53, showing the points used for computation of the b parameter. A parabola fit to these points is used to extrapolate b values beyond $m = 5$.

in Fig. 2.2. A parabola is fit to the designated points, using a Gaussian fit to the I_s profile to determine r_0 (see Fig. 2.3a).

2.2.1.2 Simon-Hoh Instability

The Simon-Hoh instability is a radial $E \times B$ drift instability driven by the difference in neutral drag acting on ions and electrons [54, 55]. Because of its mechanism of action, this instability is variously called the Simon-Hoh instability, the $E \times B$ instability, the crossed-field instability, or the neutral-drag instability [60]. In the edge of CSDX, the neutral density may be comparable to the plasma density and collisions with neutrals cannot be neglected [49]. Because of their low thermal velocity (ions are cold and have large mass), ions collide more frequently with neutrals

and therefore experience a greater drag force. Under the influence of an electric field, the effective $E \times B$ drift of the ions is thus smaller than that of the electrons (ion terminal velocity is lower). The physical mechanism relies on the differential motion of ions and electrons in combination with gradients in density and potential that are oppositely directed. Because the circumstances favoring instability are somewhat esoteric, the Simon-Hoh mechanism is not commonly discussed in the research literature. In particular, it has appeared seldom in fusion-relevant studies because the plasmas in question are taken to be fully ionized¹.

The physical picture of the instability is as follows. In our cylindrical geometry, the zero-order $E \times B$ velocity is in the azimuthal direction ($\hat{\theta}$). The density gradient points inward ($-\hat{r}$), as does the electric field. As a starting point, we take an outward radial excursion of a fluid element from a higher density region into a lower density region. This quasi-neutral density perturbation will separate into an electron perturbation (faster propagation) and an ion perturbation (slower propagation) due to differential neutral drag. The resulting charge separation creates a first-order local azimuthal electric field \tilde{E}_θ , which produces a first-order outward radial $\tilde{E} \times B$ drift in the perturbed region. The induced drift amplifies the original radial excursion, leading to instability. If the electric field points outward (anti-parallel to the density gradient), the induced drift is radially inward and the Simon-Hoh mechanism does not cause instability.

Simon [54] has derived a dispersion relation and calculated the growth rate for the instability in a model situation similar to the conditions of CSDX. Although it is not necessary to reproduce the full equation here, it is important to note that it depends on the details of the neutral collision rates in both perpendicular and parallel directions. The full set of parameters required to calculate a dispersion curve includes parallel and perpendicular neutral collision rates, diffusion rates, and mobilities, for both ions and electrons. Neutral profiles and dynamics are not well studied in CSDX, so quantitative evaluation of Simon-Hoh dispersion relation is not possible at this time. Instead, we simply consider plausibility in Section 2.4.2 based on the discussion presented by Light, Chen,

¹ The “collisionless Simon-Hoh Instability” [61] is a similar process with more relevant application to hot plasmas. Here the mechanism of charge separation is due to a finite-Larmor-radius effect.

and Colestock [52]. If the plasma is significantly magnetized when considering neutral collisions, the Simon-Hoh instability is not likely to be dominant. Thus the plausibility condition for the Simon-Hoh mechanism is $\nu_{en}/\omega_{ce}, \nu_{in}/\omega_{ci} > 1$.

2.2.1.3 Centrifugal Instability

The centrifugal or rotational instability is a gravitational interchange mode, where the effective gravity is provided by rotation of the plasma column. When the mass density gradient is opposite to the the gravitational force, exchange of fluid parcels in a direction parallel to the gradient lowers the potential energy of the system and leads to Rayleigh-Taylor instability [62, 63]. As an illustration, the dispersion relation below describes the stability of a horizontal interface between two fluids of constant density [64]. The gravitational force g is downward. Mass densities of the lower and upper fluids are represented by ρ_1 and ρ_2 , respectively, and the effective surface tension is given as T .

$$\omega^2 = -g|k| \left[\frac{\rho_2 - \rho_1}{\rho_2 + \rho_1} - \frac{k^2 T}{g(\rho_1 + \rho_2)} \right] \quad (2.5)$$

Surface tension is stabilizing and is provided by internal electric fields (quasi-neutrality) [65]. Although the modes we will consider have $k_z \sim 0$, magnetic tension can also contribute when the relevant perturbation has a wavenumber component along the magnetic field [64]. In addition to reducing the growth rate, surface tension plays an important role in the unstable case by selecting the most-unstable wavenumber. Because $\gamma \sim \sqrt{k}$, smaller structures are likely to grow faster when the surface tension is negligible. In practice, however, the local curvature of the perturbation increases as the instability progresses until the surface tension term becomes non-negligible. Nonetheless, we expect that centrifugally-driven fluctuations will be found at higher mode numbers than drift waves. Note that ω is either purely real ($\rho_2 - \rho_1 < k^2 T/g$) or purely imaginary ($\rho_2 - \rho_1 > k^2 T/g$); the modes do not propagate in the fluid frame. Thus, the lab-frame phase velocity of centrifugally driven perturbations is simply the rotation velocity of the column.

In CSDX, the typical density profile peaks at the center of the column, which exhibits significant time-average rotation [49]. Given sufficiently low surface tension, therefore, the system is

unstable to the centrifugal mode.

When there is velocity shear in the system, the centrifugal instability may be suppressed. One measure of whether the rotation or the shear will be the dominant instability mechanism is the centrifugal Richardson number. This dimensionless quantity measures the ratio between the changes in potential energy, due to buoyancy, and changes in kinetic energy, due to mixing when two fluid elements are exchanged. When buoyancy effects are large, rotational instability is likely to occur. If the velocity shear scale length L_v is small compared to the other relevant length scales in the system, shear is likely to be dominant. As defined by Perkins and Jassby for a cylindrical column [50], the Richardson number is:

$$|Ri| = \frac{L_v^2}{r} \left| \frac{1}{n} \frac{dn}{dr} \right| = \frac{L_v^2}{rL_n}. \quad (2.6)$$

We will use the Richardson number to make a plausibility argument against centrifugal instability in section 2.4.2.

2.2.1.4 Transverse Kelvin-Helmholtz Instability

The Kelvin-Helmholtz (KH) instability is a well-known mixing instability driven by sheared fluid flow. Small scale perturbations are accelerated by the mean flow, extracting energy into a vortex-chain-like wave. More precisely, the vorticity fluctuations driven by shearing of the perturbed surface are phased relative to the cross-streamwise displacement of the surface, such that the initial distortions of the interface are reinforced [66, 67]. The dispersion relation for perturbations to a plane interface between fluids with velocities u_1 and u_2 gives a complex value for ω [64]:

$$\omega = -k_x \frac{\rho_1 u_1 + \rho_2 u_2}{\rho_1 + \rho_2} \pm \sqrt{-g|k| \left[\frac{\rho_2 - \rho_1}{\rho_2 + \rho_1} - \frac{k^2 T}{g(\rho_1 + \rho_2)} \right] - k_x^2 \frac{\rho_1 \rho_2}{(\rho_1 + \rho_2)^2} (u_1 - u_2)^2}. \quad (2.7)$$

As above, the gravitational force, g , is downward, mass densities of the lower and upper fluids are represented by ρ_1 and ρ_2 , respectively, and the effective surface tension is given as T . The terms involving the velocity shear depend only on the component of the wavevector parallel to the flow interface (denoted by k_x). We shall consider only pure KH modes, where $k = k_x$. In contrast to the

centrifugal instability, the Kelvin-Helmholtz instability can generate propagating waves, as viewed in the frame of either fluid. The real part of the phase velocity is, in fact, the mass-density-weighted average velocity in the vicinity of the shear layer.

As with the centrifugal instability, surface tension is stabilizing. Note that stratification can be stabilizing or destabilizing². Even more so than for the centrifugal instability, the fastest growing KH modes are small-scale (neglecting surface tension, $\gamma \sim k_x$). Again, the practical implication is that higher mode numbers are likely to be excited than in the case of the drift instability.

2.3 CSDX-U Device

2.3.1 Overview

The Controlled Shear Decorrelation eXperiment - Upgrade (CSDX-U) is a linear machine, which generates a cold ($T_e \sim 3 \text{ eV}$, $T_i \sim 0.5 \text{ eV}$), dense ($n_e \sim 10^{18} \text{ m}^{-3}$), magnetized ($\rho_{\text{Li}}/r_{\text{plasma}} \sim 0.03\text{--}0.3$) plasma column in argon using a recently-upgraded helicon source. Early work established the presence of a sheared azimuthal velocity profile in the absence of external momentum input [68] and documented the structure of fluctuations using measurements of ion saturation current, floating potential, and visible-light emission [33, 57, 69]. Drift waves were identified as the dominant class of fluctuations in the plasma [57]. Efforts to date on CSDX have found evidence for turbulent stresses [70, 49], nonlinear energy transfer [71, 72], and localized structures [33, 41].

The machine has recently been upgraded and now uses a 15-cm-diameter, 13.56 MHz radio-frequency (RF) source, operated at up to 5 kW in the $m = 0$ helicon mode. The vacuum system is the same as for previous studies, with a 20-cm-diameter cylindrical chamber. The canonical parameters for the experiments described here are chosen to be similar to previous work on CSDX. The working gas is argon, at a pressure of $3.2 \times 10^{-3} \text{ Torr}$ and a flow rate of 25 sccm. The RF power is 1600 W with less than 1% reflected, and the background magnetic field is 900 G for the baseline case. Time-average profiles for these parameters are shown in Figure 2.3. The raw I_s data

² In fact, the Rayleigh-Taylor or centrifugal instability can provide initial perturbations, which are then sheared and rolled up by the velocity differential across the perturbed structure.

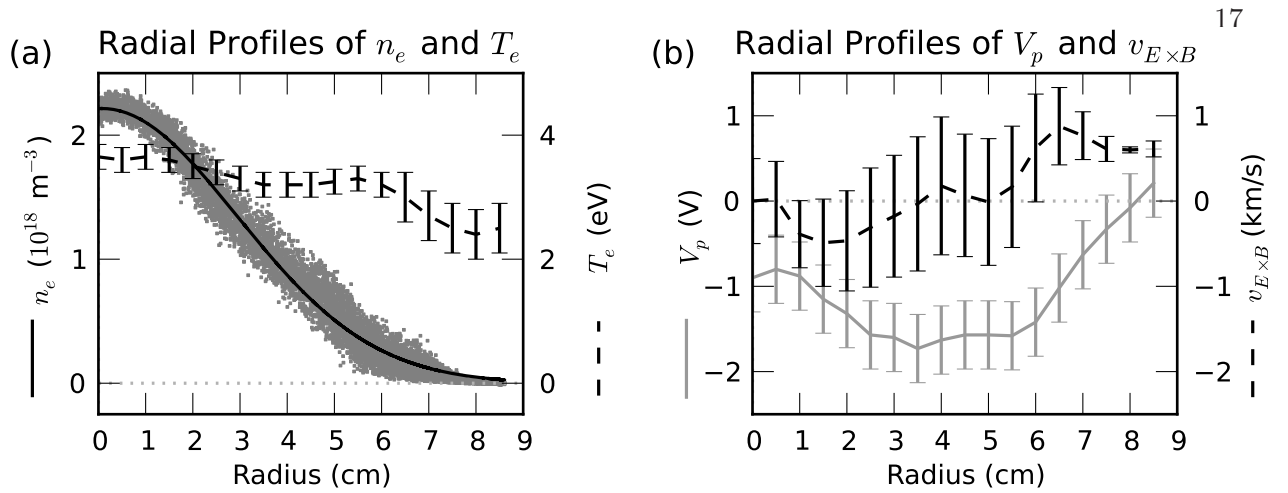


Figure 2.3: Time average profiles for plasma parameters. (a) Electron density and temperature profiles. The black solid line is a Gaussian fit to the density data (gray dots). (b) Measured plasma potential and resulting azimuthal $E \times B$ velocity.

has a nearly Gaussian profile, as does the corresponding density data. A fit is shown in 2.3(a) for comparison. The $E \times B$ velocity derived from plasma potential profiles is shown in 2.3(b). Evidence for sheared flow has been documented in the previous CSDX source [69, 68], but the presence of a time-varying flow component [39] means that this average profile provides incomplete information. In addition, the uncertainties in the derived velocity profile are large, so that $v_{E \times B}$ is not particularly well constrained by swept probe measurements.

2.3.2 Device Hardware

2.3.2.1 Vacuum System

A diagram of the CSDX device, including dimensions and locations for diagnostics, is shown in Figure 2.4. The experiment volume consists of a cylindrical stainless-steel chamber with length 2.8 m and internal diameter (ID) 20 cm. The plasma source bell jar is mounted concentrically on one end, and a glass window is mounted on the other. The axial location $z = 0$ m is defined by the mating surface of the bell jar flange with the cylinder flange, with \hat{z} pointing away from the source. The vacuum system consists of roughing pump and a 1000 L/s turbomolecular pump, separated from the main chamber by a butterfly valve. The valve and pump are mounted on an

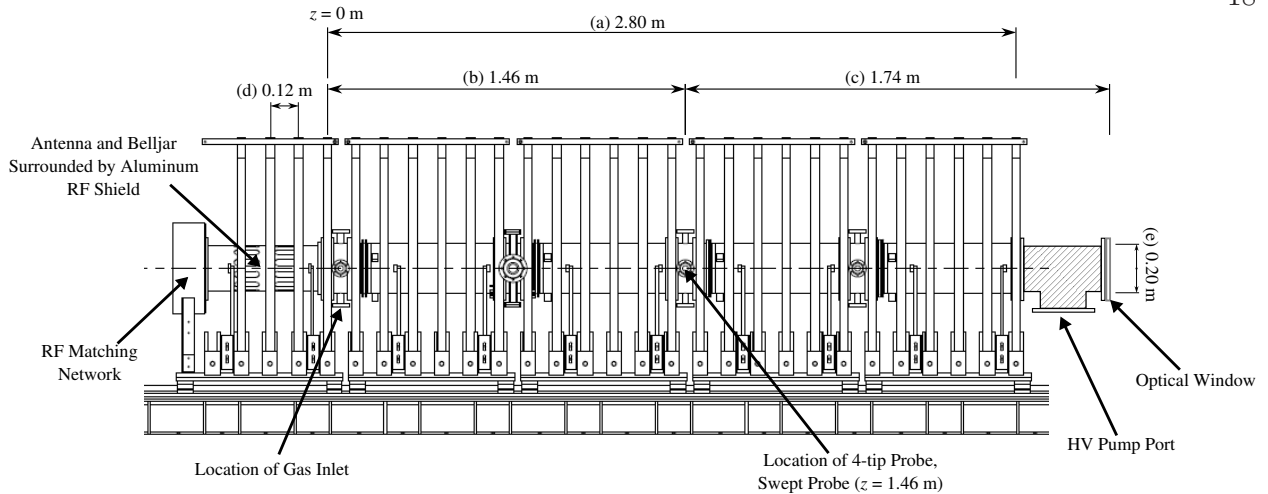


Figure 2.4: Technical drawing of the CSDX device. Labeled distances are as follows: (a) Length of experimental section. (b) Axial distance from $z = 0$ to location of 4-tip probe. (c) Axial distance from location of 4-tip probe to end window (optical path length from the camera focal plane to the window). (d) Magnet spacing. (e) Diameter of experimental section.

extension tube, which is electrically insulated from the plasma by a teflon liner (hatched in Figure 2.4). The minimum base pressure is $\sim 10^{-6}$ Torr, and the pressure and flow rate of the working gas is controlled by adjusting both the gas input rate and the butterfly valve (pumping rate). Gas input is determined by a mass flow controller in units of 1 sccm (standard cubic centimeters per minute). Typical flow rates are between 15 and 35 sccm at a pressure of several milliTorr.

2.3.2.2 Plasma Source

CSDX plasmas are produced by a 13.56 MHz RF source, coupled into the helicon mode via an antenna with either $m = 0$ or $m = 1$ mode structure. The antenna wraps around a glass bell jar attached to one end of the vacuum chamber, and is coupled to the RF power supply via an automated matching network. Reflected power is generally $< 1\%$. The room is shielded from the antenna via a slotted aluminum cylinder placed between the matching network and the vacuum chamber (see Figure 2.4). Given the bright blue core, high density, and low temperature of the plasma typical for these sources, we assume plasma production via a true helicon wave. Wave field measurements verifying helicon operation have been made in a similar source with diverging

magnetic field geometry [73], but have not been repeated in the current device geometry. The diameter of the bell jar has recently been increased from 10 cm to 15 cm, and the RF power supply has been upgraded from 2 kW to 5 kW. The source is run in steady state, with water cooling for the antenna and forced air cooling for the bell jar. The cooling is not sufficient to maintain ambient temperature with the upgraded source, so care must be taken to ensure that wall conditions do not change appreciably over the course of an experiment. For example, at $P_{RF} = 1800$ W, the operating temperature of the chamber stabilizes near 75° C, but at $P_{RF} = 4500$ W, the chamber temperature rapidly increases to above 110° C.

2.3.2.3 Magnet System

The vacuum chamber is located in the bore of a set of 29 pancake magnet coils, spaced every 12 cm (see Figure 2.4). Current is supplied to the coils by computer-controlled high-current power supplies, adjustable in increments of 10 A. The coils are water cooled and can be run at currents up to 800 A in steady-state. Provided that the source can couple into the plasma, the range of accessible background field values is 400 to 2400 G. The field is quite uniform over the cross section of the vacuum chamber, so that field values at the center and at the edge differ by $\sim 1\%$. The axial profile of the field is also quite uniform in the middle 50% of the experimental section, where data is acquired. Figure 2.5(a) shows the axial variation in field strength along the entire coil set. For reference, the current-to-field calibration plot is shown in Figure 2.5(b).

2.3.2.4 Probe Diagnostics

In addition to the fast imaging system described below, several probe diagnostics are employed for profile and fluctuation measurements. Time-average properties are measured with a single-tip swept Langmuir probe, compensated for RF rejection [74].

Fluctuations are measured as a function of both time and space by an electrostatic probe array. The array has four tips, each digitized at approximately 500 kSamples/s. One tip of the probe is biased to collect ion-saturation current (I_s). The other three tips are arranged as in Figure

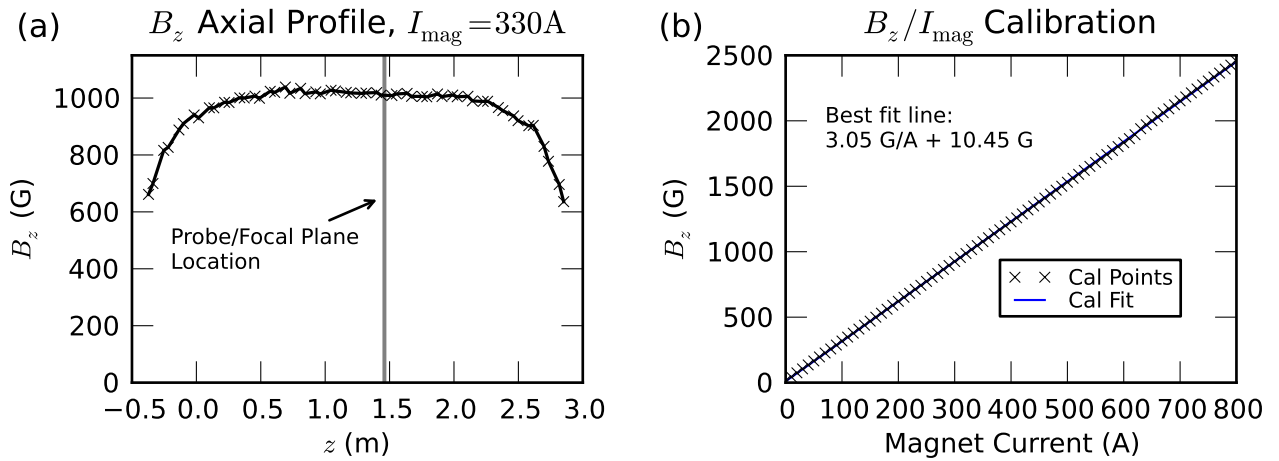


Figure 2.5: Background axial magnetic field properties. (a) Axial profile of background magnetic field at $I_{\text{mag}} = 330 \text{ A}$. (b) Calibration data for background magnetic field as a function of coil current. Uncertainties in measured values are within the size of the data markers for both (a) and (b).

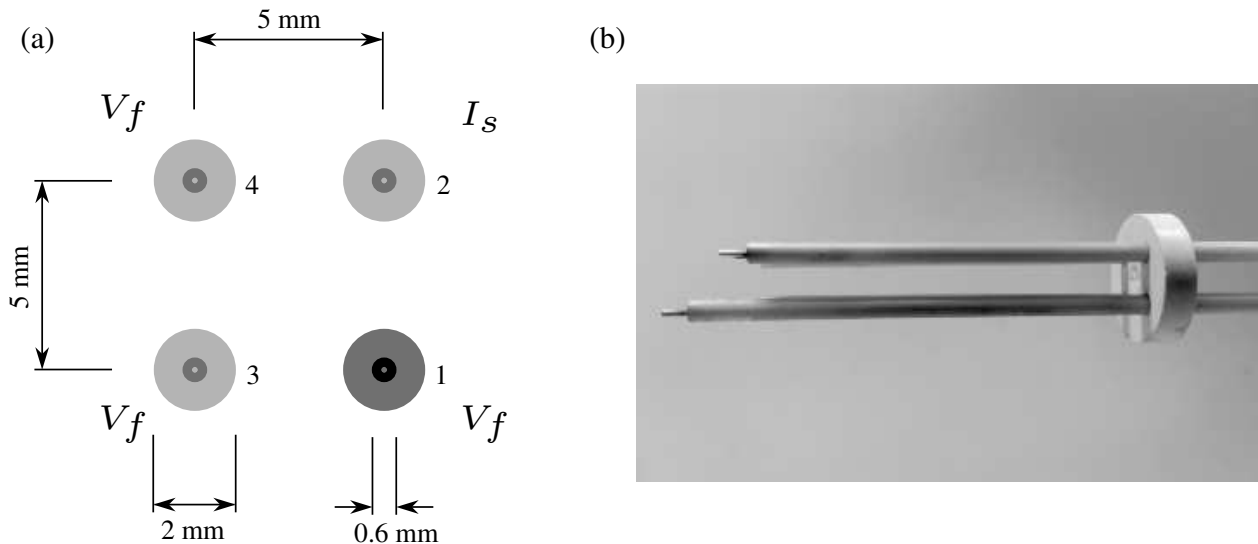


Figure 2.6: (a) Layout of the electrostatic probe used for measuring fluctuations. The view is end on, from the center of the plasma column. Tips 2, 3, and 4 are in the same (radial) plane while tip 1 protrudes farther into the plasma (darker shading). This geometry allows radial and azimuthal electric fields to be estimated from differences in floating potential. (b) Photograph of the actual probe (side view), including stabilizer disk to ensure that the geometry remains fixed even if the probe stalk droops.

2.6 to measure the floating potential (V_f) at three points in the plasma, two separated azimuthally by 5 mm and two separated radially by 5 mm. The radius of each cylindrical tip is $r_t = 0.6 \text{ mm}$. In

comparison, the plasma column radius is $r_p \sim 8$ cm, and the ion cyclotron radius and Debye length for the canonical parameters listed above are $\rho_{Li} \sim 7$ mm and $\lambda_D \sim 10$ μ m. Because $\rho_{Li} \gg r_t$, an unmagnetized probe theory is used to interpret the data [75].

The entire probe stalk is mounted on a translating stage. Motion is roughly aligned with the radial coordinate of the experiment, allowing a radial profile to be extracted from a single acquisition. Translation has been accomplished by means of a pneumatic actuator (maximum translation speed ~ 10 cm/s).

In addition to recovering mean and fluctuation profiles of I_s and V_f , the geometry of the probe allows finite difference gradients in floating potential to be calculated in the azimuthal and radial directions. If temperature fluctuations are negligible, floating potential fluctuations should be equivalent to plasma potential fluctuations [75]. For reference, we summarize here the relationship between floating and plasma (V_p) potentials given by Stangeby [76]. The difference between V_f and V_p is proportional to the electron temperature, T_e , multiplied by a logarithmic factor:

$$V_p - V_f = \frac{k_B T_e}{e} \ln \left[\left(2\pi \frac{m_e}{m_i} \right) \left(1 + \frac{T_i}{T_e} \right) \frac{1}{(1 - \gamma)^2} \right] \quad (2.8)$$

where e is the elementary charge, k_B is the Boltzmann constant, m_e and m_i are the electron and ion masses, T_i is the ion temperature, and γ is the secondary electron emission coefficient of the probe surface. For the case of CSDX, $T_i \ll T_e$, so that we may treat the logarithm as a constant even in the presence of moderate temperature fluctuations. For argon at canonical conditions, we have approximately

$$V_p - V_f \simeq 5.18 T_e \quad (2.9)$$

where T_e is measured in units of electron volts (eV). In many low temperature plasma experiments, including previous work on CSDX[57], the assumption of small temperature fluctuations ($\tilde{T}_e/T_e \ll 1$) is made so that plasma potential and floating potential fluctuations become approximately equal:

$$\frac{\tilde{V}_p - \tilde{V}_f}{\langle T_e \rangle} \simeq 5.18 \frac{\tilde{T}_e}{\langle T_e \rangle}. \quad (2.10)$$

The usual arguments for the validity of this assumption in CSDX are twofold: 1) Fluctuation

levels are approximately proportional to the gradient strength, and T_e profile is rather flat (Figure 2.3a); 2) The different functional relationships of I_s and V_f to T_e should manifest in the relative fluctuation levels as \tilde{T}_e/T_e changes, yet $\tilde{I}_s/\langle I_s \rangle \approx \tilde{V}_f/\langle V_f \rangle$ across parameter combinations [57]. Nevertheless, comparisons of experimental CSDX data with simulation may hint at the importance of temperature fluctuations [77]. Further questions about the magnitude and effects of temperature fluctuations are addressed in Section 2.5.

Under the above assumption, $\tilde{\mathbf{E}}_{\perp} \approx -\nabla_{\perp} \tilde{V}_f$ can be measured by the four-tip probe. Since magnetic field fluctuations are negligible in regimes explored to date [78], we may then calculate fluctuating $E \times B$ velocities from electrostatic measurements.

2.3.2.5 Imaging System

Image sequences of up to several hundred thousand frames are acquired using a Phantom v7.10 CMOS camera. Visible light from the plasma is collected through an end window by a 1200 mm, $f/8$ telescope (Celestron C6-RGT) at a distance of ~ 7 m from the focal plane using a 180 mm, $f/4$ lens as an objective. The image is projected onto the camera sensor using a standard 25 mm, $f/1.4$ C-mount lens. The long focal distance allows the sight-lines of the camera to be aligned with the background magnetic field to within $\pm 0.6^\circ$, minimizing parallax. Additionally, parallel dynamics are not expected to contribute to imaging measurements because the depth of field (DOF) around the image plane is much less than the machine length, L ($\text{DOF} \ll L \sim 1/k_{\parallel}$). Using our optical arrangement, each pixel images a volume of width $\Delta x = \Delta y = 1.5$ mm in the focal plane ($r_{\text{plasma}}/\Delta x \sim 50$) and depth $\Delta z \sim 10$ cm ($L/\Delta z \sim 30$).

In this study, we present analysis of a single sequence of 10,000 frames of 488-nm (ArII) light, referred to as I_{488} (shot label 12215f488). The narrowband optical filter (± 10 nm FWHM) we use reduces the collected intensity significantly, so that the minimum exposure time is on the order of $20 \mu\text{s}$. Images are acquired with 128x128-pixel resolution at a rate of 50,000 frames/second (50 kfps). We record images with wider spatial coverage than the extent of the visible plasma column (~ 110 pixels in diameter) to ensure accurate pixel-to-cm calibration and to reduce edge effects when

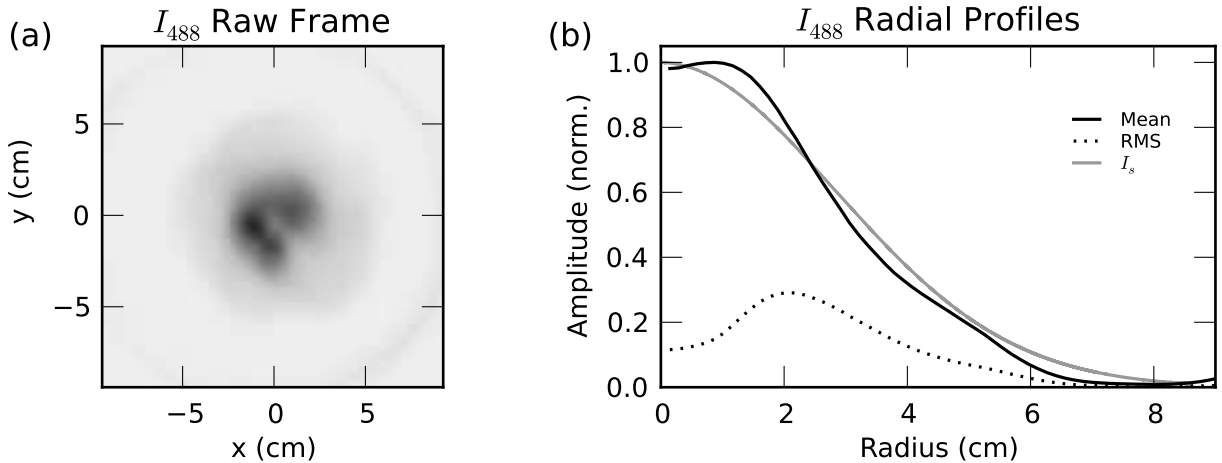


Figure 2.7: (a) Raw image example (single frame). White corresponds to zero intensity. (b) Normalized radial profiles of mean I_{488} (solid black), RMS I_{488} fluctuation amplitude (dashed black), and mean I_s (solid gray).

calculating velocity fields. The raw unit of I_{488} is an unsigned integer (uint) corresponding to the intensity level within the 12-bit (0 – 4095) range of the images. Data presented here is normalized to the maximum intensity value in the image sequence, so that I_{488} lies in the range $[0, 1]$.

A sample raw image frame for shot 12215f488 is shown in Fig. 2.7(a). Black corresponds to approximately 60% of the maximum I_{488} value in the sequence and white to zero intensity. The spatial scale shown here applies to all images presented in this study. The mean I_{488} profile and the profile of the root-mean-square (RMS) I_{488} fluctuation level about the mean, both normalized to the maximum mean brightness, are plotted versus radius in (b). Averages to obtain mean profiles are performed over both time and azimuth. Also shown in Fig. 2.7b is the I_s profile from Fig. 2.3a, normalized. The width of the mean brightness profile closely matches the width of the I_s profile, indicating that the entire ionized column is visible in the 488-nm wavelength band. For reference, a more detailed comparison of the normalized electron density, ion saturation current, and intensity profiles is shown in Figure 2.8. Note that I_s is a good proxy for n_e . Further study of the relationship between probe and imaging measurements is presented in Section 2.5.

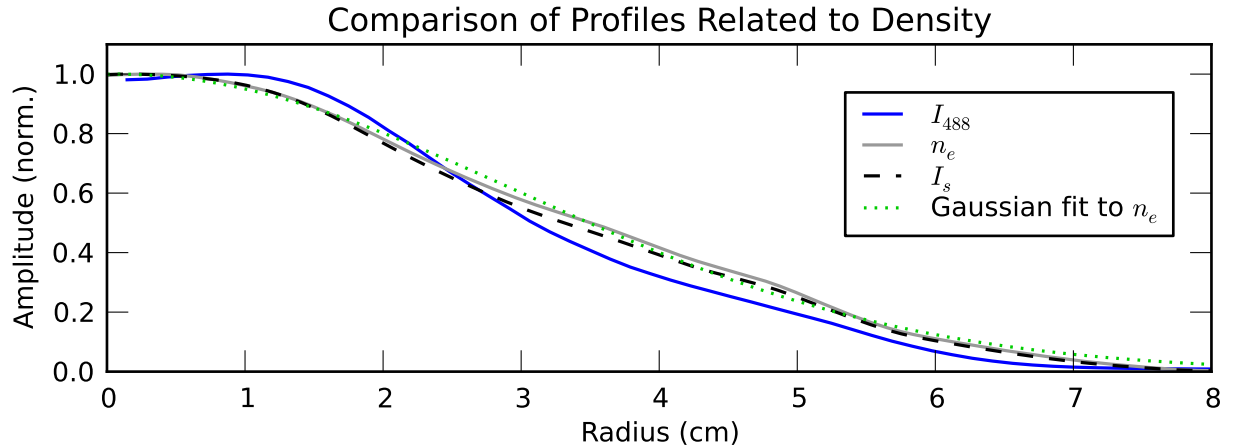


Figure 2.8: Time-average radial profiles of electron density (n_e), ion saturation current (I_s), and intensity (I_{488}). A Gaussian fit to the density is a convenient and reasonably accurate representation of the profile shape.

2.4 Imaging Measurements of Coherent Modes

2.4.1 Cross-spectral-density Phase Mapping

In order to extract information about the spatial structure and coherence of recorded fluctuations, we use a cross-spectral-density (CSD) technique to map spatial variations in phase onto the pixel grid. This map provides a two-dimensional picture of the coherent spatial features present at each frequency. Unlike spatial Fourier filtering, the phase map preserves azimuthal asymmetries. The estimated discrete CSD is defined in the standard way [3], as described in Section 1.2.2 (a description is provided here as well, to facilitate a self-contained discussion). Each pixel is considered to be a discrete-time signal, sampled at points t_j , $j = 0, 1, \dots, N$. To calculate the relative phase between two pixels, the signals $x(t_j)$ and $y(t_j)$ are divided into n_d distinct (non-overlapping) blocks of length T_d with appropriate windowing, and each block is transformed into the frequency domain. The resulting Fourier signals $X_i(f_j)$ and $Y_i(f_j)$ are multiplied together to construct a raw estimate of the CSD for each block i at each frequency f_j . These block estimates are averaged together to calculate the smooth estimate (cf. Equation 1.2)

$$\hat{G}_{xy}(f_j) = \frac{2}{n_d T_d} \sum_{i=1}^{n_d} X_i^*(f_j) Y_i(f_j). \quad (2.11)$$

We use $n_d = 50$ blocks of $N_d = N/n_d = 200$ time points each to calculate $\hat{G}_{xy}(f_j)$, corresponding to a frequency resolution of 250 Hz. Because CSDX is a steady-state system, and its time-average properties are stable and well-converged [49], we rely on the assumption of time-stationarity over the length of the image sequence to reduce the uncertainty in our estimates³. In a statistically-stationary system, averaging over calculations for the n_d separate time blocks amounts to ensemble averaging.

The phase angle of the complex $\hat{G}_{xy}(f_j)$ gives an estimate of the time-average phase difference between $x(t_j)$ and $y(t_j)$ at each frequency, f_j , and the coherence function

$$\gamma_{xy}^2(f_j) = \frac{|\hat{G}_{xy}(f_j)|^2}{\hat{G}_{xx}(f_j)\hat{G}_{yy}(f_j)} \quad (2.12)$$

gives an estimate of the stability of this cross-phase in time and space. For the analysis presented here, $x(t_j)$ is the I_{488} time series for a fixed reference pixel, and \hat{G}_{xy} represents the spectral properties of pixel y relative to x . Explicit notation of the discrete frequency and time indices is suppressed in further CSD expressions, and all quantities are assumed to be functions of frequency unless otherwise noted.

Fig. 2.9 compares the coherence spectrum and CSD power spectrum, spatially-averaged over pixels inside a 5-cm radius, showing that the spectrum is dominated by coherent modes for the fixed plasma parameters of this study. Error bars in the cross-spectral power are given by the statistical uncertainty in the discrete CSD estimate [3], $\delta|\hat{G}_{xy}|/|\hat{G}_{xy}| = 1/|\gamma_{xy}|\sqrt{n_d}$. At the frequencies where there is a peak in the average coherence, we may expect to find coherent spatial structures. An uncertainty for each pixel in the phase map can be estimated as a function of frequency by the standard deviation of the cross-spectral phase[3] (cf. Equation 1.6):

$$\sigma = \frac{(1 - \gamma_{xy}^2)^{1/2}}{|\gamma_{xy}|\sqrt{2n_d}} \quad (2.13)$$

Example phase maps are shown in Fig. 2.10, demonstrating mode structures for each of the four frequency bands shaded in Fig. 2.9. The reference pixel for these calculations is located at $r = 3.5$ cm and $\theta = \pi$. Fig. 2.11 shows maps of this uncertainty (Eq. 1.6) corresponding to each

³ The necessity for time stationarity can be relaxed by using a smaller number of time blocks to obtain smooth estimates, trading increased spectral variance for faster time-resolution.

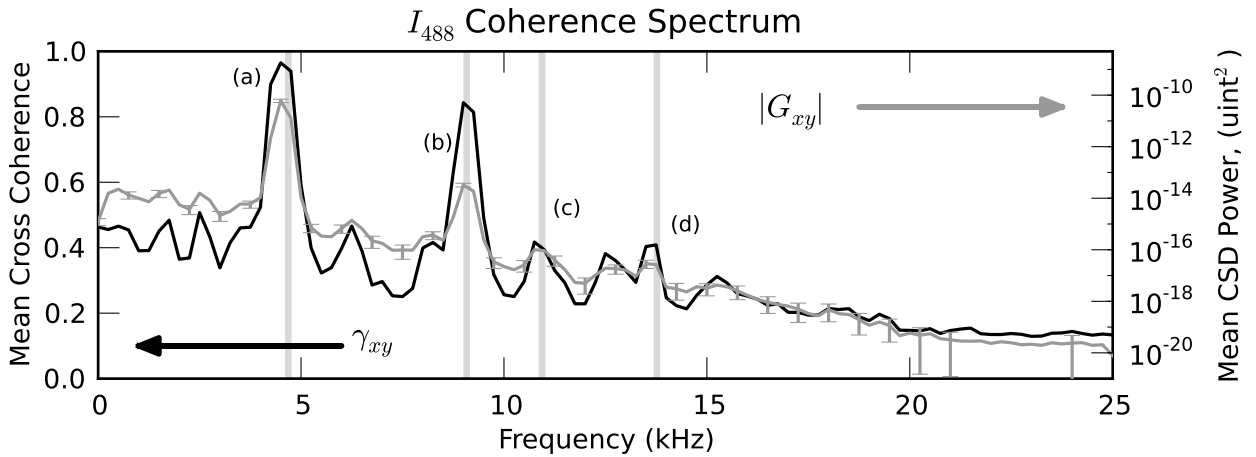


Figure 2.9: The average coherence spectrum of the plasma column compared with the average power spectrum. Error bars in the cross-spectral power are statistical uncertainty in the discrete CSD estimate. Note that the power spectrum is plotted on a logarithmic scale. (a)-(d) are the four most prominent peaks, corresponding to the phase maps in Fig. 2.10.

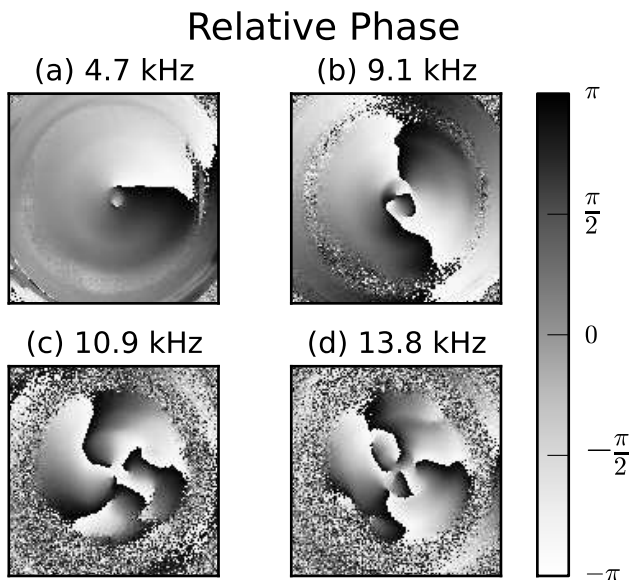


Figure 2.10: Sample phase maps for the four most prominent coherent modes. Vertical bars in Fig. 2.9 highlight the frequency component corresponding to each map, (a), (b), (c) and (d).

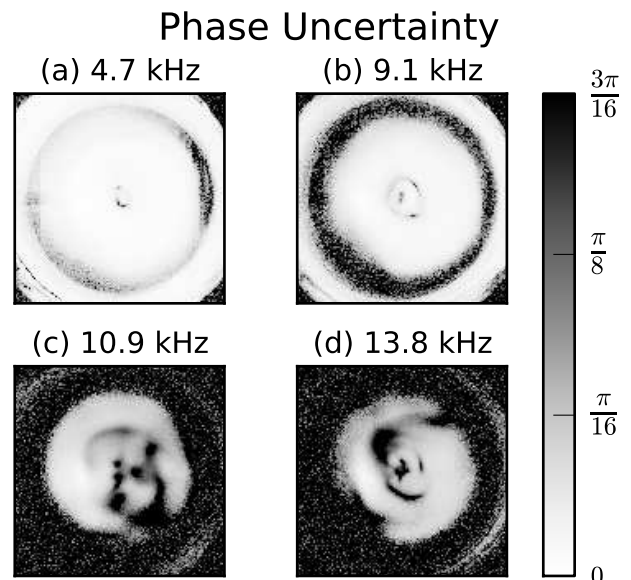


Figure 2.11: Standard-deviation maps (Eq. 1.6) corresponding to Fig. 2.10. Note that particularly asymmetric parts of the phase maps seem to coincide with high uncertainty.

of the phase maps in Fig. 2.10. The uncertainty inside the visible column for coherent modes is generally $\ll \pi/16$ radians, though significant variation is present. The dark bands visible in (a) and (b) are located in the space between the visible plasma column and the vacuum wall. Bright

regions outside this band are due to reflections from the interior of the chamber. Similar features are visible in Fig. 2.10. The lower average coherence value of frequency bands (c) and (d) in Fig. 2.9 reflects the non-uniform coherence at these frequencies (visible as phase uncertainty). Regardless of the patches of high variance in the relative phase for (c) and (d), there are large regions where the uncertainty in the phase is well under 5% of 2π ($\pi/16 \approx 3\%$). It is clear that multiple coherent modes exist in the plasma, and the mean azimuthal and radial structure of each is well resolved by cross-spectral-density phase mapping.

Although most of the coherent modes do exhibit a high degree of azimuthal symmetry, it is important to note that the phase-mapping technique does not impose any symmetry constraints. In particular, Fig. 2.10(c) shows a map with a distinctly asymmetric phase structure. The corresponding uncertainty map shows that deviations from the expected symmetry seem to be concentrated in regions of low coherence (relative to the reference pixel). Because the coherence is generally high outside these regions, large phase uncertainty is taken to be a result of local variation in the mode structure (either temporal or spatial).

Physical perturbations, such as the presence of a probe, could disrupt fluctuations in a localized region of space and lead to asymmetries and temporal incoherence in the mode pattern. In CSDX, various probes are present in the vacuum vessel, though during image acquisition they are retracted beyond the radius where the plasma density becomes negligible. In addition to physical perturbations, asymmetries in the source or dynamic equilibrium could be reflected in the mode patterns. Fig. 2.12 shows average (a) and RMS (b) I_{488} frames, along with their azimuthal profiles at $r = 3$ cm (c). Clear asymmetries are present in these phase-insensitive quantities. Because no probe or other obstruction was inserted into the visible region during data collection, it is likely that there is azimuthal variation intrinsic to the time-average plasma column. The presence of these asymmetries means that care is needed when examining the average spatial properties of fluctuations. Note that the profile of the average radial gradient of I_{488} does not line up with the RMS profile. This behavior is an indication that using I_{488} as a proxy for I_s is questionable, since the I_s fluctuation amplitude peaks where the I_s gradient is steepest.

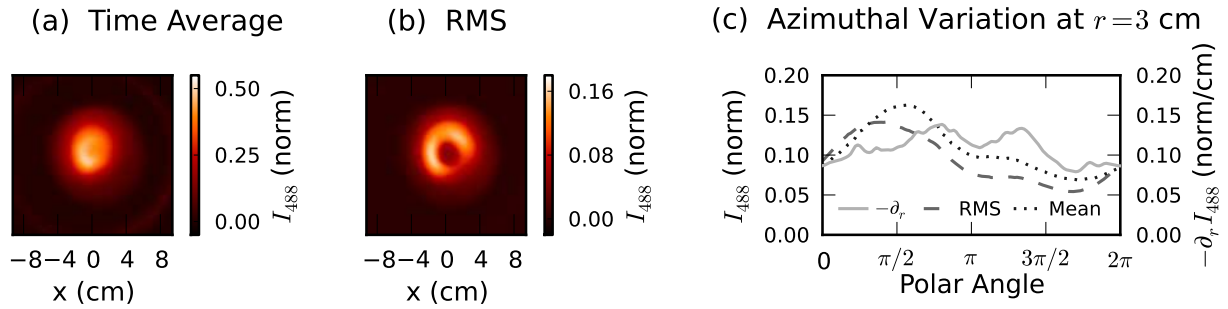


Figure 2.12: (a) Time-average frame. (b) RMS frame. (c) Azimuthal variation at $r = 3$ cm for time-average (mean) I_{488} , RMS I_{488} , and the radial gradient (negative) of I_{488} . Intensity is normalized to its maximum value in the image sequence.

2.4.2 Dispersion estimates from intensity

The relationship between the spatial and temporal properties of a wave, its dispersion relation $\omega(k)$, provides a unique signature for identifying the wave. The presence of multiple, discrete peaks in the coherence spectrum makes plausible the extraction of dispersion properties for these modes. Previous studies over more than 25 years [4, 5, 6, 7, 8, 9, 10, 11, 12, 13, 14, 15] have used probe pairs to estimate the wavenumber spectrum and statistical dispersion relation [16] for plasma fluctuations. The two-point technique estimates the power spectral density, $s(k, \omega)$, using a conditional wavenumber spectral density, $s_l(K|\omega) = S_l(K, \omega)/S(\omega)$, where K is the local wavenumber. This approximation holds under the condition that the fluctuations being measured can be represented by a superposition of wave packets [16]. A statistical dispersion relation is then calculated as the weighted average of K given $s_l(K|\omega)$ (first spectral moment). Although two-point measurements of wavenumber spectra have proven successful at identifying the dominant wavenumber at a given frequency, it may be impossible to extract reliable information beyond the mean and width of the wavenumber spectrum at each frequency [17].

In the case of imaging, where we have access to multi-dimensional signals, these restrictions no longer apply. We obtain an experimental estimate for the dispersion relations of waves present in the visible light measurements using a two-dimensional auto-spectral density technique (Section 1.2.4). The image array is mapped into polar coordinates, and the auto-spectral density is calculated

for n_d blocks of N_d time points, as above. Note that the result is insensitive to the uncertainty in the center position used for the mapping ($\delta r \sim 1$ pixel). The raw estimate for each block i is:

$$G_{xx}^{(i)}(r, \theta, f_j) = C_j X_i^*(r, \theta, f_j) X_i(r, \theta, f_j), \quad (2.14)$$

where $C_j = 2/T_d$ for $j = 1 \dots N_d/2 - 1$ and $C_j = 1/T_d$ for $j = 0, N_d/2$. The dependence on position (r, θ) is indicated explicitly for clarity. A fast Fourier transform is then performed along the azimuthal index. Windowing is not required, as the data is truly periodic along the transform axis. A basis of pure azimuthal modes is non-ideal, due to the presence of azimuthal asymmetries noted above (Fig. 2.12), and results in broad mode spectra where there is significant frequency content. We choose to use the azimuthal Fourier basis in spite of this limitation in order to estimate the global spectral density for the plasma (averaged in both time and azimuth). The n_d calculations of $G_{xx}^{(i)}$ are averaged to obtain a smooth estimate of the two-dimensional auto-spectral density, now a function of radius (r), mode number (m), and frequency (f):

$$\hat{G}_{xx}(r, m, f_j) = \frac{C_j}{n_d} \sum_{i=1}^{n_d} X_i^*(r, m, f_j) X_i(r, m, f_j). \quad (2.15)$$

We again use $n_d = 50$ blocks of $N_d = 200$ time points, corresponding to a fractional uncertainty in measured power of $1/\sqrt{n_d} = 14\%$ and a frequency resolution of 250 Hz. For consistency with theory conventions, we transform from units of mode-number (m) and frequency (f) to those of wavenumber ($k_\theta = m/r$) and angular frequency ($\omega = 2\pi f$).

To identify the waves contributing to the measured spectral power, we plot theoretical dispersion relations over the experimental estimates. Theory calculations use temperature and density values from the Langmuir probe measurements shown in Fig. 2.3. If there are multiple unstable modes driven by the same mechanism, they should lie along a single theoretical dispersion curve. The mode most often observed in previous CSDX experiments is the electron drift wave [57], where the natural length scale is the ion sound gyroradius, $\rho_s = \sqrt{kT_e/m_i\omega_{ci}^2} \sim 1$ cm. Because $k_\theta^{-1} \sim \rho_s \sim r$ for much of the parameter space, we may expect that cylindrical effects are important. Therefore, we adopt the cylindrical model of Ellis et al. for calculating theoretical drift wave

dispersion curves [53]. The nearly Gaussian density profile (see Fig. 2.3) allows us to compare to this model directly, without additional numerical computations. The leading order approximation to the drift frequency is

$$\omega = \frac{\omega_*}{1+b}, \quad \text{where } \omega_* = k_\theta v_{de} = k_\theta \frac{T_e}{eB} \frac{1}{n} \frac{\partial n}{\partial r} \quad (2.16)$$

and b is an effective cylindrical value for $k_\theta^2 \rho_s^2$ including cylindrical and non-local effects. To this order, the cylindrical dispersion relation is of the same form as the slab dispersion relation, including finite-Larmor-radius effects. For $b \ll 1$ (low-order modes at large radius), the phase velocity of these waves is simply the electron diamagnetic velocity, v_{de} . The b parameter is calculated here by fitting a parabola to the appropriate trace in Fig. 2 of Ref. 53. Dispersion curves are plotted as dotted lines for $m > 5$ to reflect the fact that b is tabulated only for $m = 1 - 5$.

Fig. 2.13(a) shows $\hat{G}(r=3 \text{ cm}, k_\theta, \omega)$, normalized to the total spectral density at $r = 3 \text{ cm}$. To enable comparison with theory curves, white circles are overlaid to indicate maxima in the k -spectra for frequencies with summed spectral power above the background level. The summed spectral power is defined as $\bar{G}(\omega) = \sum_k \hat{G}(k, \omega)$. In quantitative terms, a circle is plotted for each frequency where $\log_{10} \bar{G}(\omega)$ is larger than its linear trend (a linear background as in the power spectrum of Fig. 2.9 is universal in the data presented here). These points constitute the experimentally measured dispersion relation, $\hat{\omega}(k)$. For comparison, calculations of the power spectral density using two-point measurements from both probe and imaging data are shown in Fig. 2.13(c) and (d). Fig. 2.13(c) shows the estimate obtained from two floating potential tips separated by 6 mm in the vertical direction ($\Delta\theta \sim 6 \text{ mm}$), while 2.13(d) shows the estimate from two pixels at the approximate position of the probe tips (retracted during imaging). Fig. 2.13(b) shows an azimuthal average over 32 separate two-point estimates from pixel data at $r = 3 \text{ cm}$, which produces a result similar to the auto-spectral density calculation (a). The two-point estimates are generally noisier than the 2D auto-spectral-density estimate, and vary less smoothly in (k, ω) space.

Since the measurements are taken in the laboratory frame, measured phase velocities may be shifted by local $E \times B$ flow. Several traces are plotted on Fig. 2.13(a) to demonstrate the

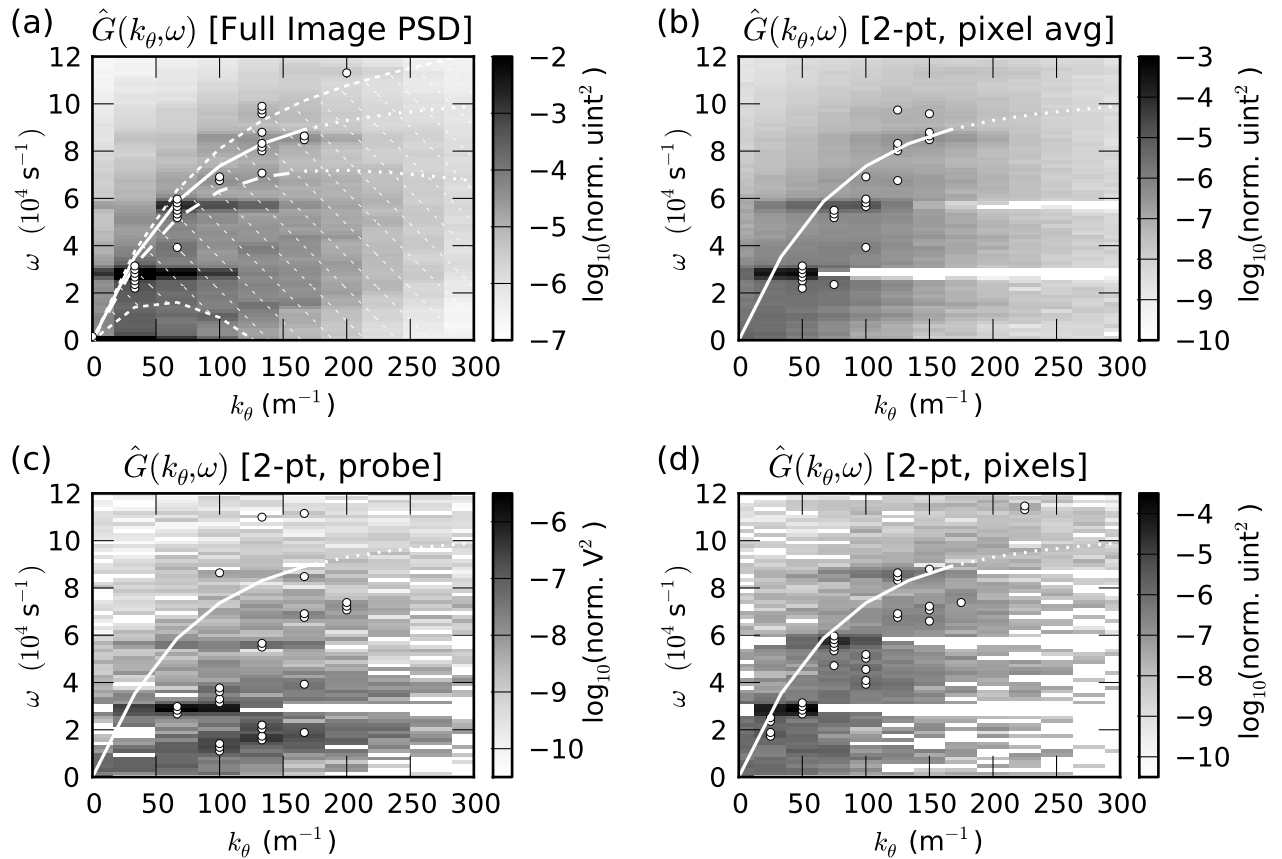


Figure 2.13: Normalized spectral density and measured dispersion relations at $r = 3$ cm from (a) 2D auto-spectral density of image data, (b) average of 32 two-point estimates from pixel data, (c) two-point floating-potential data (probe), and (d) two-point pixel data. The color scale for each plot indicates the power relative to the total spectral power at the given radius. White circles represent the maxima of the k -spectra for frequencies where the total spectral power is more than 1% above background. The dashed line in (a) represents the raw theoretical expectation [Eq. (2.16)] calculated from the profiles in Fig. (2.3). The hashed region in (a) indicates likely bounds for Doppler-shifted theory curves based on the $E \times B$ profile of Fig. 2.3(b). The solid line in each plot is the theoretical expectation including the best-fit Doppler shift for (a).

sensitivity of the drift dispersion curve to these Doppler shifts. The dashed white line indicates the raw estimate, corresponding to $v_{E \times B} = 0$. The hashed region between dotted white lines shows likely bounds for Doppler-shifted curves. These lines indicate Doppler shifts corresponding to the measured $v_{E \times B}$ at $r = 3$ cm plus and minus half the uncertainty in the measured value ($v_{E \times B} = -178 \pm 357$ m/s). A best fit value of $v_{E \times B} = 103$ m/s is calculated using a least squares fit of the shifted drift dispersion curve to $\hat{\omega}(k)$ (shown as a solid line). The only parameter in the

fit is the $E \times B$ velocity, which remains within the error bounds of the swept-probe measurements for all best-fit lines in this study. Other parameters are kept fixed at their measured values, since the uncertainty in $v_{E \times B}$ is much larger than that of the other profile quantities used as inputs to the theoretical curves. In comparison with the standard two-point probe techniques [Fig. 2.13(c)], the imaging auto-spectral density puts tighter constraints on a theoretical fit. For reference, the best-fit dispersion curve in Fig. 2.13(a) is also plotted in (b)-(d).

The measured drift frequencies do not change appreciably with radius. The theoretical radial profile of ω_* depends on the details of the plasma parameter profiles, but is determined in the Gaussian model by the (rather flat) T_e profile in Fig. 2.3(a) (for a Gaussian density profile, $k_\theta \partial n / \partial r \sim (1/r)r$). Dispersion measurements for three radii are plotted in Fig. 2.14, along with corresponding theoretical dispersion curves using a best-fit Doppler shift as above. For reference, these best fit values are $v_{\text{best}}(2 \text{ cm}) = 66 \text{ m/s}$, $v_{\text{best}}(4 \text{ cm}) = 222 \text{ m/s}$, and $v_{\text{best}}(6 \text{ cm}) = 49 \text{ m/s}$. The range of mode numbers included changes with radius, since $k_\theta \equiv m/r$. The theoretical drift dispersion matches imaging spectral-density estimates quite well at radii across the plasma column.

A low-frequency feature with poor localization in (k, ω) becomes visible in Fig. 2.14(c), and is only prevalent at large radii where the pressure gradient is low. As considered in previous work [79], there are four classes of instability that are likely to drive fluctuations in this frequency range: drift [53], centrifugal [51, 50], Kelvin-Helmholtz (KH) [51, 50], and Simon-Hoh [54, 55]. Though definitive identification of an instability requires measurements of true plasma parameters (i.e. density and potential fluctuations for comparison of phase and amplitude), dispersion properties can give an indication of what is most plausible.

Calculating the Simon-Hoh eigenfrequencies for our case requires significant modeling of the neutral profiles, which is not currently available. Although the instability cannot be ruled out, it is likely subdominant at the plasma parameters considered here⁴. Simple estimates of the neutral collision rate give $\nu_{en}/\omega_{ce} \ll \nu_{in}/\omega_{ci} < 1$.

The centrifugal Richardson number, Ri , as defined in Ref. 50, is an indication of the relative

⁴ See the discussion in Ref. 52, for example.

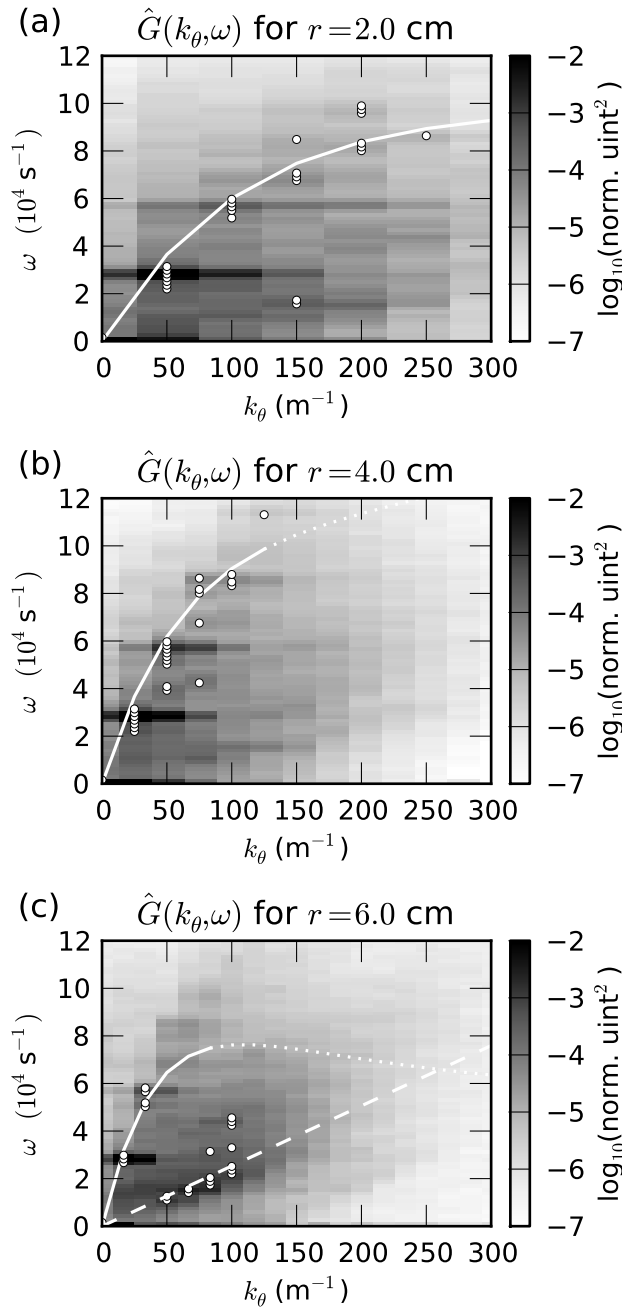


Figure 2.14: Comparison of dispersion estimates at various radii: (a) 2 cm, (b) 4 cm, and (c) 6 cm. The solid line is the theoretical curve from the Ellis model including the Doppler shift from the best-fit $E \times B$ velocity. Best fit values for $v_{E \times B}$ are $v_{\text{best}}(2 \text{ cm}) = 66 \text{ m/s}$, $v_{\text{best}}(4 \text{ cm}) = 222 \text{ m/s}$, $v_{\text{best}}(6 \text{ cm}) = 49 \text{ m/s}$. White circles represent the maxima of the k-spectra for frequencies where the total spectral power is more than 1% above background. The dashed line in (c) is the Kelvin-Helmholtz dispersion curve calculated from Eq. (2.17).

importance between centrifugal force and velocity shear. Where $Ri \ll 1$, we expect that the centrifugal instability will also be subdominant [51, 50]. An estimate using the swept-probe probe data gives $Ri \approx 0.03$. Given the large uncertainty in the swept-probe measurements, we cannot rule out $Ri \geq 1$, but we cannot say more based on the current data.

We can check whether a KH mechanism is a plausible match to the fluctuation data by approximating the velocity shear near $r = 6.0$ cm with a step-function velocity profile. In our case, $k_\theta \hat{\theta} \parallel \mathbf{u} \perp \mathbf{B}_0$, so the KH dispersion relation is equivalent to its hydrodynamic analogue [64]:

$$\omega = k_\theta \left[u_{\theta,1} \frac{\rho_1}{\rho_1 + \rho_2} + u_{\theta,2} \frac{\rho_2}{\rho_1 + \rho_2} \right] \quad (2.17)$$

where the fluid velocity u_θ and the mass density ρ are sampled at two radial points, $r_1 < r_2$. The velocities are taken from the swept-probe $E \times B$ profile, because the best-fit drift wave Doppler shift is not well constrained at $r \geq 6.0$ cm⁵. Because stratification may affect the phase speed if the density changes over the region of velocity shear, the theoretical model to which we compare includes density variations. Note that the density decreases with radius and the effective (centrifugal) gravity vector points outward, so the stratification is never stabilizing. The values of r_1 and r_2 are chosen to be the positions of the nearest swept-probe measurements on either side of $r = 6.0$ cm. There are no other free parameters in this comparison.

Fig. 2.14(c) shows $\hat{G}(r=6 \text{ cm}, k_\theta, \omega)$ with equation (2.17) overlaid for $r_1 = 5.5$ cm and $r_2 = 6.5$ cm. Based on the above considerations, the most likely candidate for driving the observed fluctuations is the Kelvin-Helmholtz (KH) instability, although further work is needed to claim definitive identification. The degree to which measurements based on visible-light intensity alone match with theoretical predictions is striking, especially since no mapping between intensity and plasma parameters is attempted.

⁵ Measurements of the drift Doppler shift above $r = 6.0$ cm were not possible due to the low number of significant points present in the imaging dispersion measurements. Even at $r = 6.0$ cm, there are no points on the drift curve for $m > 2$, meaning that the drift curve is not as well-constrained as at smaller radii. Therefore, we rely on the swept probe measurements despite the large uncertainties.

2.4.3 Implications for Dynamics

A notable feature of the measured power spectral densities is that the mode spectrum at any given frequency is quite broad, despite the presence of narrow peaks in the frequency and coherence spectra. Although much of this breadth can be accounted for by modeling the azimuthal asymmetries shown in Fig. 2.12, there remains excess power in mode numbers above the dominant m at each frequency. Nonlinearities in the system have been observed in previous CSDX experiments [57], and may play a role even in the relatively coherent regime studied here. Disentangling the relative contributions of asymmetry and nonlinearities is a delicate problem that we do not address here. While time evolution of spatial structures is especially interesting where nonlinear effects are important, and is a natural application for imaging diagnostics, care is needed when spectral features overlap in frequency or mode number.

A recent imaging study of drift waves used Fourier filtering in θ to separate out an image sequence for each mode number (Fourier component) [80]. Each filtered sequence was interpreted as a record of the time evolution of a particular mode and the subsequent analysis showed this evolution to be consistent with Kuramoto-type [81] nonlinear coupling between modes. Given the broad k -spectrum of $\hat{G}(k_\theta, \omega)$ in each of the dominant frequency bands (Figs. 2.13-2.14), filtering the images by mode number alone (across all frequencies) may not be sufficient to separate the various bands of fluctuations from each other in our case. Fig. 2.15 shows frequency spectra for image sequences filtered by mode number, each containing only a single azimuthal Fourier component. These spectra are averaged over all pixels inside a radius of 5 cm, as in Fig. 2.9. It is immediately clear that much of the power is concentrated in the same frequency bands as for the unfiltered image sequence. The difference between the spectra at low frequency may hint at non-trivial evolution, but a more sophisticated analysis is required to differentiate non-stationary or nonlinear evolution from a linear superposition of saturated modes.

While we leave a detailed investigation of temporal mode evolution for a future study, it is interesting to compare the apparent mode structures between data filtered in mode number (m)

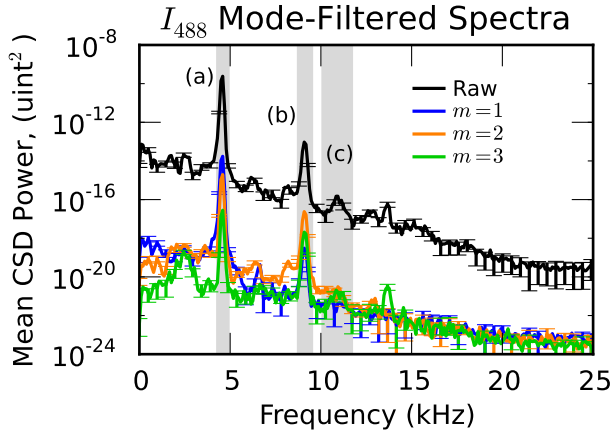


Figure 2.15: Frequency spectra of image sequences filtered in mode number, demonstrating shared frequency content. Shaded regions (a), (b), and (c) correspond to the frequency pass bands used for the filtered sequences in Fig. 2.16.

alone and data filtered in both m and frequency. If fluctuations of more than one type overlap in mode number, such as KH and drift modes, it may be necessary to consider each branch separately. As an example of the possible complications in interpreting mode evolution, Fig. 2.16 shows a sequence of three frames for the $m = 2$ image component. Each row corresponds to a different frequency filter, and each column corresponds to a particular frame. The first row shows the image sequence with no frequency filtering applied. The next three rows show the same sequence with bandpass filters applied around each of the peaks (a), (b), and (c) in Fig. 2.15. Pass-bands for these image sequences are chosen to encompass the entirety of the respective peak in the frequency spectrum $\hat{G}(\omega)$. The most striking feature of the comparison is the difference in radial structure between the various frequency contributions. Note that the amplitudes of sequences (a), (b), and (c) are of the same order, so that no one of these structures is completely dominant. More precise quantitative comparison of the amplitudes is hampered by the effects of effective integration over the exposure time. For the case at hand, the observed (integrated) amplitude decreases slightly as ω increases. The effect is relatively small because $\omega t_{\text{exp}} \lesssim \pi/2$ for the frequencies in question.

There is significant change in radial structure over a short time scale in the unfiltered case, corresponding to large variations in local amplitude. The frequency filtered sequences are (by defi-

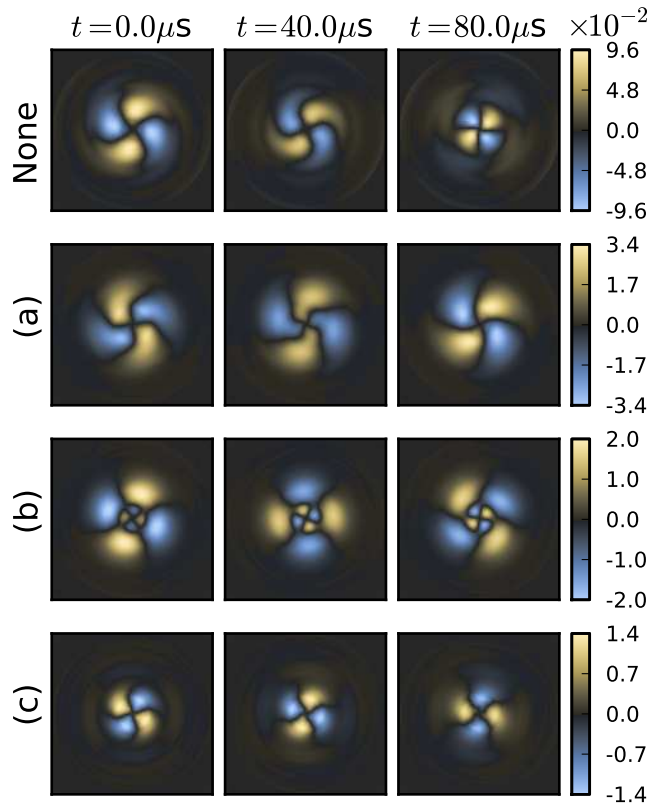


Figure 2.16: Time evolution of $m = 2$ image component with various frequency filters applied. The rows (a,b,c) correspond to the pass-bands around the peaks distinguished in Fig. 2.15. The color scale for each mode is normalized to the maximum intensity value in the entire image sequence.

nition) constrained at each radius to propagate with a quasi-steady phase velocity (ω/k), and any variations are limited to a maximum frequency corresponding to the width of the passband ($\Delta\omega$). The relative phase between radial locations, however, is not constrained by the filtering operation. Because the radial structure of each filtered sequence is steady on timescales longer than $1/\Delta\omega$, at least part of the apparent dynamics of each azimuthal Fourier component is caused by the overlap of quasi-steady structures propagating with different phase velocities. On the other hand, if the breadth of the mode spectrum is an indication of nonlinear coupling, excluding parts of the frequency spectrum from analysis of the dynamics is quite artificial. Separating nonlinear contributions to the spectrum from mode-overlap and asymmetry contributions is a difficult problem, and cannot be addressed by simple filtering. A time-frequency technique such as wavelet analysis is required to study temporal mode properties, and higher-order quantities are needed to characterize

nonlinearities.

2.4.4 Discussion of Imaging Results

We have identified the spatial and spectral structure of coherent modes in CSDX using fast-imaging data. The high quality of the power spectral density obtained from imaging allows direct comparison to theory. With the use of average profile data from Langmuir probes, we are able to suggest plausible fluctuation types by matching theoretical dispersion curves to experimental measurements. Inside $r = 6$ cm, the dominant fluctuations are consistent with cylindrical drift waves, as observed in previous work on CSDX [57]. At the edge of the plasma ($r \geq 6$ cm), a newly identified spectral feature becomes important. This new feature is consistent with transverse Kelvin-Helmholtz fluctuations, and matches well with a simple theoretical estimate. The natural extension to this work is an exploration of the full parameter space of CSDX. Detailed studies of the mode dynamics using imaging are also possible, especially with increased frame rates. Faster time resolution can be obtained by taking advantage of the wide spectral separation between ArI and ArII lines. Using broadband high/low-pass interference filters would increase the collected intensity, reduce exposure times, and allow higher frame rates.

Imaging remains a qualitative aid for many studies, because intensity cannot often be mapped onto a single physical variable for use in a theoretical model. For spectral quantities, however, quantitative comparisons may not require such a mapping. The wavelength of the collected light gives a general indication of the physics responsible for visible-light emission and therefore which plasma parameters are likely to contribute to intensity fluctuations. The frequency and wavenumber ranges of these fluctuations provide strong limitations on the relevant physics of the waves in the plasma. More subtle distinctions between possible modes can be elucidated through the phase mapping or dispersion analysis presented here.

We emphasize that the measured dispersion relations $\hat{\omega}(k)$ are obtained from imaging data alone. Although computing theoretical dispersion curves requires profile data for true plasma parameters, such data is generally available. Non-perturbative fluctuation data with high spatial

and temporal resolution, recorded simultaneously at many locations, however, is very challenging to obtain with non-imaging diagnostics. Visible light imaging can recover detailed fluctuation information on a single-shot basis, despite the lack of mapping between I_{488} and physical plasma parameters. Even so, detailed comparisons between imaging and electrostatic probe measurements are needed to understand the limitations of imaging techniques and to establish regimes where they are applicable. Preliminary work to this end is presented in Section 2.5.

2.5 Relationship between Probe and Imaging Measurements

The experimental run for this dissertation work was not optimized for probe/imaging correlations (probe and imaging data were not recorded simultaneously, to avoid introducing the probe into the images), but a small number of supplementary shots were taken with simultaneous probe and image acquisition after some imaging features failed to appear in probe data. Analysis of this data is presented here, and suggests that an in-depth study comparing the strengths and weaknesses of both diagnostics is in order.

2.5.1 Intensity as a Proxy for Density

Visible light intensity is often considered to be proportional to ion saturation current I_s [38, 33]. In principle, visible light emission is a function of many parameters, including electron, ion, and neutral densities and temperatures, as well as any auxiliary heating (such as RF waves):

$$I_{488} = f(n_e, n_i, n_n, T_e, T_i, T_n, P_{RF}) \quad (2.18)$$

In CSDX, the ions and neutrals are too cold to produce collisional excitation at the relevant frequencies ($h\nu_{488} = 2.54 \text{ eV}$, $h\nu_{750} = 1.66 \text{ eV}$). Since we use narrowband atomic line filters, we may also neglect neutral density effects for ion radiation and vice versa. In the absence of local measurements, we assume that the source microwave power is constant on the time scales of data acquisition (i.e. we may neglect P_{RF}). On the time and space scales of interest, the plasma is quasi-neutral, so that we may let $n_i = n_e$. Thus, visible emission from ions should reflect primarily

electron parameters (emission from neutrals, of course, still depends on the neutral density):

$$I_{488} = f(n_i = n_e, n_e, T_e) \quad (2.19)$$

Temperature fluctuations are generally neglected in CSDX and similar machines, as discussed in Section 2.3.2.4, so that visible light fluctuations are simply a proxy for density fluctuations ⁶ :

$$\tilde{I}_{488} \propto \tilde{n}_e + \mathcal{O}(\tilde{n}_e^2) \quad (2.20)$$

Two figures from previous work are reproduced here to illustrate the general validity of this approximation. Figures 2.17a-b show plots from Ref. 38, demonstrating high correlations between I_s , floating potential, and visible light fluctuations. Note the similarity between the time series (a), as well as the high values of the cross-correlation function (b). Similar behavior was observed in CSDX with the original plasma source [33], and is shown in Figures 2.17c-d. Note that the work in Ref. 33 was performed at similar source conditions to those described in Section 2.3, but imaging measurements recorded broadband visible light (no interference filter).

2.5.2 Correlations Between Intensity and Electrostatic Quantities

In the current CSDX source, correlations between probe quantities and visible light are rather poor. Correlations here are defined in terms of the time-lag correlation function[3]:

$$M_{AB}^k = \frac{1}{N-1} \sigma_A \sigma_B \sum_n A_n B_{n+k}. \quad (2.21)$$

A plot of the cross-correlation functions for I_{488}/I_s and I_{488}/V_f is shown in Figure 2.18. Since the probe is moving during the acquisition, the correlation time window is selected based on a small radial range around the location of interest. The time-base of the probe is $\sim 10\times$ faster than that of the camera, so probe data is interpolated at the frame times of the camera signal. In this case, approximately 3000 time points covering nearly 60 ms are used, corresponding to probe motion of 2 mm in the radial direction. In order to make the correlation as meaningful as possible, the

⁶ Work on helicon devices has observed that I_{488} is proportional to n_e^2 [82], suggesting that the dominant excitation process starts from the ionic ground state rather than the neutral ground state.

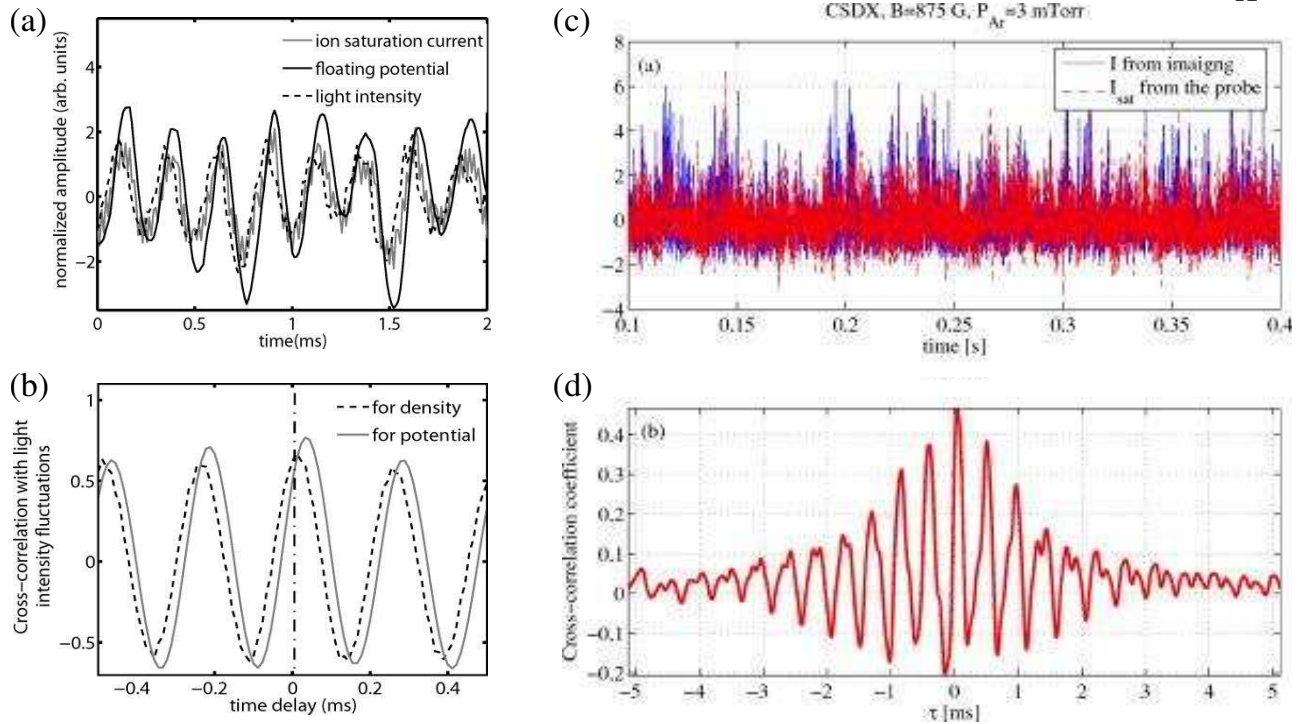


Figure 2.17: Examples of the correlation between I_s and visible light in previous experiments. (a) Time series in the Mirabelle device (Fig. 3 of Ref. 38). (b) Correlation functions in the Mirabelle device (Fig. 4 of Ref. 38). (c) Time series in the original CSDX source (Fig. 2 of Ref. 33). (d) Correlation functions in the original CSDX source (Fig. 2 of Ref. 33). (a)-(b) reprinted with permission from S. Oldenburger, C. Brandt, F. Brochard, N. Lemoine, and G. Bonhomme, Review of Scientific Instruments, 81, 063505 (2010). Copyright 2010, AIP Publishing LLC. (c)-(d) reprinted with permission from G. Y. Antar, J. H. Yu, and G. Tynan, Physics of Plasmas, 14, 022301 (2007). Copyright 2007, AIP Publishing LLC.

imaging time series used to construct the correlation function approximates the spatial resolution of the probe and follows it in space. The pixels covering an area equivalent to the projection of the probe measurement volume and just above the probe itself (+ y direction in image coordinates) are averaged together at each time to form the imaging signal. Close to the center of the plasma, the probe trajectory deviates from the radial direction, passing ~ 7 mm below the center of the column. Thus, although the pixels are displaced from the probe in the azimuthal direction for most of the probe scan, the displacement inside $r \sim 1.5$ cm is as much in radius as in azimuth, or more so.

The cross-correlations between I_{488} and I_s are surprisingly low compared to previous findings (cf. Fig. 2.17). The cross-correlations between I_{488} and V_f are somewhat higher, and the oscillations

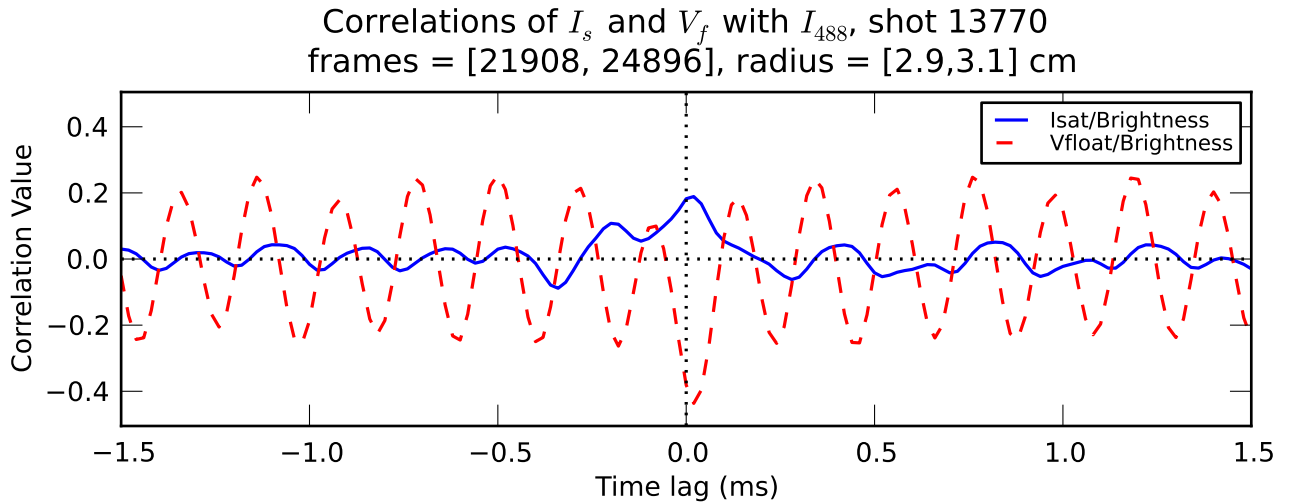


Figure 2.18: Comparison of (a) I_{488}/I_s and (b) I_{488}/V_f time-lag correlation functions at $r = 3.0$ cm. Data is taken over a small radial range because the probe is moving. This correlation calculation uses approximately 3000 time points covering nearly 60 ms.

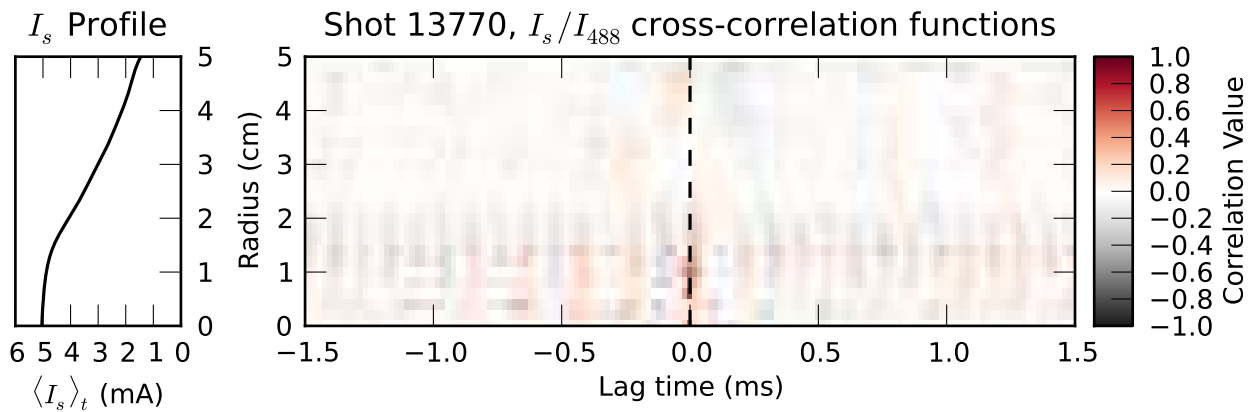


Figure 2.19: I_{488}/I_s time-lag correlation functions across the plasma radius. Pixels are chosen to match the probe radial position for each radial bin of width 1 mm. The time-averaged normalized I_s profile is shown at left for comparison.

in the correlation function are more regular. Note that V_f is **anti**-correlated with I_{488} at zero lag. These features persist across the plasma radius. Figure 2.19 shows the cross correlation function for I_{488} and I_s as a function of radius and time lag. The correlations are weak almost everywhere, with the peak values near ~ 0.4 occurring near the center. The nearest peak to zero time lag is displaced slightly because of the azimuthal drift of the plasma in combination with the primarily

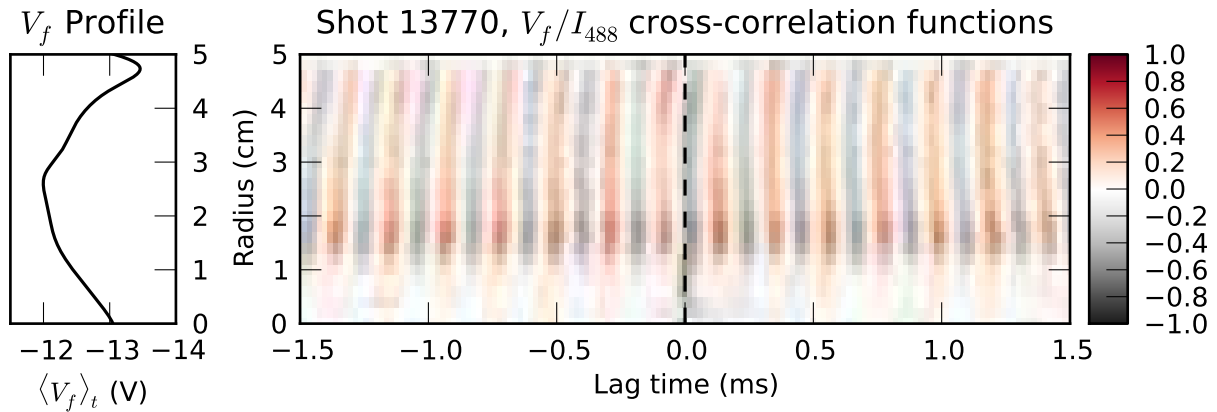


Figure 2.20: I_{488}/V_f time-lag correlation functions across the plasma radius. Pixels are chosen to match the probe radial position for each radial bin of width 1 mm. The time-average normalized $-V_f$ profile is shown at left for comparison.

azimuthal separation of the signal locations. The cross correlation function for I_{488} and V_f , shown in Figure 2.20, shows **anti**-correlations across the radius of the plasma. There is an interesting shift in the phase of the signals near $r = 5$ cm, but we cannot say much about it since the imaging and probe measurements were no longer simultaneous for probe radii larger than $r = 5$ cm.

In addition to the generally poor correlations between the two diagnostics, clear fluctuations are visible in the image sequences that do not appear in the probe profiles. For example, Figure 2.21 shows a sequence of frames from a frequency-filtered image set (shot label 12228). A narrow bandpass filter has been applied to each pixel, restricting the frequency content to the range [7.6, 7.9] kHz. No other processing has been performed. There is a clear spatial structure, in both the radial and azimuthal directions. The radial $\langle \tilde{I}_{488} \rangle$ profile, averaged over time and azimuth, shows two distinct radial ‘lobes’ (blue curve in Figure 2.22). The root-mean-square (RMS) fluctuation amplitudes for I_s and V_f , restricted to the same frequency range, do not show this structure (black and green curves, respectively, in Figure 2.22). Either the probe signals are dominated by other fluctuations in this frequency band, or the fluctuations measured by the imaging are not picked up by the probes.

The relationship between probe and visible-light measurements may also depend on the particular features being measured. For example, there is considerable similarity in the frequency

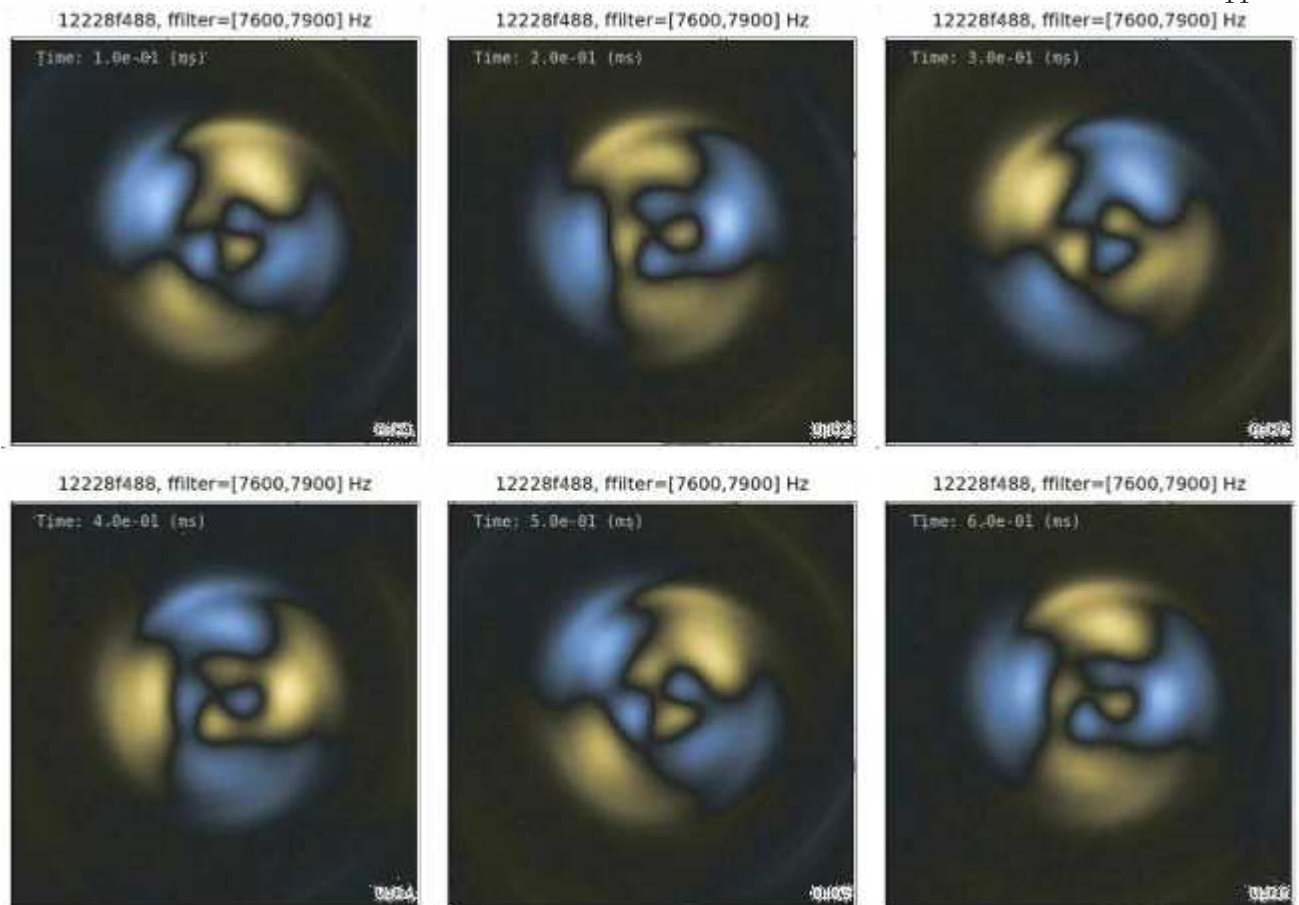


Figure 2.21: Image sequence showing fluctuations with coherent spatial structure in the [7.6, 7.9] kHz band.

content of I_s and I_{488} . Fig. 2.23 shows frequency power spectra on a logarithmic scale for each quantity. Several curves are shown to represent the structure of the spectra as a function of radius. Each spectrum is an average over a radial range of 1 cm, centered on the labeled r value. Traces are separated by factors of ten so that all are visible. The prominent peaks just below 5 and 10 kHz indicate that both I_s and I_{488} are sensitive to the dominant coherent fluctuations, in spite of the low correlation values between the two signals. It is interesting to note that the I_s spectrum does not reflect the clear fluctuations near the 14 and 18 kHz peaks in the I_{488} spectrum. Even more striking is the difference in low frequency power content. A broad feature below 5 kHz in frequency dominates the I_s spectra in the outer half of the plasma, whereas the higher-frequency coherent peaks dominate the I_{488} spectra at all radii.

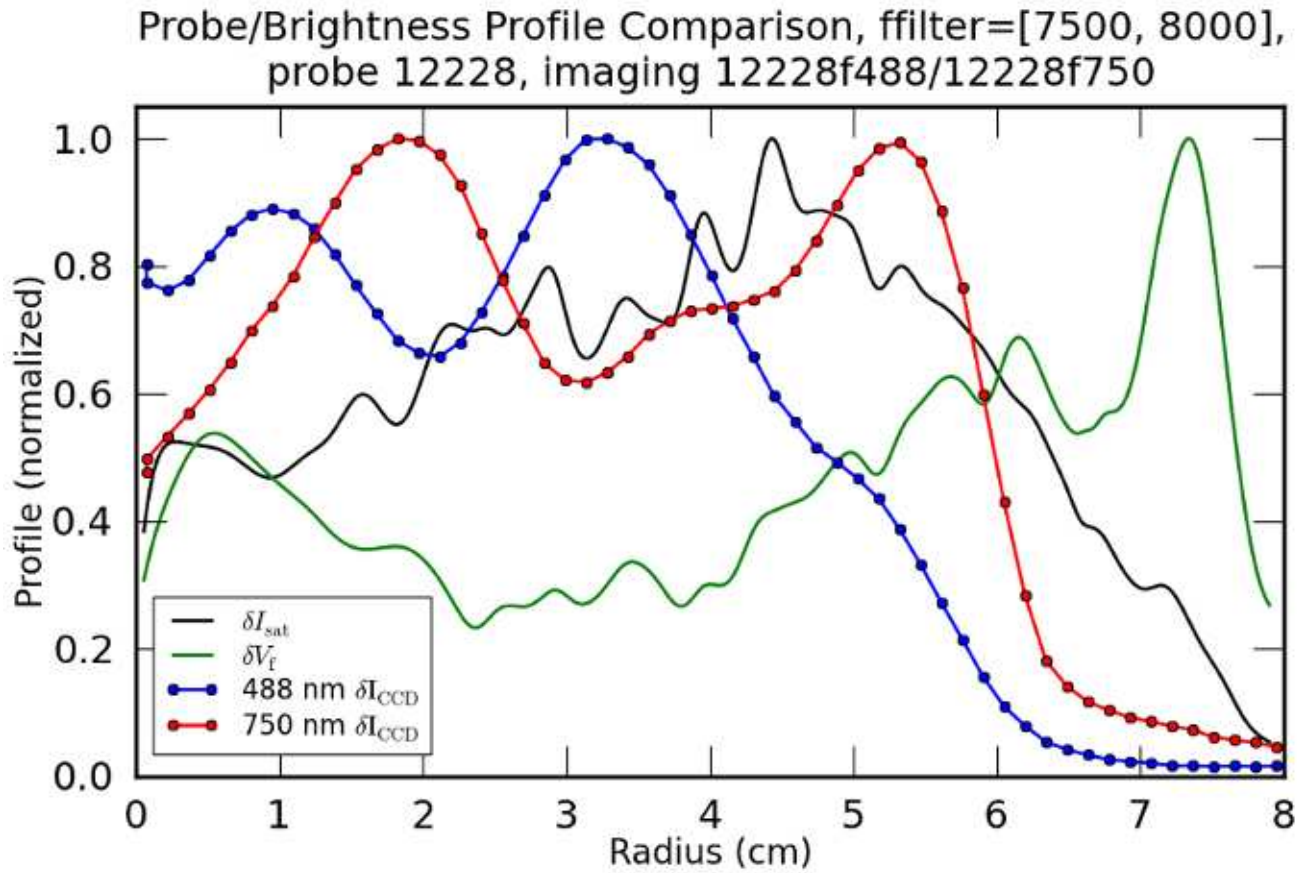


Figure 2.22: Radial fluctuation amplitude profiles for visible light and probe quantities (shot label 12228).

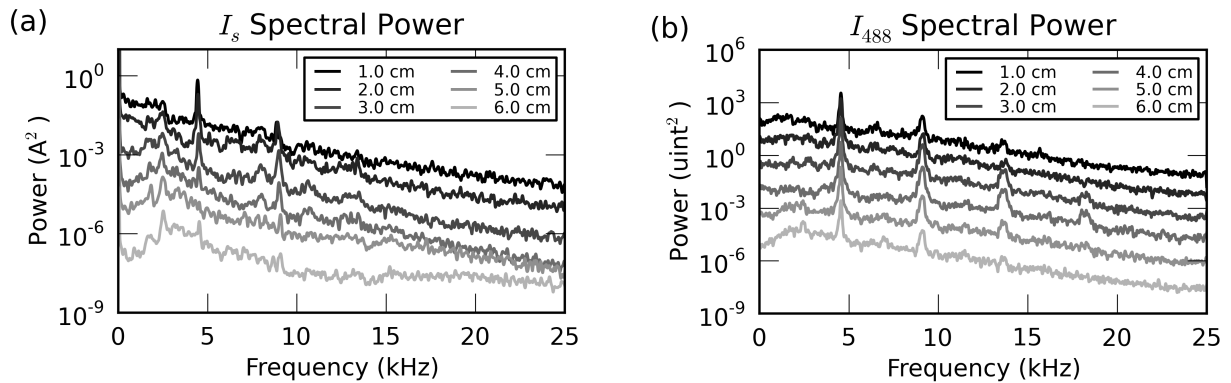


Figure 2.23: Comparison of (a) I_s and (b) I_{488} frequency spectra at various radii. The innermost radial trace is not shifted, while each successive radial trace is shifted downward by a factor of ten to allow all traces to be visible.

These findings challenge the interpretation of visible light intensity fluctuations as proportional to electron density fluctuations and suggests that closer examination of the underlying approximations is necessary. In particular, the role of electron temperature fluctuations should be reconsidered. No measurements of T_e fluctuations in CSDX have been made. Electron temperature fluctuations were deemed negligible in the original CSDX source for two reasons [57], as discussed in Section 2.3.2.4. First, the electron temperature gradient is much flatter than the electron density gradient (this applies to the new source as well). Since the strength of gradient-driven fluctuations is proportional to the steepness of the gradient, we should expect $\tilde{T}_e/\langle T_e \rangle \ll \tilde{n}_e/\langle n_e \rangle$ ⁷. Second, if temperature fluctuations are important, we should see their influence reflected in the fluctuation amplitudes of I_s and V_f . The relative fluctuation strengths, $\tilde{I}_s/\langle I_s \rangle$ and $\tilde{V}_f/\langle T_e \rangle$, reflect different functional dependences on $\tilde{T}_e/\langle T_e \rangle$:

$$\frac{\tilde{I}_s}{\langle I_s \rangle} = \left[1 + \frac{\tilde{n}_i}{\langle n_i \rangle} \right] \left[1 + \frac{\tilde{T}_e}{\langle T_e \rangle} \right]^{1/2} - 1, \quad (2.22)$$

$$\frac{\tilde{V}_f}{\langle T_e \rangle} \simeq \frac{\tilde{V}_p - 5.18 \tilde{T}_e}{\langle T_e \rangle} \quad (2.23)$$

where the plasma potential, V_p , itself depends on the electron temperature. Because the two fluctuation amplitudes were quite similar at their common peaks (same radial location), significant electron temperature fluctuations were deemed unlikely [57]. Changes in $\tilde{I}_s/\langle I_s \rangle$ relative to $\tilde{V}_f/\langle T_e \rangle$ as a function of background field, B_z , were noted in Ref. 57, but not analyzed in the context of neglecting temperature fluctuations.

A recent paper from the ASDEX-Upgrade team [83] studied the effects of temperature fluctuations on measurements of I_s and V_f in the tokamak scrape off layer, using both simulation and experimental measurements. A primary finding is that that when T_e fluctuations are important ($L_{T_e} \simeq L_{n_e}/2$), I_s is a good proxy for density, but V_f is not a good proxy for V_p . In addition, conditionally averaged floating potential fluctuations are anti-correlated with plasma potential fluctuations. The positive correlations between I_s and V_f and the somewhat adiabatic drift-wave dynamics that have been observed in CSDX [57, 79] (implied positive correlation between $n_e \sim I_s$ and V_p)

⁷ Note that this does not consider the possibility of non-gradient-driven fluctuations.

seem to indicate that the current CSDX source is likely not in the regime studied in Ref. 83, but further work is needed to confirm this.

A suggestion for reconciling the positive correlation between I_s and V_f with the disparity between the correlation functions of each with I_{488} is based on the relative sensitivity of the three quantities to T_e fluctuations. For ease of notation, we define $\hat{T}_e = \tilde{T}_e/\langle T_e \rangle$, $\hat{n} = \tilde{n}_e/\langle n_e \rangle$, $\hat{I}_s = \tilde{I}_s/\langle I_s \rangle$, and $\hat{V}_{p,f} = \tilde{V}_{p,f}/\langle T_e \rangle$. For the sake of simplicity in our suggestion, we assume that $\hat{T}_e \ll 1$, as indicated by the above considerations, and that the emission intensity should not depend on the plasma potential directly. The sensitivities for the probe quantities are then (cf. Eqns. 2.22-2.23)

$$\frac{\partial \hat{I}_s}{\partial \hat{T}_e} = \frac{1}{2} \frac{[1 + \hat{n}]}{[1 + \hat{T}_e]^{\frac{1}{2}}} \simeq \frac{1}{2} (\hat{n} + 1) \left(1 - \frac{1}{2} \hat{T}_e \right), \text{ and} \quad (2.24)$$

$$\frac{\partial (\hat{V}_f - \hat{V}_p)}{\partial \hat{T}_e} \simeq -5.18. \quad (2.25)$$

Determination of I_{488} sensitivity is slightly more complicated. A small number of studies explore the parameterization of argon emission from helicon-generated plasmas [82, 84, 85]. The last calculates I_{488} sensitivity at parameters closest to ours ($n_e = 10^{12} \text{ cm}^{-3}$) and suggests that the sensitivity is large. The data from Figure 6.11 of Ref. 85 is reproduced here in Figure 2.24 to demonstrate the full sensitivity curve derived from a collisional-radiative model (validated by experimental measurements). A finite difference estimate of $\partial I_{488}/\partial \hat{T}_e$ derived from the same data is shown in Figure 2.25. Here, the normalization is done with respect to a reference temperature of 3.2 eV. The estimated sensitivity of \hat{I}_{488} to \hat{T}_e is as high as 12/eV between $T_e = 2.5$ and 3.0 eV.

In order to make a concrete comparison of the sensitivities described above, the estimated fluctuation level of each quantity is evaluated for the parameters $n_e = 2 \times 10^{12} \text{ cm}^{-3}$, $T_e = 3.2 \text{ eV}$, and $\hat{n}_e = 0.1$, with $\hat{T}_e = 0.05$ or 0.1. The results are shown in Table 2.1. For the intensity calculation, the sensitivity was averaged over $\hat{T}_e = 1 \pm 0.05$ or 1 ± 0.1 . If the relationship between the plasma potential and the density is known, the high sensitivity of the relationship between floating and plasma potential should make any finite temperature fluctuations readily apparent.

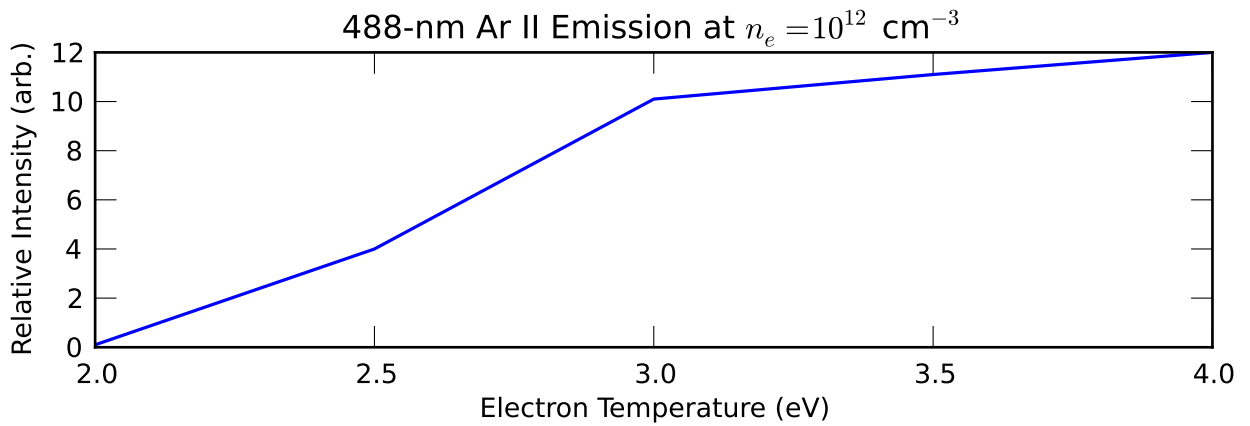


Figure 2.24: Comparison of experimental intensities with collisional-radiative model for the relevant 488-nm argon line (reproduced from Fig. 6.11 of Ref. 85). Note that temperatures are normalized to 3 eV.

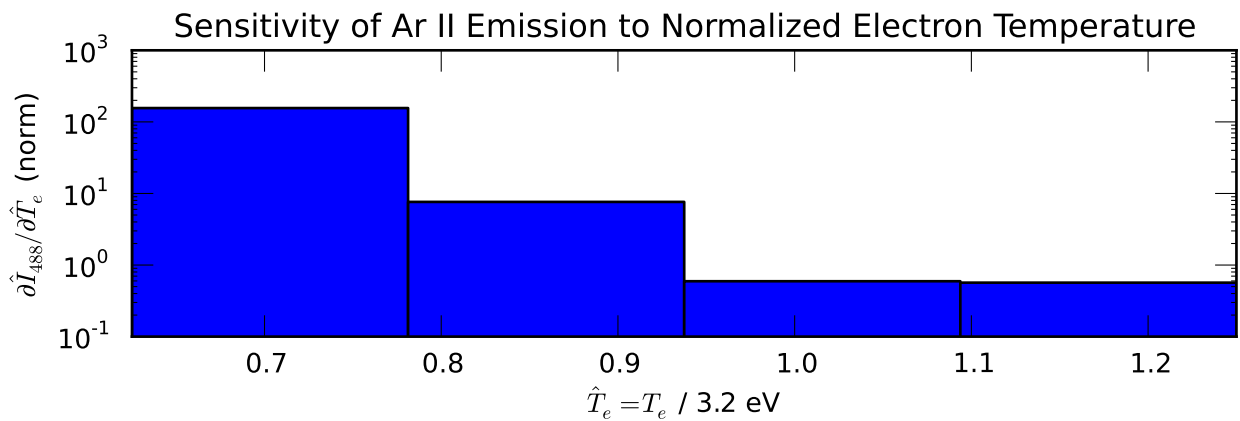


Figure 2.25: Finite difference estimate of emission sensitivity to electron temperature derived from Fig. 6.11 of Ref. 85.

Quantity	$\hat{T}_e = 0.05$	$\hat{T}_e = 0.1$
$\frac{\partial \hat{I}_s}{\partial \hat{T}_e}$	0.5	0.5
$\frac{\partial(\hat{V}_f - \hat{V}_p)}{\hat{T}_e}$	-5.2	-5.2
$\frac{\partial I_{488}}{\partial \hat{T}_e}$	0.6	1.9

Table 2.1: Comparison of partial derivatives of with respect to normalized electron temperature fluctuation amplitude. If the dynamics are adiabatic ($V_p \sim n_e$), the high sensitivity of $(\hat{V}_f - \hat{V}_p)$ to the temperature fluctuation level should make it obvious when temperature fluctuations cannot be neglected.

The quasi-adiabatic electron approximation that has often been invoked in CSDX and similar experiments assumes that normalized electron density fluctuations and normalized plasma potential fluctuations are nearly proportional, with the possibility of a small phase shift, δ :

$$\frac{\tilde{n}}{\langle n \rangle} \simeq \frac{e\tilde{V}_p}{\langle T_e \rangle} (1 - i\delta). \quad (2.26)$$

As discussed above, temperature fluctuations are usually neglected. If these approximations are valid, the maximum time-lag correlation value between the ion saturation current, I_s and floating potential, V_f should be close to one. In the opposite (isothermal electron) limit, density and potential are completely decoupled and the maximum correlation value should be close to zero. The dissertation of M. Burin [79] discusses at length the variation in adiabaticity in the original CSDX source. The usual parameterization is that of Hasegawa and Wakatani [86], $C_1 = k_{\parallel} v_{th,e} / \nu_e \omega_{ci}$. For $C_1 \ll 1$, the electron parallel dynamics are not affected by collisions on the time scale of the ion motion and the response is adiabatic. This limit can be described by the single-field model of Hasegawa and Mima [87], where density and potential are equivalent. For $C_1 \gg 1$, electron collisions dominate, and the electron density is completely decoupled from the potential. For $C_1 \sim 1$, density and potential are coupled, but not tightly enough that the evolution can be reduced to a single-field equation. This intermediate regime requires at a minimum the coupled system of differential equations of the Hasegawa-Wakatani model [86]. For the parameters used in this study, C_1 is of order unity, placing the plasma dynamics squarely in the two-field regime. We should therefore expect that the density and potential should be somewhat correlated, but not perfectly so. A plot of the time-lag correlations between probe tips aligned along the background magnetic field is shown in Figure 2.26. The zero-time correlation value between I_s and V_f is ~ 0.4 , suggestive of an intermediate adiabaticity regime and in agreement with previous work on the original CSDX source. Given this result, we cannot simply assume that differences between the floating potential and ion saturation current profiles are due to temperature fluctuations.

Although I_{488} should be somewhat more sensitive to temperature than I_s , we cannot account for the disparity in fluctuation intensity profiles based on sensitivity alone. A logical next step is

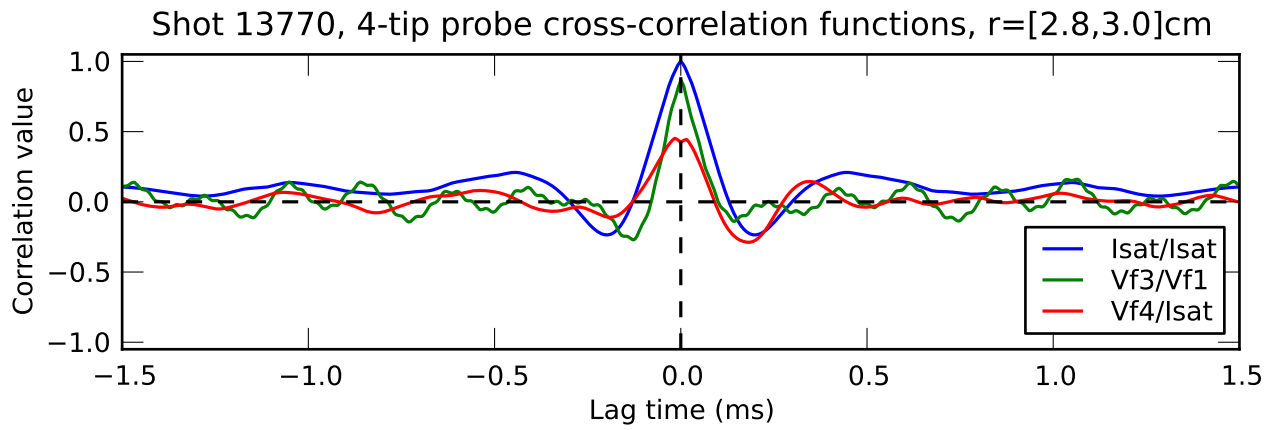


Figure 2.26: Comparison of time-lag correlation functions for field-aligned probe tips at $r = 2.9$ cm.

to attempt temperature fluctuation measurements in CSDX. The high density of helicon plasmas makes the use of emissive probes difficult, but it may be possible to construct a fast-sweep Langmuir probe [88, 89, 90], or use other fast Langmuir probe techniques [91].

Chapter 3

The Colorado FRC Experiment

3.1 Motivation and Overview

Compact toroids (CTs) are a class of plasma objects that exhibit toroidal magnetic structure in a simply connected volume [92]. No external field coils or material structures link the plasma torus, and the plasma magnetic field is generated almost entirely by internal currents. The two most-studied objects in this class of plasma configurations are the spheromak [93, 94] and the field-reversed configuration (FRC) [95, 96]. Spheromaks represent magnetically dominated plasmas with helical field structure. The poloidal and toroidal field magnitudes are similar in the bulk of the plasma. FRCs are kinetically dominated plasmas whose fields are primarily or entirely poloidal. In contrast to tokamak plasmas, whose shape and profiles are prescribed to a large degree by external manipulation, FRCs and spheromaks are self-organized objects. Both can be produced using more than one type of device, relaxing from various initial conditions to a preferred state. Because of this property, they are intriguing objects in their own right, as well as interesting candidates for possible fusion reactor applications. Self-organization is a common theme in natural plasmas, and CTs provide a unique laboratory context for studying this physics. Indeed, studying properties and dynamics of FRCs and spheromaks has given insight into various astrophysical processes [97, 98], especially magnetic reconnection [99, 100, 101, 102].

The lack of internal material structures linking the plasma makes compact toroids attractive from the perspective of fusion reactor development. Compact toroids are often produced in confinement vessels with a linear geometry, allowing for simple engineering and a natural diverter

configuration. FRCs are particularly attractive because the FRC equilibrium is intrinsically high- β (high ratio of plasma pressure to magnetic pressure). In comparison with “high” average tokamak values of $\langle\beta\rangle \sim 0.1$, FRC values are of order $\langle\beta\rangle \sim 10$ [96]. High plasma pressure suggests the possibility of fusion reactions with lower cross sections than deuterium-tritium (DT), some of which produce only charged reaction products (aneutronic). FRCs are typically ion-dominated, often with $T_i > T_e$. This suggests the possibility of a higher efficiency fusion system, with less of the energy absorbed (and radiated) by electrons. FRCs can also survive the process of translation over many axial lengths of the plasma, allowing for a fusion burn chamber to be separated from formation equipment (fewer neutron damage issues in a DT system) [96].

The Colorado FRC Experiment (CFRC) was designed to investigate turbulence and flows in a prolate field-reversed configuration. In comparison with tokamaks and stellarators, the level of turbulence measurement in FRCs has been quite rudimentary. As of 1996, “Little or nothing is known about the internal magnetic structure, fluctuations, electrostatic potentials, and flows” in FRCs [103]. Even given the significant progress made since then [96], the understanding of macroscopic stability is quite incomplete. There are hints that shear flow and kinetic effects are important, but the role that fluctuations play, directly or indirectly, in FRC formation, confinement, equilibrium, and heating is mostly unknown. Given the recent intense interest in fluctuation-driven shear flows as players in the L-H transition in tokamaks [104, 105, 106], an understanding of the role of turbulence in FRC physics is more desirable than ever.

The current chapter addresses the first four years of doctoral work contributing to this dissertation, primarily focused on the construction of the CFRC experimental apparatus. Section 3.2 addresses the theoretical context of the questions CFRC was meant to study. Section 3.3 describes the device itself, including the formation scheme and hardware (3.3.1), diagnostics for the device (3.3.2), diagnostics for the plasma (3.3.3), and the status of the machine just prior to the shutdown of the program (3.3.4). General characteristics of the plasmas produced in the CFRC are also presented in Section 3.3.4. Section 3.4 illustrates the diagnostic technique we developed to map out fluctuation properties using a multi-channel magnetic probe. An effort is made throughout to

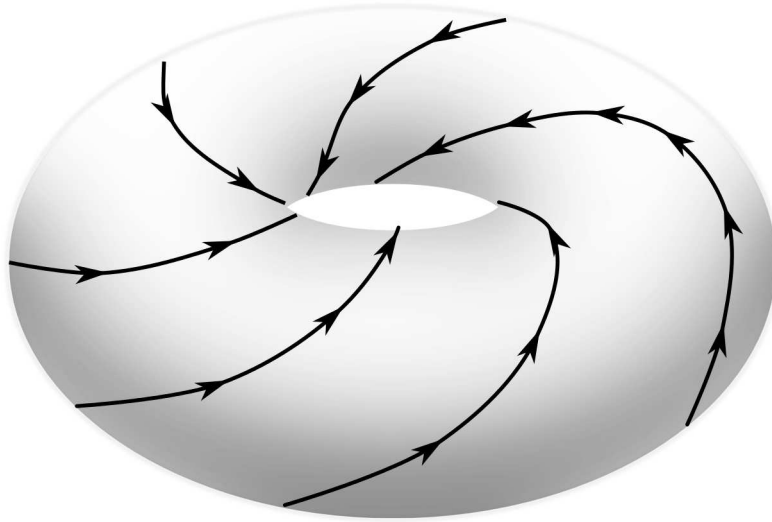


Figure 3.1: Sketch of a spheromak flux surface and accompanying field lines.

be somewhat comprehensive in the description of relevant hardware and software because it is not collected together in any other document.

3.2 Theoretical Background

3.2.1 The Spheromak and the Woltjer-Taylor Relaxation Paradigm

The CFRC formation scheme involves merging two spheromaks to form an FRC, so that a discussion of spheromak properties is necessary for understanding the operation of the machine. The spheromak is a low- β , magnetohydrodynamic (MHD) equilibrium state with nested toroidal flux surfaces, diagrammed in Figure 3.1. The magnetic fields are helical, with poloidal and toroidal fields of similar magnitude. Radial variation (magnetic shear) is parametrized in terms of the safety factor, q , as in a tokamak. The safety factor is defined in terms of the ratio of toroidal to poloidal flux at the location of each poloidal flux surface, $q(\Psi) = d\Phi/d\Psi$. In a typical spheromak, q is near unity at the magnetic axis and decreases slightly ($\sim 25\%$) towards the wall [93]. Compared to a tokamak, which can have variation in q of up to an order of magnitude, a spheromak has very little magnetic shear. Consequently, spheromaks are unstable to interchange instabilities at relatively low β . Theoretical calculations indicate a β limit of order 1%, although spheromaks have been

observed with $\beta \sim 20\%$ [93].

The modern formulation of spheromak equilibrium relies on ideas formulated in the 1950s in regards to astrophysical plasmas [107, 108, 109]. The equilibrium force condition in the MHD framework is

$$\mathbf{J} \times \mathbf{B} = \nabla P. \quad (3.1)$$

An equilibrium where the plasma pressure is small compared to the magnetic energy density obeys $\mathbf{J} \times \mathbf{B} \approx 0$ and is called ‘force-free’, since the Lorentz force is negligible. The condition $\mathbf{J} \times \mathbf{B} = 0$ leads to a field solution defined by the equation:

$$\nabla \times \mathbf{B} = \lambda \mathbf{B}. \quad (3.2)$$

The parameter λ can be any scalar function of space satisfying $\nabla \lambda \cdot \mathbf{B} = 0$. The solutions are helical, since the plasma current and the resulting field are everywhere parallel.

In 1958, Woltjer demonstrated [109] that force-free fields with constant λ represent a minimum magnetic energy state for a given magnetic helicity¹. Magnetic helicity is defined as $K = \int_V \mathbf{B} \cdot \mathbf{A} d^3r$, where \mathbf{A} is the magnetic vector potential. Helicity is a topological quantity related to the twisted-ness of the magnetic field and dates back even to Gauss [110]. In a system with no dissipation, the helicity and the magnetic energy are both conserved.

Nearly twenty years after Woltjer, Taylor argued that magnetic reconnection preserved global helicity while dissipating magnetic energy [111]. This is a consequence of the dimensional scaling of the two quantities [93], since the ratio of magnetic energy decay to helicity decay is proportional to the inverse length scale of the dissipation process. Reconnection occurs on small scales (sub-MHD), so that magnetic energy is dissipated at a much higher rate than helicity in reconnection events. Taylor’s argument provides a means for a plasma with a given helicity to relax to the minimum energy force-free state through microscopic dissipation mechanisms. For this reason, force-free magnetic field configurations are often dubbed ‘Woltjer-Taylor states’ or simply ‘Taylor states’.

¹ A Lagrange multiplier is used to apply the helicity conservation constraint during the minimization procedure. At the end of the calculation, it is this multiplier that becomes the proportionality constant between \mathbf{J} and \mathbf{B} in the solution. Hence the calculation strictly applies only to the situation where λ is a constant.

The process of ‘Taylor relaxation’ is a special case of the general self-organization framework of selective decay [112].

Solutions of the force-free equilibrium fields (Eq. 3.2) for an isolated configuration in a circular cylinder of length L can be written in terms of orthonormal solutions known as Chandrasekhar-Kendall functions [93, 113]:

$$\begin{aligned} B_r(r, \phi, z) &= -\frac{B_0}{\gamma} \left[\frac{m\lambda}{\gamma r} J_m(\gamma r) + k J'_m(\gamma r) \right] \sin(im\phi + ikz) \\ B_\phi(r, \phi, z) &= -\frac{B_0}{\gamma} \left[\frac{mk}{\gamma r} J_m(\gamma r) + \lambda J'_m(\gamma r) \right] \cos(im\phi + ikz) \\ B_z(r, \phi, z) &= B_0 J_m(\gamma r) \cos(im\phi + ikz) \end{aligned}$$

where λ is the force free parameter defined above, m is the azimuthal mode number, k is the axial wave number, $\gamma = \sqrt{\lambda^2 - k^2}$ is a separation constant, and J_m are cylindrical Bessel functions. The $m = 0$, $k = 0$ case reduces to the ‘Bessel function solution’ given by Lundquist [107]. Typically, a detached spheromak in a cylindrical flux conserver corresponds to a finite- k , $m = 0$ (axisymmetric) solution. Further discussion of the field solutions is deferred to Section 3.3.1, because the plasma in a real experiment is not isolated during formation. Flux is introduced through at least one of the walls, and this changes the boundary conditions for the solution of Equation 3.2.

3.2.2 The Field-Reversed Configuration - High β

Typical FRCs have little or no toroidal magnetic field, and consist of a region of nested toroidal flux surfaces. In cylindrical geometry, the field-line structure resembles nested ‘slinkies’ of elliptical or racetrack cross-section wrapped around the axis of the cylinder (Fig. 3.2). FRC equilibria are much more difficult to describe than spheromak equilibria for several reasons [96]. High β means that the equilibrium is far from force-free and that $\mathbf{E} \times \mathbf{B}$ and diamagnetic drifts produce the primary flows ($\mathbf{U} \perp \mathbf{B}$). Strong flow shear has been observed, especially near the separatrix [96]. In addition, FRCs are highly kinetic objects, resisting description by a pure MHD model. Not only are there field nulls at O-points and X-points (see Fig. 3.2) due to the lack of toroidal field, but the ion gyroradius is typically large compared to the overall size of the configuration.

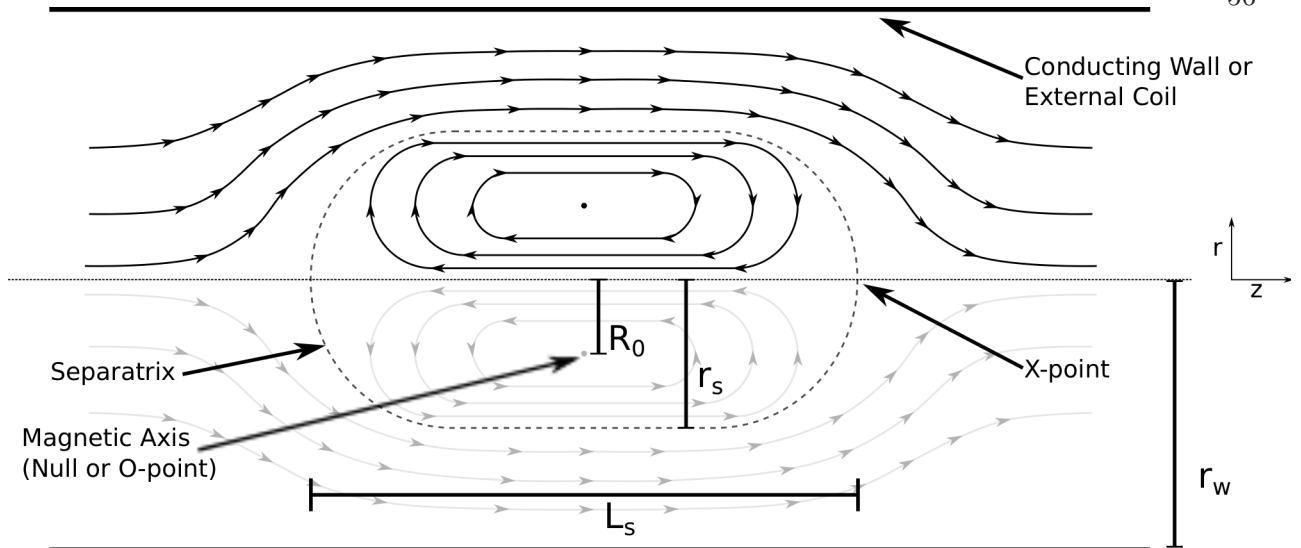


Figure 3.2: Diagram of FRC magnetic field structure in cylindrical geometry.

An important parameter for FRC scaling is the ratio between kinetic and macroscopic length scales. Three such parameters are common in the literature:

$$s = \int_R^{r_s} \frac{r dr}{r_s \rho_i} \quad (3.3)$$

is the ratio of the separatrix radius, r_s , to the average ion gyroradius, ρ_i , over the minor radius of the closed flux region;

$$S = \frac{R_0}{\rho_{i,e}} \quad (3.4)$$

is the ratio of the magnetic axis radius R_0 (field null location) to the ion gyroradius in the external field ($\rho_i, r > r_s$); and

$$S_* = \frac{r_s}{c/\omega_{pi}} \quad (3.5)$$

is the ratio of the separatrix radius to the ion skin depth. Most FRCs produced before the 1990s had $s \lesssim 2$, indicating that strong kinetic effects should be expected [95]. Even the Large S eXperiment (LSX), designed to investigate a less kinetic regime, produced FRCs with a maximum value of 8 [114, 115]. CFRC is expected to be kinetic, with $S_* \sim 1 - 3$.

FRC equilibria are also characterized by their elongation, $E = L_s/2r_s$, where L_s is the separatrix length (Fig. 3.2), and by the ratio of the separatrix radius to the inner radius of the

conducting wall or formation coil, $x_s = r_s/r_w$. Expected values of E for CFRC are 2 – 4, meaning that our plasmas will be moderately elongated and some simplifying assumptions can be made in estimating equilibrium properties.

3.2.2.1 Equilibrium

Despite the assertion that kinetic effects are strong, MHD models have proven useful in practice as first order estimates. A very simple MHD equilibrium description can be made for axisymmetric elongated FRCs ($E \gtrsim 2$). The field at the midplane is almost entirely axial, and curvature forces can be neglected. In this case, radial force balance at the midplane ($z = 0$) is simply a pressure balance:

$$P(r) + \frac{B_z^2(r)}{2\mu_0} = P_M, \quad (3.6)$$

where B_z is the axial field strength and P_M is a constant determined by the initial energy density (maximum pressure). In the case of θ -pinch FRCs, where there is an initial externally applied field B_e , $P_M = B_e^2/2\mu_0$. If we assume that the plasma pressure is only a function of poloidal flux (constant along field lines) we can calculate the location of the magnetic axis (R_0) relative to the separatrix using radial force balance. B_z points in opposite directions on the inner and outer side of the magnetic axis, so that we have from Eq. 3.6:

$$B_z = \begin{cases} \sqrt{2\mu_0(P_M - P(\Psi))} = f(\Psi) & \text{for } R_0 < r < r_s \\ -\sqrt{2\mu_0(P_M - P(\Psi))} = -f(\Psi) & \text{for } 0 < r < R_0 \end{cases} \quad (3.7)$$

where $P(\Psi)$ is the plasma pressure, written as a function of the poloidal flux coordinate. The poloidal flux function is defined by the integral of $d\Psi = B_z r dr$. Because of the assumption that the pressure is a function of poloidal flux, we also have $B_z = B_z(\Psi)$. Therefore, we can calculate the integral quantity

$$\int_0^{\Psi_M} \frac{d\Psi}{B_z(\Psi)}$$

inside and outside the null. By definition, the flux function is zero on the geometric axis and at the separatrix and maximum at the null. Thus, from the definition of the flux function,

$$\int_0^{\Psi_M} \frac{d\Psi}{-f(\Psi)} = \int_0^{R_0} r dr = \frac{R_0^2}{2}, \quad (3.8)$$

$$\int_0^{\Psi_M} \frac{d\Psi}{f(\Psi)} = \int_{r_s}^{R_0} r dr = \frac{R_0^2}{2} - \frac{r_s^2}{2}. \quad (3.9)$$

Because $f(\Psi)$ is the same function regardless of radius, we can equate the two integrals (taking care with the negative sign in the first) to recover the location of the magnetic axis:

$$R_0 = \frac{r_s}{\sqrt{2}}. \quad (3.10)$$

Measurement of the separatrix radius is useful not only for radial structure, but also for measuring the thermal energy density of the plasma [95]. When the flux conserving volume is extended enough to have approximately straight open field lines at the ends, integration of the axial component of the force balance equation produces a balance between plasma pressure and field line tension [116]. The calculation is performed by noting that $\mathbf{J} \times \mathbf{B}$ is the divergence of the Maxwell stress tensor with $\mathbf{E} = 0$ so that the MHD equilibrium condition becomes

$$\nabla \cdot \mathbf{P} = -\nabla \cdot \mathbf{T}, \quad (3.11)$$

where \mathbf{P} is the pressure tensor and \mathbf{T} is the appropriate Maxwell stress. This equation can be integrated over a volume encompassing the transition from closed to open field lines (from $z = 0$ to $z \gg L_s$) and converted to a surface integral using Gauss' theorem. In our simple model, we assume $\mathbf{B} = B_z \hat{\mathbf{z}}$ at the midplane and far from the midplane, as well as zero plasma pressure outside the separatrix. Contributions to the surface integral vanish except on the planes $z = 0$ and $z \gg L_s$. The equilibrium condition then reduces to:

$$\int_0^{r_s} Pr dr = \int_0^{r_w} \frac{B_z^2(r, z=0)}{2\mu_0} r dr - \int_0^{r_w} \frac{B_z^2(r, z \gg L_s)}{2\mu_0} r dr \quad (3.12)$$

where r_w is the radius of the conducting wall or external coil. If we assume a conducting boundary, the open flux at $z \gg L_s$ (no closed flux in this region) must equal the open flux surrounding the FRC at the midplane:

$$\int_{r_s}^{r_w} B_z(r, z=0) r dr = \int_0^{r_w} B_z(r, z \gg L_s) r dr \quad (3.13)$$

$$\text{so that } B_z^2(r, z \gg L_s) = P_M \left(1 - \frac{r_s^2}{r_w^2}\right)^2 \quad (3.14)$$

Given this relationship, we can express Equation 3.12 in terms of the maximum pressure defined above:

$$\int_0^{r_s} P r dr = \int_0^{r_w} (P_M - P) r dr - \int_0^{r_w} P_M \left(1 - \frac{r_s^2}{r_w^2}\right)^2 r dr. \quad (3.15)$$

Dividing by P_M and simplifying then gives

$$\langle \beta \rangle = 1 - \frac{1}{2} \frac{r_s^2}{r_w^2}, \quad (3.16)$$

where $\langle \beta \rangle = \frac{2}{r_s^2} \int_0^{r_s} \frac{P}{P_M} r dr$ is the volume averaged β inside the separatrix.

Because no large-aspect ratio approximations can be made in FRC geometry, there is only one fully analytic solution for both the open and closed field-line regions [96]. This model is not useful for describing CFRC plasmas, since it is only valid for $E = 1$. The most widely employed simple equilibrium model for elongated FRCs is the 1D rigid-rotor (RR) model [96],

$$B_z(u) = B_0 \tanh(Ku), \quad n(u) = n_0 \operatorname{sech}^2(Ku), \quad (3.17)$$

where $u = 2r^2/r_s^2 - 1$ is the (minor) radial coordinate, B_0 is the (uniform) magnetic field value far outside the separatrix, n_0 is the peak density, and K is the “shape” parameter constrained by axial force balance (Eq. 3.16). Unfortunately, this equilibrium solution, while it is a kinetic model [117], does not adequately represent observed scrape-off-layer widths or strong spontaneous flow shear [96]. Slightly more adjustable “two-point” models have been applied, but are also semi-empirical [118, 119]. Although numerous computations of FRC equilibria have been performed [95, 96], including MHD, extended MHD, two-fluid, hybrid, and kinetic, no single set of defining features has emerged. The relevance of these difficulties is that there is no well-defined single set of measurements that can verify that objects produced in CFRC are in fact FRCs. If and when

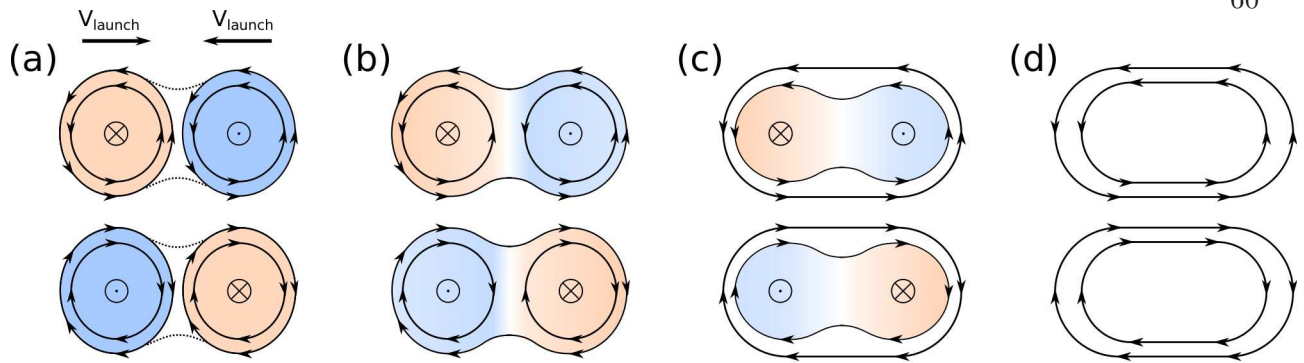


Figure 3.3: Illustration of counter-helicity merging. (a) Two spheromaks are launched towards the center of the chamber, with the same poloidal field direction but opposing toroidal fields (indicated by orange and blue shading). (b) The outer flux surfaces reconnect, creating a new poloidal flux surface around the remaining private flux regions and annihilating toroidal field. (c) The reconnection process proceeds, heating the ions (primarily) and establishing a new equilibrium. (d) When the merging process is complete, the toroidal field has been completely annihilated, leaving a purely poloidal field.

an equilibrium state is observed (see Section 3.3.4), characterization of the magnetic structure in combination with as many other features as possible will be required to demonstrate that it is an FRC.

3.2.2.2 Formation by Spheromak Merging

The formation scheme employed by CFRC involves colliding two spheromaks with opposite helicities. The poloidal fields are arranged to have the same sense, while the toroidal fields are opposite. A diagram of the process is shown in Figure 3.3. The spheromaks are launched towards one another so that the flux surfaces are pushed together (a). The magnetic fields reconnect, annihilating the antiparallel component and forming a new flux surface around the remaining private flux surfaces from the original spheromaks (b). This state is sometimes referred to as a “doublet CT” [120], or “partially-merged” configuration, with global outer flux surfaces and inner, “private,” flux surfaces. The reconnected flux surfaces establish a new self-consistent equilibrium (c), with most of the dissipated magnetic energy heating the ions [121]. If the merging process continues, all of the toroidal field is annihilated and an FRC is formed (d). FRCs have been produced by this method in several devices, including TS-3 [122, 123], SSX [120], and MRX [124].

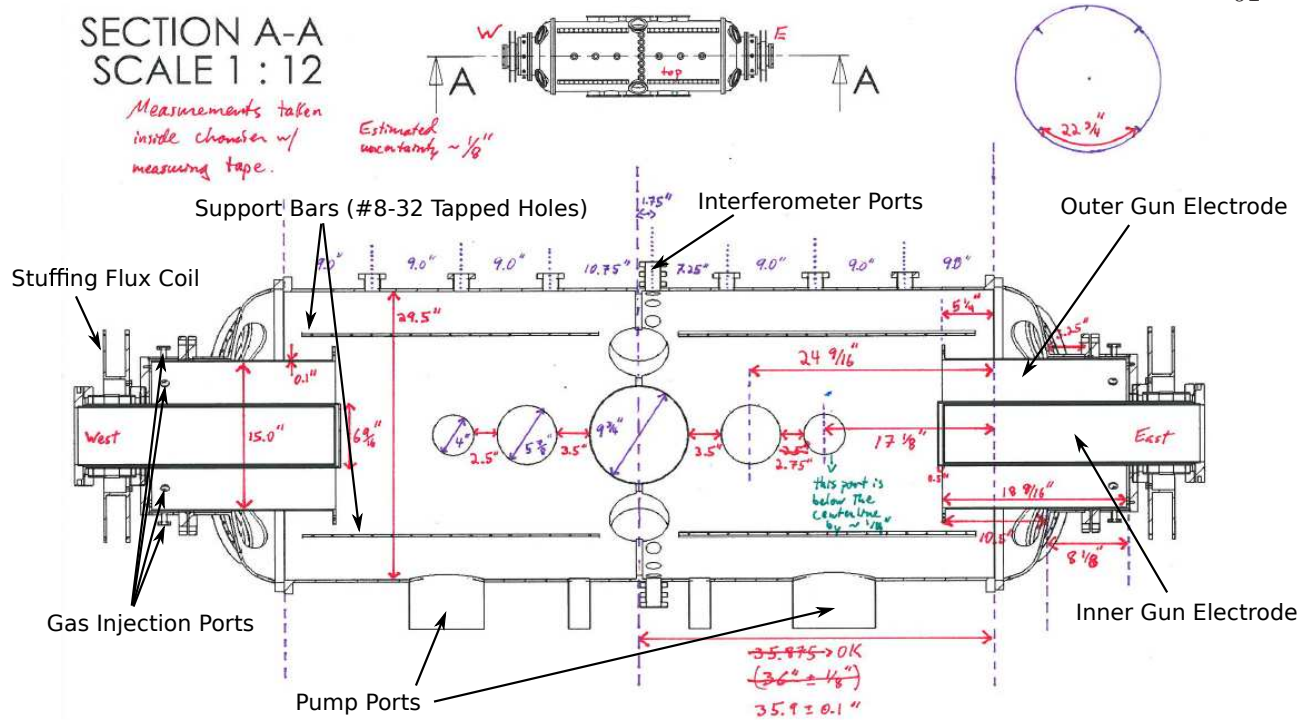


Figure 3.4: CAD cross-section of vacuum vessel showing dimensions of coaxial guns and diagnostic ports.

3.3 Device and Diagnostics

The CFRC experiment is a merged-spheromak device, with two coaxial plasma guns facing each other from either end of a cylindrical vacuum vessel. The design similar to the Swarthmore Spheromak eXperiment (SSX) [125], but has larger guns and a larger experimental volume. An annotated schematic of the vessel and ports is shown in Figure 3.4. The chamber is approximately 2 m in length and 0.5 m in diameter. The machine was designed with prolate geometry, $L/2R \sim 4$, to form and study tilt-unstable FRCs. Vacuum is maintained by two 7000 L/s diffusion pumps operated with Santovac V oil (ultra-low vapor pressure). A -30°C cold trap separates each pump from the chamber and minimizes backstreaming of pump oil. Typical base pressure is $\sim 5 \times 10^{-7}$ Torr.

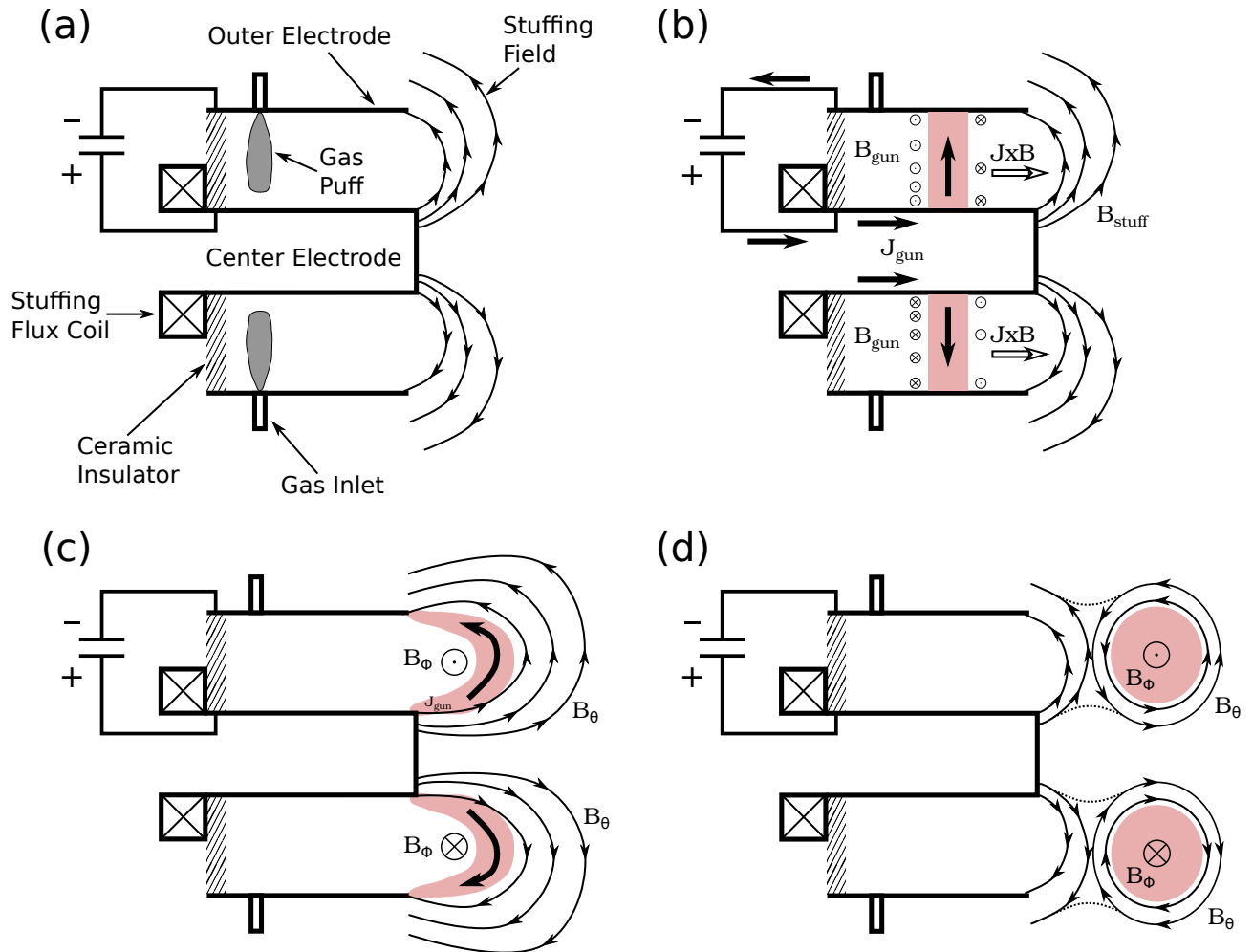


Figure 3.5: Illustration of plasma gun operation [after Ref. 126, Fig. 4]. (a) Gas is puffed into the gap between the cylindrical conductors and a high voltage is applied. (b) Arc breakdown occurs, forming plasma that carries a radial current. The plasma is pushed along the gun by the magnetic pressure of the field generated behind the current ($J \times B$ force). (c) The plasma is pushed out of the gun, and the stuffing fields are distorted by the induced currents in the plasma being ejected. (d) Distorted flux reconnects around plasma and a detached spheromak is formed (reconnected fields now supported by plasma currents).

3.3.1 Plasma Guns

Spheromaks are formed at each end of the machine by magnetized coaxial guns. The process has been described as analogous to blowing a soap bubble [125]. Typical gun operation is illustrated in Figure 3.5. Gas is puffed into the gap between two concentric, cylindrical electrodes. A high voltage is applied using a triggered capacitor bank, causing arc breakdown in the gas (a). The

current carried by the inner conductor generates an azimuthal field, and the plasma, which carries a radial current, is ejected from the gun by the resulting axial $J \times B$ force (b). In our case, the gun is seeded with ‘stuffing flux’, from a coil behind the gun. The fringing fields from this flux provide magnetic tension analogous to the surface tension of a soap film stretched across the gap. If the magnetic pressure in the gun is high enough, the plasma is ejected, carrying stuffing flux with it (c). The distended stuffing field reconnects to form a detached object (d).

A more rigorous analysis of the process can be provided in the context of Taylor states (see Section 3.2.1). The Taylor eigenvalue, λ , for objects formed in the gun can be calculated if it is assumed that the gun current changes slowly in comparison with the relevant plasma relaxation time scales. In this regime, the plasma is modeled as progressing through a series of Taylor states defined by a time-varying λ . The eigenvalue is calculated by integrating the axial component of the force-free field equation over the cross section of the inner electrode. Denoting the amount of flux connecting the electrodes as Φ_{gun} and the current carried by the electrode as I_{gun} , we have [93]:

$$\lambda(t) = \frac{\mu_0 I_{\text{gun}}(t)}{\Phi_{\text{gun}}}. \quad (3.18)$$

There is a critical value, $\lambda = \lambda_c$, at which the object being formed can access a lower energy state by disconnecting from the gun. Because the gun flux is approximately constant on the timescale of the plasma current, this corresponds to a threshold current for launching a spheromak.

Axisymmetric solutions of the force-free equilibrium fields (Eq. 3.2) allowing for open field lines (flux injection) can be written as Bessel-Fourier series [93, 127]:

$$\begin{aligned} B_r(r, z) &= -\frac{\Psi_{\text{gun}}}{2\pi} \sum_{n=1}^{\infty} c_n \gamma_n J_1(\gamma_n r) \frac{\partial S_n(z, \lambda)}{\partial z} \\ B_\phi(r, z) &= \lambda \frac{\Psi_{\text{gun}}}{2\pi} \sum_{n=1}^{\infty} c_n \gamma_n J_1(\gamma_n r) S_n(z, \lambda) \\ B_z(r, z) &= \frac{\Psi_{\text{gun}}}{2\pi} \sum_{n=1}^{\infty} c_n \gamma_n^2 J_0(\gamma_n r) S_n(z, \lambda) \end{aligned}$$

where $\gamma_n = x_{1n}/r_{\text{gun}}$ are the normalized roots of J_1 , c_n are the dimensionless expansion coefficients,

and

$$S_n(z, \lambda) = -\frac{\sinh\left(\sqrt{\gamma_n^2 - \lambda^2}(z - L)\right)}{\sinh\left(\sqrt{\gamma_n^2 - \lambda^2}L\right)}.$$

The boundary conditions here assume that flux is only injected from the $z = 0$ boundary and that other walls are flux conserving. These solutions demonstrate a topological transition from sinh-like to sine-like axial field dependence when λ exceeds the first normalized Bessel root, γ_1 . At this point, fields begin to fill the volume of the cylinder. Although closed flux surfaces do not begin to form until there is a local maximum in $S_n(z)$ away from $z = 0$ [93], the launch threshold is typically determined by the onset of topological change[125]:

$$\lambda_c = \gamma_1 = 3.83/r_{\text{gun}}. \quad (3.19)$$

For the CFRC plasma guns, $r_{\text{gun}} = 0.19$ m corresponds to the outer electrode radius, and a launch threshold of $\lambda_c = 20.1 \text{ m}^{-1}$. For the chamber itself, $\lambda_c = 10.2 \text{ m}^{-1}$, so that objects protruding from the gun may detach at a lower gun current than the gun-geometry threshold.

Status notes:

In a typical implementation, the stuffing field is tailored to maximize the flux linking the electrodes. Some implementations use a solenoid inside the center electrode, with optional shaping coils [128, 129]. SSX, which the CFRC was largely modeled after, uses a slug of high-permeability material inside the center electrode that acts as a guide for flux generated by an external coil [130]. Ideally, this guide is matched to the inner radius of the stuffing flux coil, so that all of the flux generated by the coil is captured in the guide. Such a configuration confines the stuffing flux radially, so that it only exits the center electrode cylinder through the circular end-cap. This allows straightforward calculation of the gun flux, given the parameters of the coil. In our case, the permeable guide was never procured, so the gun field is essentially dipolar. The formation process may differ from that of SSX and other spheromak experiments due the resulting geometry of the stuffing field, which is distributed throughout the gun volume rather than being concentrated at the muzzle.

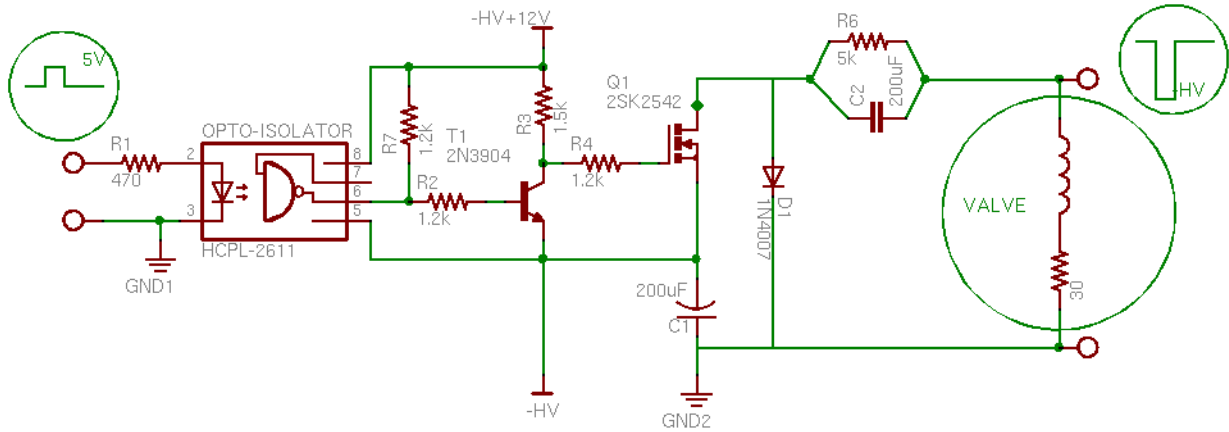


Figure 3.6: Circuit diagram for gas valve driver.

3.3.1.1 Gas Injection

The plasma guns operate by arc breakdown between two coaxial electrodes. Eight ports are drilled through the outer electrode near the back to inject gas into the gap (Fig. 3.4). These ports allow up to eight fast puff valves to operate in parallel. Currently, only two valves per gun are in operation. Rather than manufacture entirely custom gas puffers as other groups have done [131, 132], we employ Parker/General Valve model #099-0036-900 solenoid valves driven by a custom pulse circuit [133]. The valves are driven with a 400 V pulse (beyond the 270 V rating) to decrease the response time. Our short pulse durations ensure that the high drive current does not burn out the solenoid (operated successfully for hundreds of shots). For reference, a diagram of the pulse circuit as implemented² is shown in Figure 3.6. The opto-isolator allows the trigger ground and the valve (vessel) ground to be independent. T1 re-inverts the isolated pulse so that when the trigger (5V) input is high, Q1 conducts. This allows current to flow through the valve, which is protected from long input pulses by the high-pass filter, C2/R6. The shunt diode, D1, protects Q1 from the inductive kick of the valve at turn-off. Six driver channels are installed to provide room for extra valves to be added.

Although the valves are rated for pressures up to 1250 psi, they are typically operated at

² Note that the diagrams in Ref. 133 do not reflect the circuit as constructed. If you have read this sentence and can track me down, I will buy you a beer.

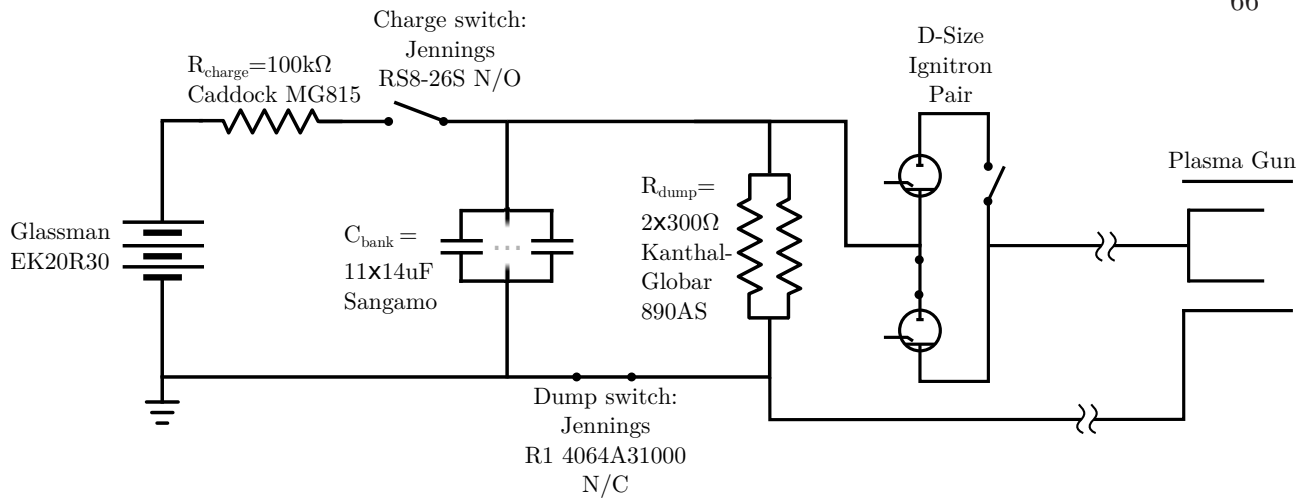


Figure 3.7: Circuit diagram for capacitor bank operation.

150 psig. Higher pressures would increase the throughput and allow for more peaked gas injection, but we are limited by the need for electrical breaks in the gas lines that feed the valves (required to break ground loops). Current lines are primarily 1/4" copper refrigerator tubing, with electric breaks made of 1/4" HDPE (rated to 456 psi) or LLDPE (rated to 358 psi) tubing.

3.3.1.2 Pulsed Power

Each coaxial gun is powered by a 154 μF capacitor bank (11 parallel 14 μF oil capacitors). The capacitors are rated up to 20 kV, for a maximum stored energy of ~ 60 kJ per gun. Both banks of capacitors are enclosed in an expanded metal cage with an independent ground. The cage prevents physical access to energized high-voltage equipment, since the cage door operates an interlock switch (N/O). Each bank is powered through a charge/dump circuit, controlled by interlocked vacuum relays. The diagram for the circuit is shown in Figure 3.7.

During operation, the charge switch is closed and the dump switch is opened. The high-voltage supplies are set to the desired charge voltage, and the capacitors charge through R_{charge} . Discharge of each capacitor bank is controlled by an optically-triggered ignitor pulse (Northstar High Voltage IG5F2) which energizes a D-size ignitron switch. Two ignitrons are installed for each bank, one with the anode grounded to the vessel and the other with the cathode grounded to the

vessel. This allows the discharge polarity to be changed with minimal intervention. Figure 3.7 shows the connections for operation with a positively charged bank. When operations are complete, the stored energy is dissipated by the dump resistors, each rated for 43 kJ. Because the dump switch is spring loaded, the capacitor bank automatically dumps if any interlock condition is violated. In addition to the charge/dump relays, the interlock system includes switches for normal operation, as well as a safety switch on the door to the capacitor cage, and an emergency dump switch near the operations computer console.

Aluminum buswork connects the capacitors to each other and to the transmission hardware. Current is delivered to each gun via 8 parallel RG-217/U coaxial cables. The inner conductors are attached to the buswork and to the gun via brass compression and pipe fittings so that they can be easily disconnected and reconnected.

Status notes:

The charge resistors were designed for lower current, and tend to overheat at high charge voltages (new supplies can source the maximum $V_{\text{cap}}/R_{\text{charge}} = 20 \text{ mA}$ current at $V_{\text{cap}} = 20 \text{ kV}$). As a precaution, computer fans were installed near each resistor to provide forced air cooling.

3.3.2 Discharge Diagnostics

In order to monitor the operation of the device, diagnostics were constructed to measure the gun current. Changes in the plasma configuration during spheromak formation are reflected by variation in the gun impedance, defined primarily by the inductance of the plasma [93]. Thus it is desirable to have discharge diagnostics that respond on a fast timescale (reconnection timescale). The gun voltage measurement that is also necessary to calculate the plasma impedance has not yet been implemented.

3.3.2.1 Rogowski Coils

The gun current is measured using an inductive diagnostic, termed the Rogowski coil after Ref. [134]. The high current levels of the discharge and the advantages of limiting the impedance

of the capacitor bank transmission system make an in-line (resistive) measurement undesirable. A Rogowski coil is a solenoidal winding that encircles the current element to be measured. The precise shape of the solenoid is unimportant, as long as the cross sectional area and turn density is consistent along the coil. Because of this feature, coils are often wound on flexible or hinged forms so that they can be placed without interrupting the circuit under test. In contrast to a transformer measurement, the Rogowski coil output is proportional to the time-derivative of the current piercing the ring. The solenoid intercepts the magnetic field generated by the current it surrounds. The integral form of Ampere's law is the clearest way to express the convenience of the method:

$$\oint \mathbf{B} \cdot d\mathbf{l} = \mu_0 I_{\text{enc}}, \quad (3.20)$$

independent of the path of integration. For our timescales, we may neglect the displacement current. If we express the field parallel to the path of the solenoid as $\mathbf{B} \cdot d\mathbf{l} = B \cdot \hat{\mathbf{a}} dl$, where $\hat{\mathbf{a}}$ is the unit vector normal to the cross section of the solenoid, then we can express the current in terms of the captured flux. The amount of flux captured per unit length is $d\Phi/dl = nAB \cdot \hat{\mathbf{a}}$, where n is the number of turns per unit length and A is the cross sectional area of the solenoid. Thus,

$$\mu_0 I_{\text{enc}} = \oint \mathbf{B} \cdot \hat{\mathbf{a}} dl = \frac{1}{nA} \oint \frac{d\Phi}{dl} dl = \frac{\Phi}{nA}. \quad (3.21)$$

The voltage across the solenoid is given by Faraday's law:

$$V_{\text{out}} = -\frac{d\Phi}{dt} = \mu_0 nA \frac{dI_{\text{enc}}}{dt} \quad (3.22)$$

The time integral of the output voltage is therefore proportional to the enclosed current, independent of the details of the path taken by the solenoid.

Our coils are wound of 18 AWG enameled magnet wire on 1/4" polyethylene tubing. The output terminal of each solenoid is run back through the tubing so that the two electrical connections are close to one another. Each coil can be wrapped around the current element to be measured and secured with a press-fit pin matched to the inner diameter of the tubing. A photograph of one coil is shown in Figure 3.8. The output voltage from the coil drives a passive integrator with $\tau_{RC} \sim 2$ ms, whose output is digitized by the data acquisition system.



Figure 3.8: Photograph of a Rogowski coil built for measuring the plasma gun current.

3.3.3 Plasma Diagnostics

The diagnostic suite of the CFRC is designed for mapping out fluctuations, so high spatial resolution and fast time response are required. All instruments are designed to have frequency response limited only by the data acquisition rate (20 MHz Nyquist frequency). Single-point plasma properties are measured via an electrostatic triple probe and “b-dot” magnetic probes. A multi-channel interferometry system gives somewhat broad coverage of the plasma in the (r, ϕ) plane. Details of magnetic fluctuations are extracted using a 16-channel, 3-axis magnetic probe, as described in section 3.4.

3.3.3.1 Triple Probe

The triple Langmuir probe is a well-developed diagnostic for making time-resolved measurements of plasma density, potential, and temperature [75]. A simplified circuit is shown in Figure 3.9. The biased pair of electrodes is floating relative to the wall. The voltage offset of the pair relative to the plasma potential self-consistently adjusts due to electron collection so that the ion saturation current, I_s , is drawn between the biased tips (assuming the bias voltage is $\gg T_e$ (eV)). The third electrode measures the floating potential of the plasma, ϕ_f , and draws zero current by definition (infinite impedance limit). Typically, the potential of the positive-bias electrode, the floating po-

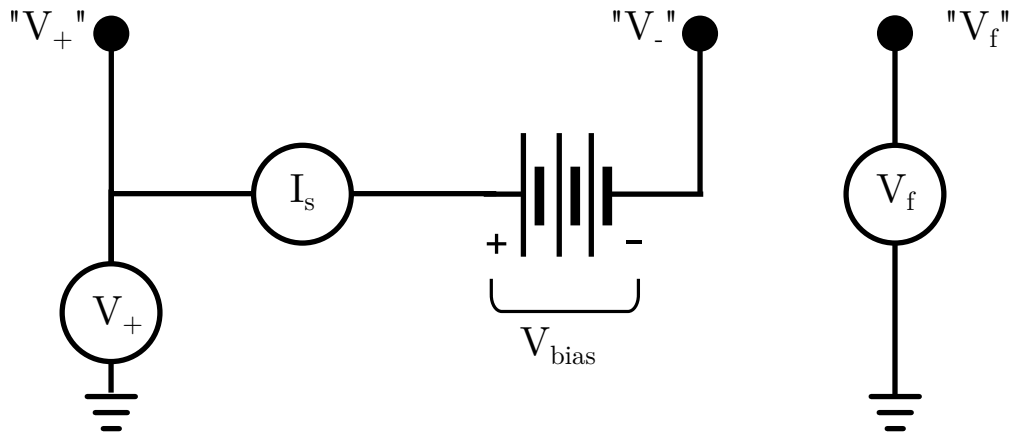


Figure 3.9: Schematic for triple Langmuir probe measurements.

tential, and the biased-pair current are measured. Electron temperature values are extracted by taking the difference between the positive bias potential, V_+ and the floating potential:

$$\frac{k_B T_e}{e} = \frac{1}{\ln 2} (V_+ - V_f) \quad (3.23)$$

The density is then easily calculated from T_e , I_s , and the effective collecting area of the probe tips, A_{eff} , since

$$I_s = en_e A_{eff} \sqrt{\frac{k_B T_e}{m_i}}. \quad (3.24)$$

Although still under development at the time the experiment was shut down, the triple probe circuit designed for the CFRC is shown in Figure 3.10. Current between the biased tips is measured using a handwound, high-bandwidth transformer. The turn ratio is 20:20, and each transformer coil is wound using 32 AWG enameled magnet wire on a Titan CF-102-Q3 ferrite toroid. The measured frequency response of the toroid is shown in Figure 3.11(a)-(b). Potentials are measured through compensated RC voltage dividers into the high-impedance load of the digitizers ($R_{DAQ} = 100 \text{ k}\Omega$). When C_1 is adjusted so that $R_1 C_1 = R_{eq} C_{eq} = (1/R_{DAQ} + 1/R_2)^{-1} (C_{cable} + C_2)$, the theoretical frequency response of the divider becomes flat [135]. The dividers are tuned in-place so that individual cable capacitances are taken into account. For reference, the values of the divider elements are: $C_1 = 3 - 30 \text{ pF}$, $R_1 = 1 \text{ M}\Omega$, $C_2 = 470 \text{ pF}$, $R_2 = 10 \text{ k}\Omega$. The measured frequency response of a capacitive divider is shown in Figure 3.11(c)-(d).

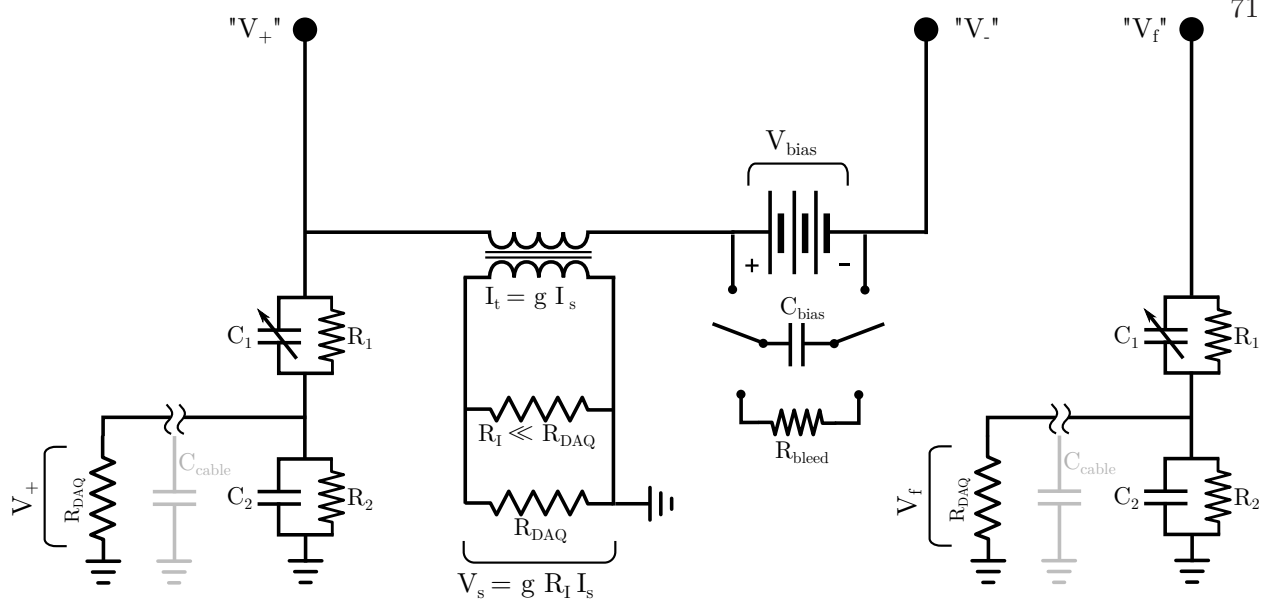


Figure 3.10: Circuit for measuring triple probe quantities in CFRC. The probe tips are labeled “ V_+ ”, “ V_- ”, and “ V_f ”, according to convention. The actual quantities measured are labeled V_+ , V_s , and V_f , proportional to positive-bias potential, ion saturation current, and floating potential (respectively).

A photograph of the physical probe built for the CFRC is shown in Figure 3.12. The probe head itself consists of three 0.5 mm-diameter tungsten wires threaded through a 3/16” outer-diameter, four-bore alumina tube. Each wire protrudes 2 mm from the alumina into the plasma. The 7” length of alumina is attached to a stainless steel tube with Torr-seal epoxy, and the tungsten wires are spot-welded onto enameled magnet wire leads. A double O-ring “Wilson” seal (MDC part # 672008) allows radial motion of the probe while the chamber is under vacuum. The probe signals are coupled to the outside through a commercial electrical feedthrough, and the circuit for recovering the signals is placed in a cast aluminum box mounted at the end of the probe assembly. The probe shaft is fixed to a linear actuator (Kerk Motion RGS6010T × 15”) to enable automated radial motion via a stepper motor (not yet installed). The entire assembly is supported by an aluminum frame bolted to the vacuum interface.

Status notes:

Four previous versions of the triple probe circuit were implemented, all of which failed to meet our requirements. A basic voltage follower isolation circuit failed due to the high common-

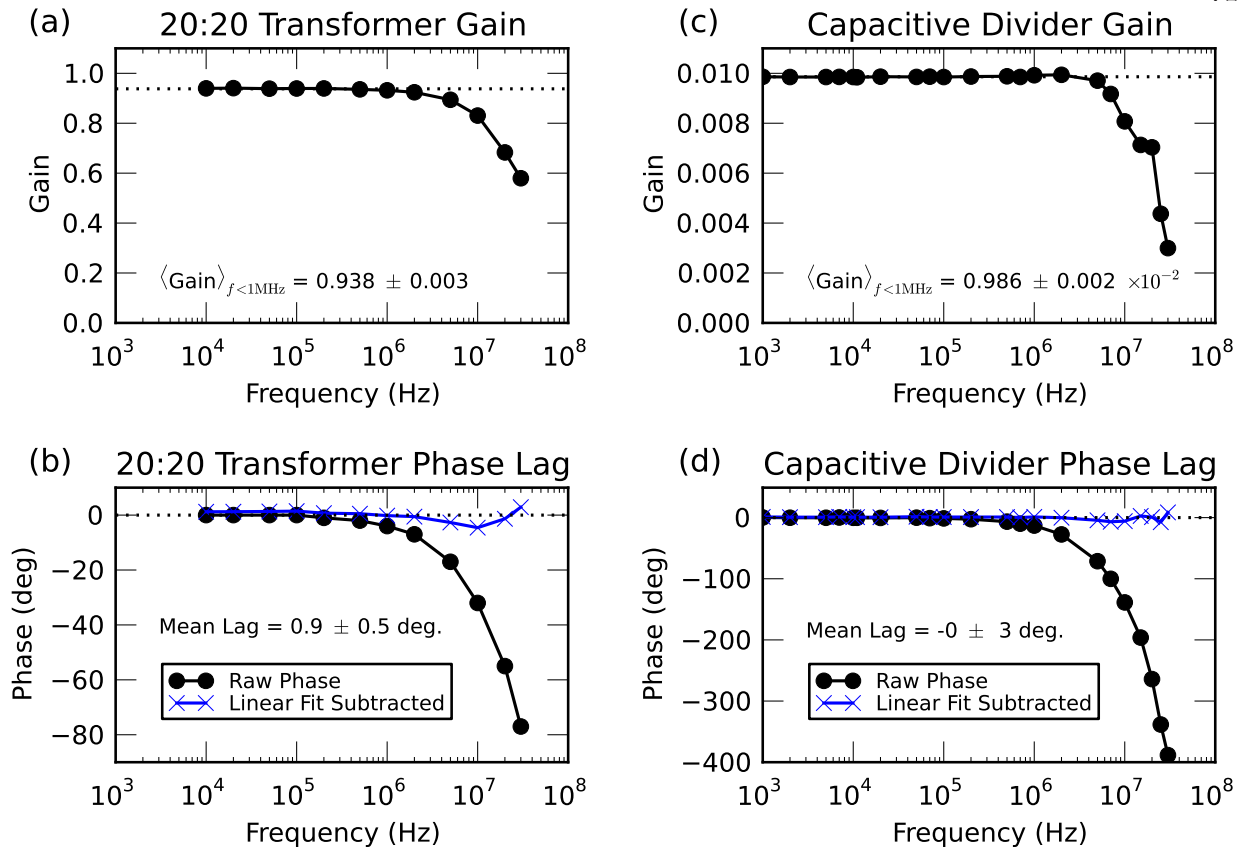


Figure 3.11: Frequency response curves for the key components of the triple probe circuit. Phase measurements also show the data with a linear fit subtracted, since the inherent time delay in the circuit will give a linear phase lag as the frequency increases. (a) Gain and (b) phase response for the I_s toroid. (c) Gain and (d) phase response for a representative capacitive voltage divider.



Figure 3.12: Photograph of the triple probe assembly.

mode voltages present on the triple probe tips. An opto-isolator-based circuit (HPCL-4562) proved too slow, with high-frequency gain cutoff frequencies on the order of 200 kHz. A transformer

scheme similar to the one detailed above was implemented, but incorrectly. The bias capacitor was connected from the low side of the battery directly to the positive probe tip, instead of being connected in parallel with the battery alone. Thinking that the transformer was to blame for the low signal strength and poor quality, the transformer was replaced by a sense resistor, R_s , and the voltage on the battery side, V_r , was measured by a third capacitive divider ($V_+ - V_R = I_s R_s$). The equally poor signal output from this circuit was only understood after the incorrect capacitor placement was discovered. The corrected circuit diagrammed in Figure 3.10 has yet to be tested on the machine.

3.3.3.2 Mach Probe

The standard electrostatic probe technique for measuring bulk velocity is the Mach probe. A Mach probe measures the ratio of ion-saturation currents between two oppositely-directed probe faces. When the velocity distribution function is a drifting Maxwellian, this ratio may be related directly to the Mach number of the ion drift speed [136] and approximated in a simple form [137]:

$$\frac{j_s^{\text{up}}}{j_s^{\text{down}}} = e^{KM} \quad (3.25)$$

where $j_s^{\text{up(down)}}$ is the current density of the upstream(downstream) probe face, $M = v_{di}/v_{th,i}$ is the Mach number, and $K = K(T_i, T_e)$ is a calibration constant. The difficulty in interpreting Mach probe measurements in magnetized, flowing plasmas has been well documented [138], but the method continues to be useful because it is relatively simple to implement.

The ion saturation current for each tip is measured by a circuit similar to that of the triple probe I_s tip. Four 20:20-turn handwound toroid transformers are used to collect the four currents. These transformers are identical to the one employed in the triple probe circuit, and the calibration is well represented by Figure 3.11a-b. A diagram of the circuit is shown in Figure 3.13.

The CFRC Mach probe is constructed of four-bore alumina tubing with a circular cross-section. A radial slot is machined through the outer alumina into each bore, creating a sheltered opening for each probe tip. Wires inserted into each bore thus form four directional collecting

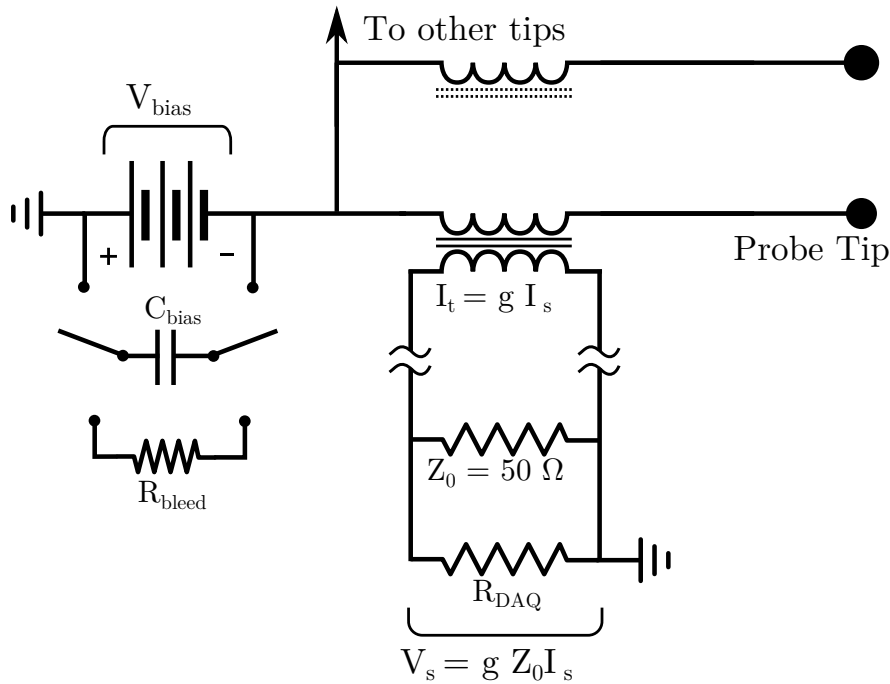


Figure 3.13: Mach probe bias and signal collection circuit. A detail of the transformer connection to the digitizer is shown for one tip. The other three tips use identical transformer arrangements.

surfaces for measurement of upstream and downstream ion current in two orthogonal directions. A photograph of the completed probe tip is shown in Figure 3.14. The rest of the probe assembly is similar to the triple probe described above (Section 3.3.3.1). Stainless steel tubing passing through a Wilson seal acts as the vacuum interface, and a linear actuator (Kerk Motion RGS6010T \times 12") provides control over the radial position of the probe tips.

Status notes:

The Mach probe was biased incorrectly (collecting electrons instead of ions) until February 14th, 2010. Any measurements recorded before this time are not useful. In addition, the version of the circuit used up until June of 2010 had an effective LC low pass filter that attenuated the output of each probe tip sequentially. The circuit presented above is designed to solve this problem, but has not yet been validated. We see sudden spikes in the currents measured by the probe, indicating that arcing may be a problem. Most measurements were taken at a bias voltage of 75 V, though values as low as 30 V were used in attempting to eliminate any arcs. At 50 V, the spikes were still observed,

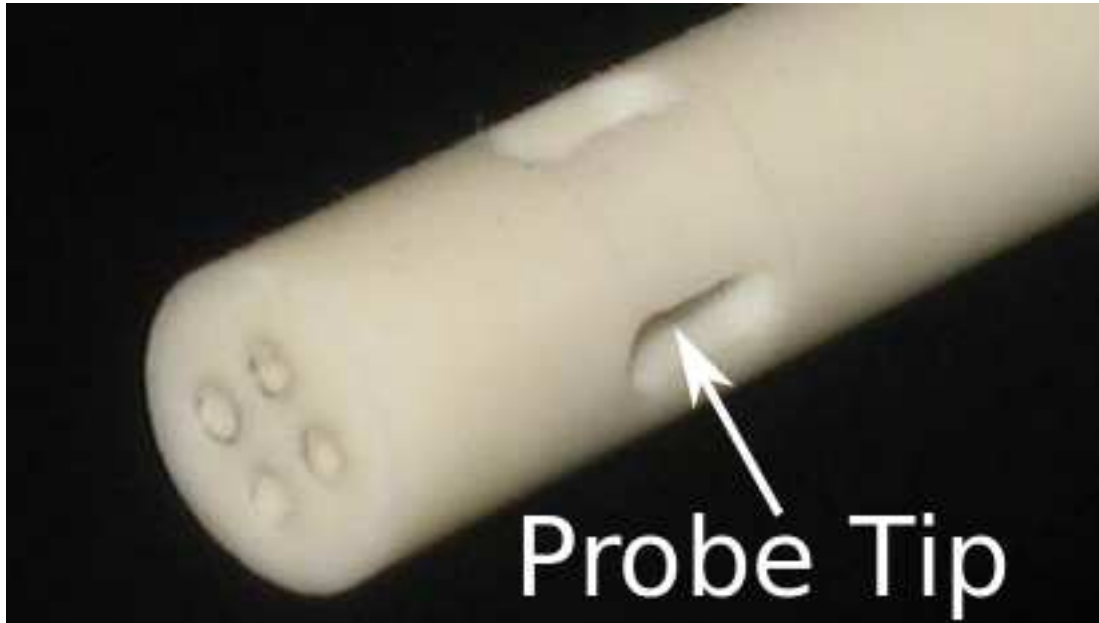


Figure 3.14: Photograph of the Mach probe head.

and at 30 V, the signals were so small that they were indistinguishable from noise. Unfortunately, we have no measurement of the electron temperature in CFRC, so we cannot constrain the voltage except by typical values from other experiments. The Mach probe is still in the development stage, and none of its data is considered valid as of yet.

3.3.3.3 Interferometer

One of the two major diagnostics for the CFRC is a multi-channel infrared interferometer, constructed as an undergraduate honors thesis project [139]. At typical laser frequencies, the electron response is dominated by plasma oscillations, with dispersion:

$$\frac{c^2 k^2}{\omega^2} = 1 - \frac{\omega_{pe}^2}{\omega^2}. \quad (3.26)$$

Since the index of refraction (ck/ω) depends on the plasma frequency, $\omega_{pe} = \sqrt{n_e e^2 / \epsilon_0 m_e}$, it is possible to measure line-integrated electron density using an interferometric phase shift according to the relation [75]

$$\int n_e dl \simeq -\frac{2cn_c}{\omega} \Delta\phi. \quad (3.27)$$

Here $\Delta\phi$ is the phase shift of the measurement beam, ω is the laser frequency, c is the speed of light, n_e is the local electron density, and n_c is the cutoff density, defined as the electron density at which the plasma frequency is equal to the laser frequency.

In order to measure an unambiguous phase shift with fast time resolution, we employ a quadrature heterodyne technique following Jacobson [140]. In a typical interferometric measurement, the detector signal is simply proportional to the intensity of the recombined signal and reference beams, averaged over many cycles of beam oscillation (represented here by angle brackets). Taking the electric field of the measurement beam to be $E_m = E_1 \cos(\omega t + \Delta\phi)$ and that of the reference beam to be $E_r = E_2 \cos(\omega t)$, the detector signal is:

$$V \propto \langle |E_1 \cos(\omega t + \Delta\phi) + E_2 \cos(\omega t)|^2 \rangle \quad (3.28)$$

$$= \langle E_1^2 \cos^2(\omega t + \Delta\phi) + E_2^2 \cos^2(\omega t) + E_1 E_2 [\cos(\Delta\phi) + \cos(2\omega t + \Delta\phi)] \rangle \quad (3.29)$$

$$= \frac{1}{2} (E_1^2 + E_2^2) + E_1 E_2 \langle \cos(\Delta\phi) \rangle. \quad (3.30)$$

Without additional information, the phase shift measurement is ambiguous because $\cos(+\Delta\phi) = \cos(-\Delta\phi)$.

In order to eliminate this ambiguity, we employ quadrature detection. A quadrature scheme involves mixing the measurement beam with two orthogonal phase references. These are termed the “in-phase” (or cosine) reference and the “quadrature” (or sine) reference, whose phase is shifted 90° relative to the in-phase reference. Mixing with two orthogonal components allows both the even and odd Fourier components of the signal to be recovered. Quadrature detection using multiple reference beams requires many more expensive optical components and twice the number of detectors, so we project the phase shift from the laser-frequency carrier to an intermediate-frequency carrier and perform the quadrature mixing using microwave electronics. The reference beam frequency is shifted by an acousto-optic modulator operating at the intermediate frequency, $\omega_{mod} \ll \omega$. When the measurement and reference beams combine on the detector face, the time-dependent interference phase shift is transferred to the modulation-frequency beat wave. This can be illustrated by repeating the above calculation of the detector signal, with the reference electric field now given by

$E_r = E_2 \cos(\omega t + \omega_{mod} t)$:

$$V \propto \frac{1}{2} (E_1^2 + E_2^2) + E_1 E_2 \cos(\Delta\phi + \omega_{mod} t). \quad (3.31)$$

Now the mixing process is repeated, this time by combining the signal with in-phase and quadrature references at the modulation frequency. Sum and difference outputs are obtained as above:

$$V_I \propto \cos(\Delta\phi + 2\omega_{mod} t) + \cos(\Delta\phi) \quad (3.32)$$

$$V_Q \propto \sin(\Delta\phi + 2\omega_{mod} t) + \sin(\Delta\phi) \quad (3.33)$$

Filtering out the component at twice the modulation frequency (low-pass) leaves one signal proportional to the cosine of the time-dependent phase shift and one proportional to the sine. The two signals together allow unambiguous determination of $\Delta\phi$.

The coherent source for the system is a CO₂ laser (Synrad 48-1KWL) operating at $\lambda = 10.6 \mu\text{m}$. The expected electron densities for CFRC are of order $n_e \lesssim 10^{22} \text{ m}^{-3}$, while the cutoff density at the laser frequency is $n_c \sim 10^{25} \text{ m}^{-3}$. For reference, a phase shift of $\Delta\phi = 2\pi$ corresponds to an electron density averaging $2.12 \times 10^{20} \text{ m}^{-3}$ across the 1 m path (two 50 cm traverses) through the plasma. Since the phase change is proportional to $\omega/n_c \sim \lambda$, using $10.6 \mu\text{m}$ light as opposed to visible light (e.g. 632 nm) increases the sensitivity by a factor of ~ 15 . The reference beam is split from the measurement beam by an ISOMET 1207B6 acousto-optic modulator driven by an ISOMET RFA221B RF driver. This model was chosen over comparable models due to its higher Q-value and increased optical isolation. The first-order diffracted beam emerges at 77.1 mrad (4.5°) with respect to the measurement beam, allowing convenient separation after propagating to the next optical element. The modulation frequency was chosen to be $\omega_{mod} = 40 \text{ MHz}$, because it is common enough to be found in stock items, within the bandwidth of our detectors, and equal to the acquisition rate of our fastest digitizers (allows interferometer time resolution to be as high as possible).

All optical components are secured to a $4' \times 2.5'$ optical breadboard, supported by a frame of 80/20[®] aluminum. The frame is mounted on rails running perpendicular to the vacuum chamber.

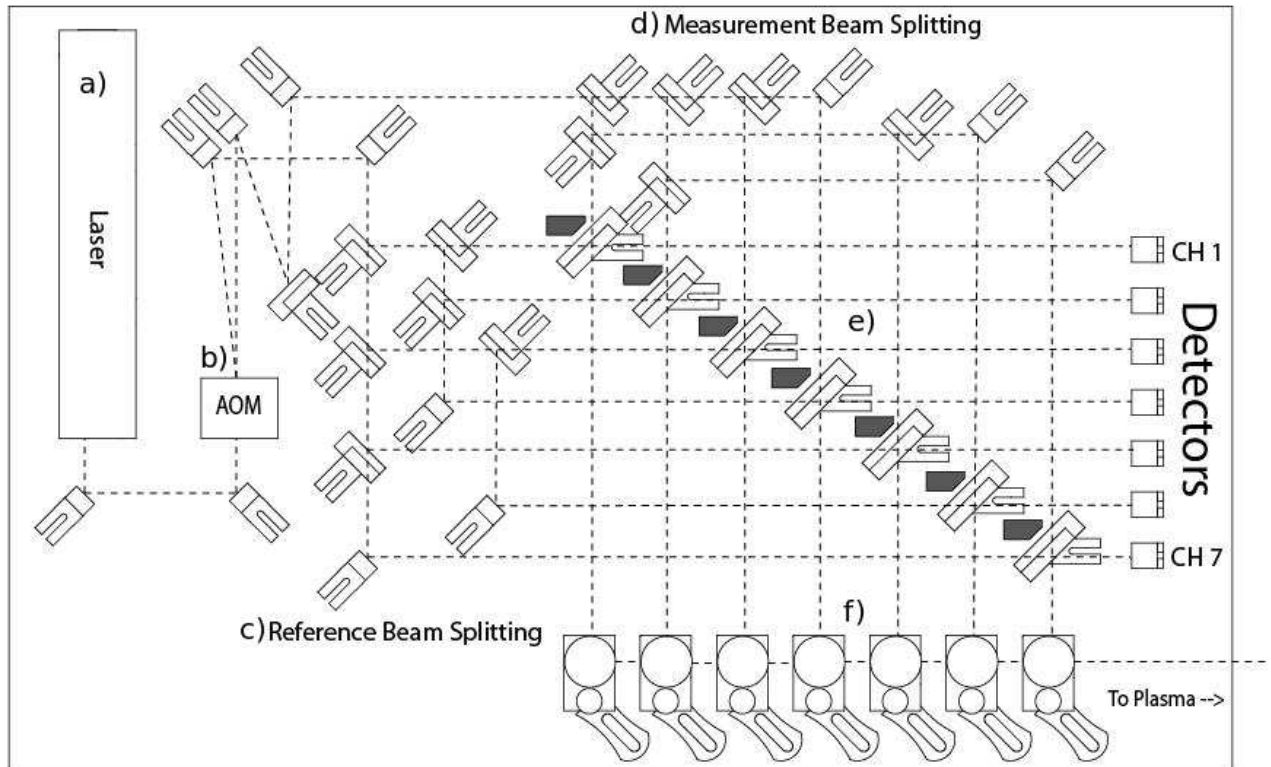


Figure 3.15: Optical table layout, courtesy of L. Ellison. a) CO₂ laser. b) 40 MHz acousto-optic modulator. c) Set of reference beam splitters. d) Set of measurement beam splitters. e) Diagonal array of beam recombining optics. f) Periscope beam-steering elements

The interferometer may be translated away from the vessel easily for simplified alignment and diagnostic port access, then placed adjacent to the vessel for measurements. To ensure that channels beyond the first could be assembled without disturbing the existing channels, the optical table configuration was designed using CAD software. Considerations taken into account include compactness, beam divergence, and preventing stray light. The final CAD representation is shown in Figure 3.15. The full implementation of the diagnostics uses seven parallel channels with three-inch chord separation, although to date only three channels have been installed. The primary optics consist of 19 ZnSe beam splitters (Lambda Research Optics IPR-5005Z-50R-10.6-45-P, with 50-50 reflection-transmission at a 45° angle of incidence). The measurement and reference sides each require six splitters to create seven beams (Figure 3.15c-d). This arrangement divides the laser output into six beams with 1/8 of the initial power and one with 1/4 of the initial power. The

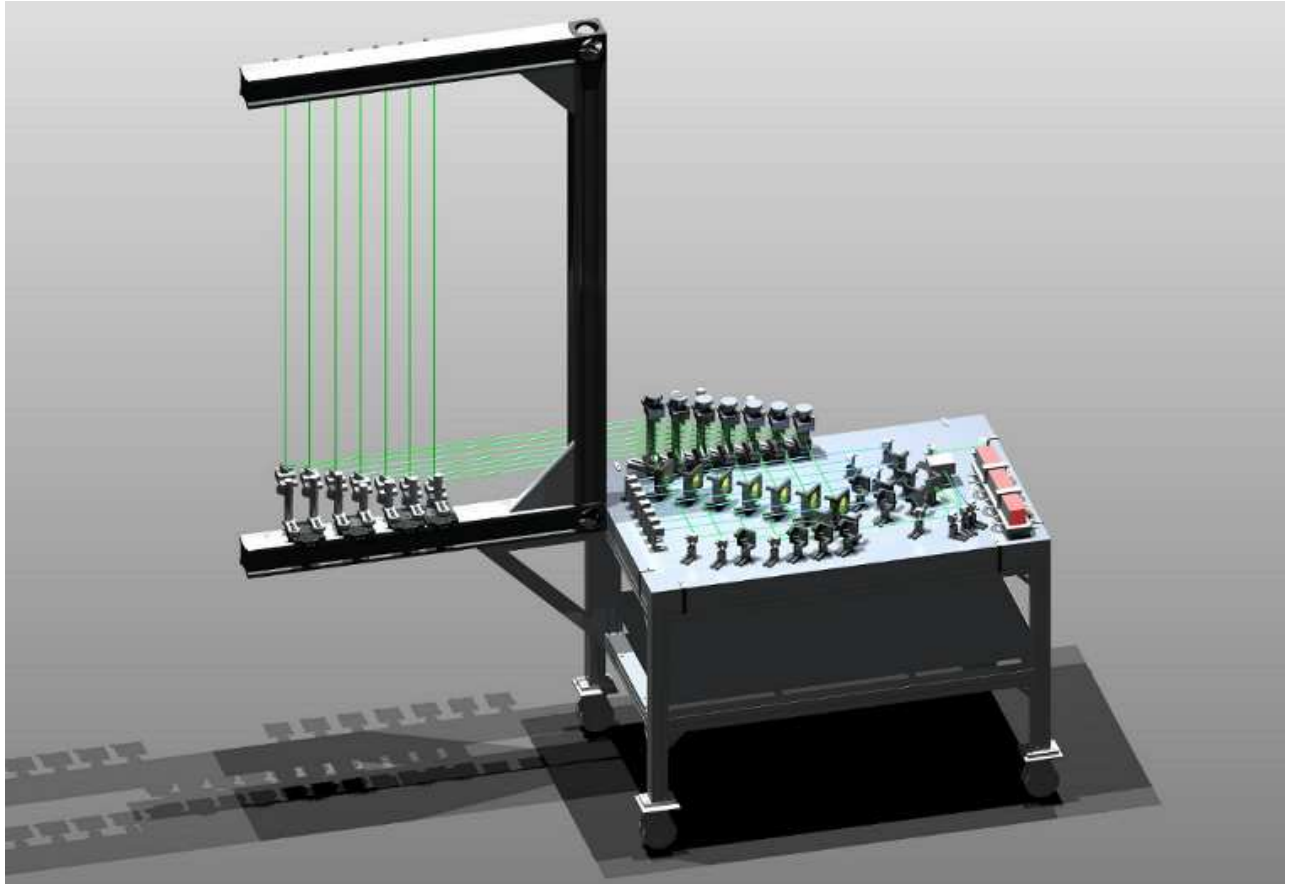


Figure 3.16: 3D SolidWorks model of interferometer, courtesy of L. Ellison.

seven recombining optics are twice as large (2" diameter) to enable separation of the outgoing and returning beams at the detectors (Figure 3.15e).

As the beams exit the table, they are vertically stacked with $\sim 1.5''$ spacing using periscope mounts (Figure 3.15f). This leaves adequate clearance for staggered beam-steering optics, which turn the outgoing beams to pass upward through the FRC vessel. Above the vacuum chamber, the beams reflect from mirrors mounted on the top optical rail. This reflection sends the beams back through the vessel with a slight angular offset to ensure adequate beam separation at the recombining optics. The 3-D geometry, including the optical rails, is shown in Figure 3.16.

Graphite beam blocks absorb the unwanted transmitted and reflected beams at the recombining optics. This minimizes back-propagation of stray light through the system so that phase measurements and laser operation are not disturbed. Similarly, the metallic faces of the detector

housings have been shielded with graphite. Each has a 4 mm diameter aperture which allows beam transmission. At the vessel interface, 2.75" conflat flanges have been adapted to hold NaCl transmission windows at a 3° angle with respect to the beam path. Any reflected light at the air/salt/vacuum interface is directed away from the system. As an additional precaution, the entire optical table is encased in acrylic, which is opaque at the laser frequency.

To manage Gaussian beam divergence, two sets of focusing optics are included. The first focusing location is shortly after the AOM separates the reference beam, so that only one focusing element is required for all seven beams (Fig. 3.15g). The second position is located at the top of the optical rails, where the beams are reflected between the first and second pass through the plasma (Fig. 3.16h). Both focusing elements are spherical mirrors. The reference beams are not focused, as the beam diameter remains sufficiently small (< 7 mm at the detectors).

Optimal focal lengths for the mirrors were determined using a Gaussian beam propagation code. The beam waist is calculated throughout the system while checking for proper clearance at each potentially limiting aperture. The optimized configuration includes a spherical mirror of focal length 1.5 m placed on the table just after the AOM and spherical mirrors of focal length 2 m at the top of the optical arms. These elements has proven satisfactory for managing beam divergence in practice (4 mm spot diameter at the detectors).

The interference signal is converted to a voltage by VIGO Systems PVM-10.6 infrared detectors. Because of the quadrature scheme, the interferometer signal becomes a 40 MHz oscillation at each detector, with a time-dependent phase shift relative to the reference modulation waveform (Eq. 3.31). Two amplifier stages (Perry 481-50X and Minicircuits ZKL-2R7+) boost each signal from ~ -51 dBm at the detector output to roughly 8 dBm at the mixer input. The AOM driver signal is combined with the amplified signal to produce sine and cosine outputs using a Mini-Circuits MIQC-60WD+ in-phase/quadrature demodulator (Eqs. 3.32-3.33). Low-pass filters remove the 80MHz component of the mixer output.

Status notes:

The electronics stage (amplifiers and mixers) is connected to the digitizer channels using

non-isolated SMA cables (shields are grounded at both ends). As a result, electromagnetic noise from the discharge is picked up by ground loops between cable shields. As a temporary mitigation strategy, most of the $\sim 19'$ cable run is shielded by galvanized steel electrical conduit with a 1.5" inner diameter.

The vertical arrangement of the interferometer beams has a strong disadvantage that was only realized close to the end of the project. Debris generated by plasma discharges settles in the lower window ports, so that the quality of the transmitted beam degrades over time. Only when the interferometer signal had degraded to an unusable level did we discover the problem. A recommendation for future operation is to inspect the salt windows on the lower interferometer ports often and clean or replace them every few months.

Additionally, we often had problems with ‘dropouts’ in the signal, where the amplitude of both the x (cosine) and y (sine) channels would simultaneously drop. A plot of $x(t)$ against $y(t)$ should trace out a circular arc, representing the time evolution of the interferometer phase shift. The dropout behavior was an abrupt reduction in the radius of the circle, corresponding to some failure of the carrier signal rather than a problem with the phase measurement. The cause was never determined with certainty, though the SMA connections were often found to be intermittent when investigating the problem (especially on channel 4). Replacing these cable ends fixed the problem temporarily on at least two occasions, but we could not eliminate the possibility of other simultaneous problems. As a mitigation strategy, the two signals are normalized to the time-varying signal amplitude corresponding to the radius of the circle ($r = \sqrt{x^2 + y^2}$).

3.3.3.4 High-Resolution Magnetics Array

The second major diagnostic implemented on the CFRC is a high-resolution magnetic probe array. Faraday or “B-dot” loops have been the standard tool for diagnosing the field structure of low-temperature magnetized plasmas for over fifty years. Modern research on magnetic reconnection and fluctuations in magnetized plasmas still relies on inductive probes [e.g. 141, 142]. A pair of probes was designed and constructed to meet the needs of two experiments, the Swarthmore

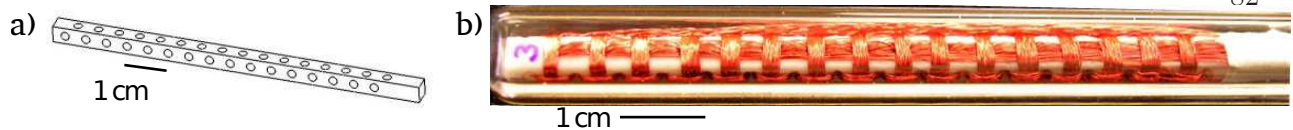


Figure 3.17: a) CAD drawing of Macor stalk showing arrangement of winding holes. b) Complete probe head.

Spheromak eXperiment (SSX) [99] and the Colorado Field-Reversed Configuration experiment (CFRC) [143]. SSX research has been focused on aspects of reconnection and relaxation, including energetic particles and flows during merging [99]. Both research programs require detailed mapping of time-varying magnetic fields with fast response and high spatial resolution.

B-dot probes operate by Faraday's law,

$$V = -\frac{d\Phi_B}{dt},$$

where a voltage V is induced around a loop due to the change in the enclosed magnetic flux, Φ_B .

In the case of a fixed coil of N turns and cross-sectional area A across which the magnetic field B is uniform, this reduces to

$$V = -NA\frac{dB_{\perp}}{dt},$$

where the subscript \perp indicates the component of the magnetic field perpendicular to the plane of the loop. The raw signal must be integrated to obtain the magnetic field as a function of time:

$$B_{\perp}(t) = -\frac{1}{NA} \int_0^t V(t') dt' \quad (3.34)$$

The probe described here has 16 spatial locations, high spatial (5mm) and time ($1\mu s$) resolution, and a simple and somewhat modular vacuum design. A drawing of the probe armature layout and a photograph of the completed probe head are shown in Figure 3.17. Hand-wound coils were chosen over commercial surface-mount inductors due to the difficulty of aligning the axes of the surface mount coils [144] and the relative ease of winding coils by hand on a simple form. Two orthogonal sets of 17 holes are drilled into a Macor ceramic stalk ($4\text{ mm} \times 4\text{ mm} \times 90\text{ mm}$) to make an armature for threading wire (Fig. 3.17a). Macor was chosen because of its high dimensional stability, machinability, and insulating properties. Two sets of coils are wound through these holes and

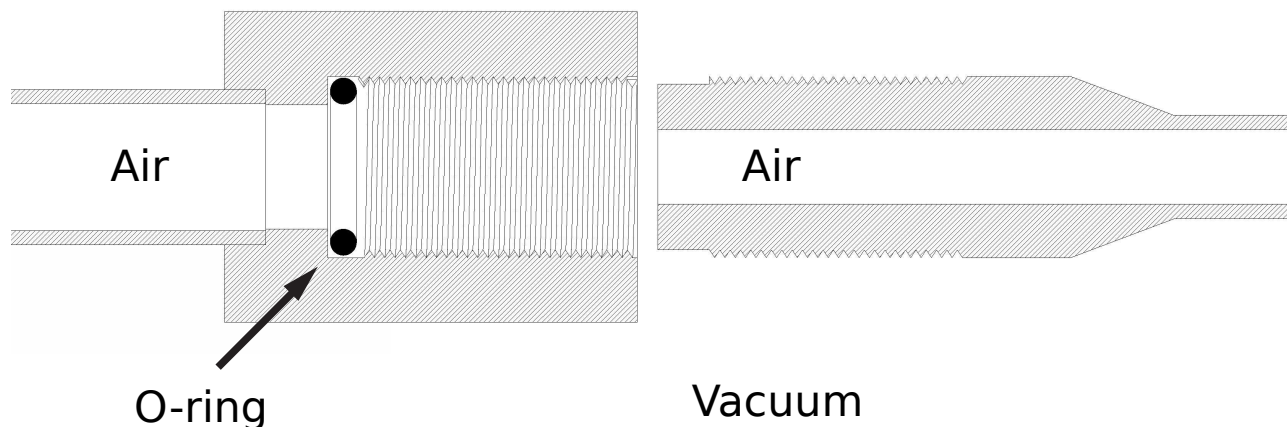


Figure 3.18: O-ring seal for connecting glass envelope to stainless tube.

the third set is wound around the square cross-section of the armature (Fig. 3.17b). The number of turns in each coil is restricted by the physical strength of the Macor. The allowable size of the armature holes given the 5 mm spacing of the coils is 2 mm. For the low-frequency measurements presented here, each coil has an area of approximately $4.5 \times 4.5 \text{ mm}^2$ and consists of 20 turns of 36 AWG magnet wire, giving a calculated response constant of $NA \sim 0.4 \text{ mVs/T}$. The true NA product for each coil was measured using a calibrated Helmholtz pair, as described below. The response time of the coil is given by its inductance combined with the 50Ω input impedance of the amplifiers. For a typical 20-turn coil $L \sim 3\mu\text{H}$, giving a maximum undistorted signal frequency of $R/2\pi L = 2.6 \text{ MHz}$. The self-resonant frequency of each coil is approximately 140 MHz.

The Macor probe stalk is protected from the plasma by a quartz envelope, which is attached to a 304 stainless steel (304ss) shaft by way of a threaded vacuum seal. The interior of the probe is at atmospheric pressure, which eliminates the need for an expensive and bulky multi-pin vacuum feedthrough. The quartz is brazed to 304ss tubing. A threaded adapter was machined and welded on to the existing tubing, while a mating adaptor was welded to the probe shaft. The adapter forms a vacuum seal by compressing an o-ring against two flats as shown in Fig. 3.18. This setup allows simplicity and facilitates repair or exchange of the probe stalk. The stainless shaft enters the vacuum vessel through a commercial double-o-ring “Wilson” seal (MDC part # 672008). Each pair

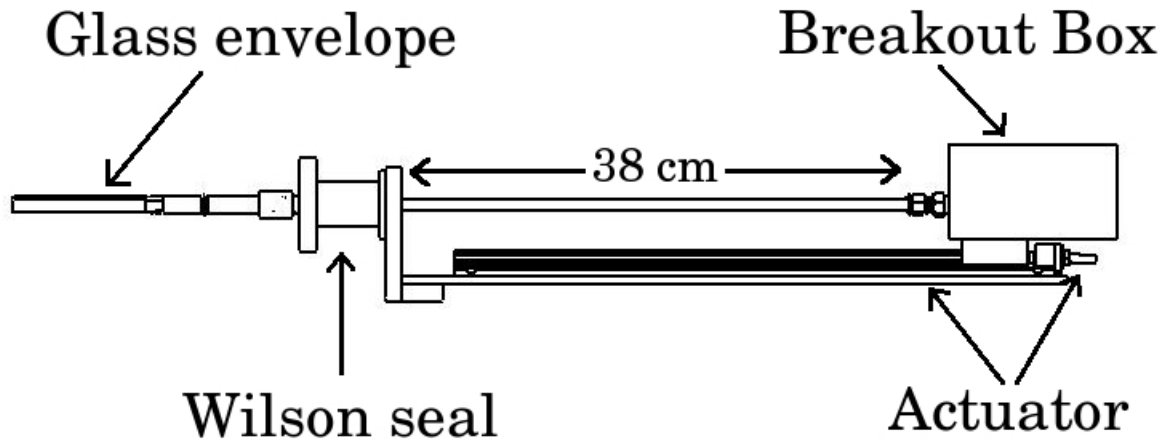
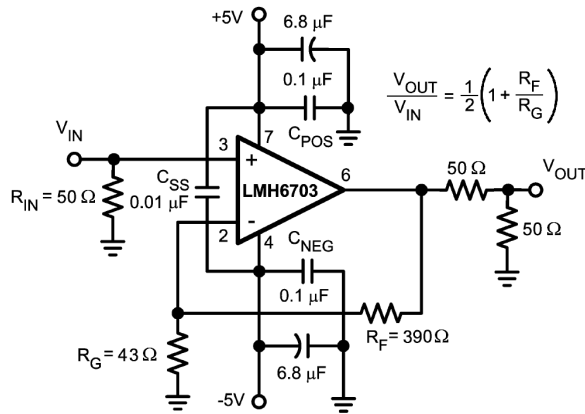


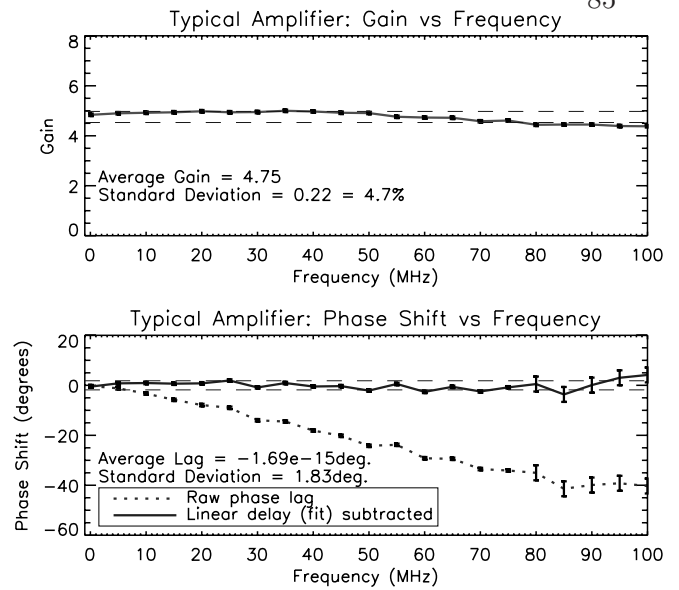
Figure 3.19: Diagram of aluminum support structure and linear actuator.

of coil leads is connected via a printed circuit board (PCB) terminal to an SMA plug inside a cast aluminum breakout box on the air side of the steel shaft. This arrangement provides strain relief and conversion from the twisted-pair coil leads to coaxial lines for shielded data transmission. Using PCB terminals allows for compact, low-inductance connections. The breakout box is mounted to the bushing of a screw-driven linear actuator (Kerk Motion RGS6010T \times 18") to enable translation of the entire probe stalk. The assembly is supported by an aluminum frame bolted to the air side of the Wilson seal (Fig. 3.19).

To enable measurement of low-level fluctuations, the probe system includes removable (inline) active differential amplifiers with a gain of 5. The circuit diagram for a single amplifier is shown in Fig. 3.20. Traces for a low-pass output filter are printed on the circuit boards. A filter with cutoff frequency $f_c = 20$ MHz is included in the CFRC amplifiers to prevent aliasing above the data acquisition Nyquist frequency. The LMH6703 was chosen as the active element because of its flat frequency response up to 100 MHz (maximum SSX data acquisition Nyquist frequency). The amplifiers were designed with high bandwidth so that fast fluctuations could be measured (using low inductance windings). The 48 amplifiers are mounted inside a 0.25"-thick cast aluminum box to shield them from electromagnetic noise generated by the discharge pulsed power. The inputs and outputs are coupled to the outside of the box via SMA bulkhead connectors. The ambient noise



a)



b)

Figure 3.20: a) Fast amplifier circuit diagram. The theoretical gain is approximately five with a bandwidth of 100 MHz. b) Gain and phase lag versus frequency for a typical amplifier.

level on the output of the amplifiers is < 1.5 mV. Crosstalk between amplifier channels is $\leq 0.5\%$ of the input signal voltage. Hardware integration is not built in to the amplifier system. For our experiment, raw b-dot data is recorded and integrated numerically so that fluctuation details are not compressed into a small portion of the digitizer dynamic range by the presence of a background magnetic field.

The gain and phase delay for each fast amplifier were measured as a function of frequency using an RF generator and a digital storage oscilloscope. The SSX amplifiers were calibrated up to 100 MHz, while the CFRC amplifiers were tested up to 20 MHz (low-pass cutoff frequency). The average gain for 48 SSX amplifiers is $4.8 \pm 0.2(4\%)$ and the average phase lag (neglecting the $\sim 0.2\mu\text{s}$ constant time delay in the test circuit) is $0.0^\circ \pm 0.7^\circ$. The CFRC average gain and phase lag, respectively are $4.8 \pm 0.1(2\%)$ and $0.0^\circ \pm 0.5^\circ$. Calibration data for a typical amplifier is shown in Fig. 3.20b. Each pickup loop is calibrated over the appropriate frequency range using a sinusoidally-driven, low-inductance Helmholtz coil with external series resistance ($R_s \sim 100 \Omega$) added to stabilize the coil current. The voltage across the current-limiting resistor is measured

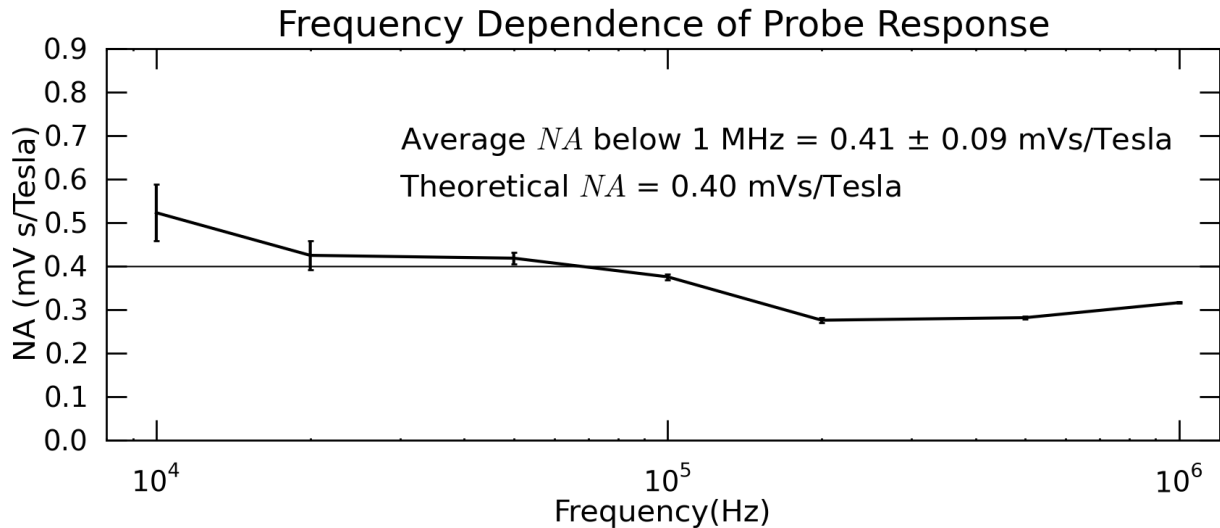


Figure 3.21: Calibration data for a single $3\mu H$ coil.

simultaneously with the output voltage of the probe coil. The calibration constant is determined by dividing the output voltage by the product ωB , where B is determined from the coil current and the Helmholtz coil constant. A sample calibration curve is shown in Fig. 3.21.

Original design specifications included a requirement that the configuration of the probe be able to change for measuring propagation of fluctuations along an arbitrary axis. Due to cost and time constraints, this capability was not implemented. All measurements to date have been recorded with the probe channels aligned along the radius of the vacuum chamber. Nevertheless, we have observed waves propagating along the probe axis, especially during merging. If primary reconnection plane is at the midplane of the device, the radial coordinate of the chamber corresponds to the poloidal direction of the merging spheromaks. Examples of magnetic measurements and spectral analysis are described in Sections 3.3.4 and 3.4.

Status notes:

The only data recorded on CFRC so far uses high-gain, twenty-turn coils. These measurements are restricted to low frequency wave observations because $R/2\pi L = 2.6$ MHz.

The original breakout PCBs had a single ground for all 8 channels, which created many ground loops. The PCBs were redesigned with separate grounds, and replaced in both the CFRC

and the SSX probes. Cable connections need to be isolated from one another for the same reason, and are currently wrapped in kapton tape. A comparison of the data before and after isolating the channels grounds is shown in Figure 3.22. When compared with the discharge current waveform (Fig. 3.26), it is clear that the magnetic signals were dominated by induced voltages from the gun discharge. This means that data taken before August 6, 2010 is not useful for measurements of field structure on the discharge time scale. Higher frequency fluctuation data may still reflect local plasma behavior.

The probe was designed without capacitive signal rejection. In a single-ended measurement scheme, fluctuations in the local plasma potential can drive non-negligible currents in the coils. Many schemes are available to mitigate such electrostatic pickup [145], but the issue was not considered during the original design. We assume that magnetic fluctuations are dominant for our case, but nonetheless, the possibility of electrostatic signals mixing with the magnetic signals should be kept in mind.

In addition, there is no hardware low-pass filter in place in the current setup. Because the gain of the low-frequency coils is so large, the amplifiers (with integrated low-pass filter) are not in use³. Therefore, it is possible that fluctuations with frequencies larger than 20 MHz contribute to lower frequency components via aliasing.

3.3.3.5 Simple Magnetic Probe

Although funding opportunities made it a priority to construct the multi-channel magnetic array before attempting more global measurements, a single point magnetic probe was constructed “on-the-cheap” to provide field measurements at a second spatial point. Similar in principle to the above multi-probe, this diagnostic provides of just one triplet of magnetic measurements. Glass tubing was melted closed at one end to provide a suitable vacuum envelope. The envelope is connected to 304ss tubing using Swagelok[®] fittings. Electrostatic coupling was assumed to be

³ The low-frequency/high-gain coils were also too sensitive for SSX. Tim Gray reduced them to single-turn coils, and there was still some saturation of the digitizer (without amplifiers).

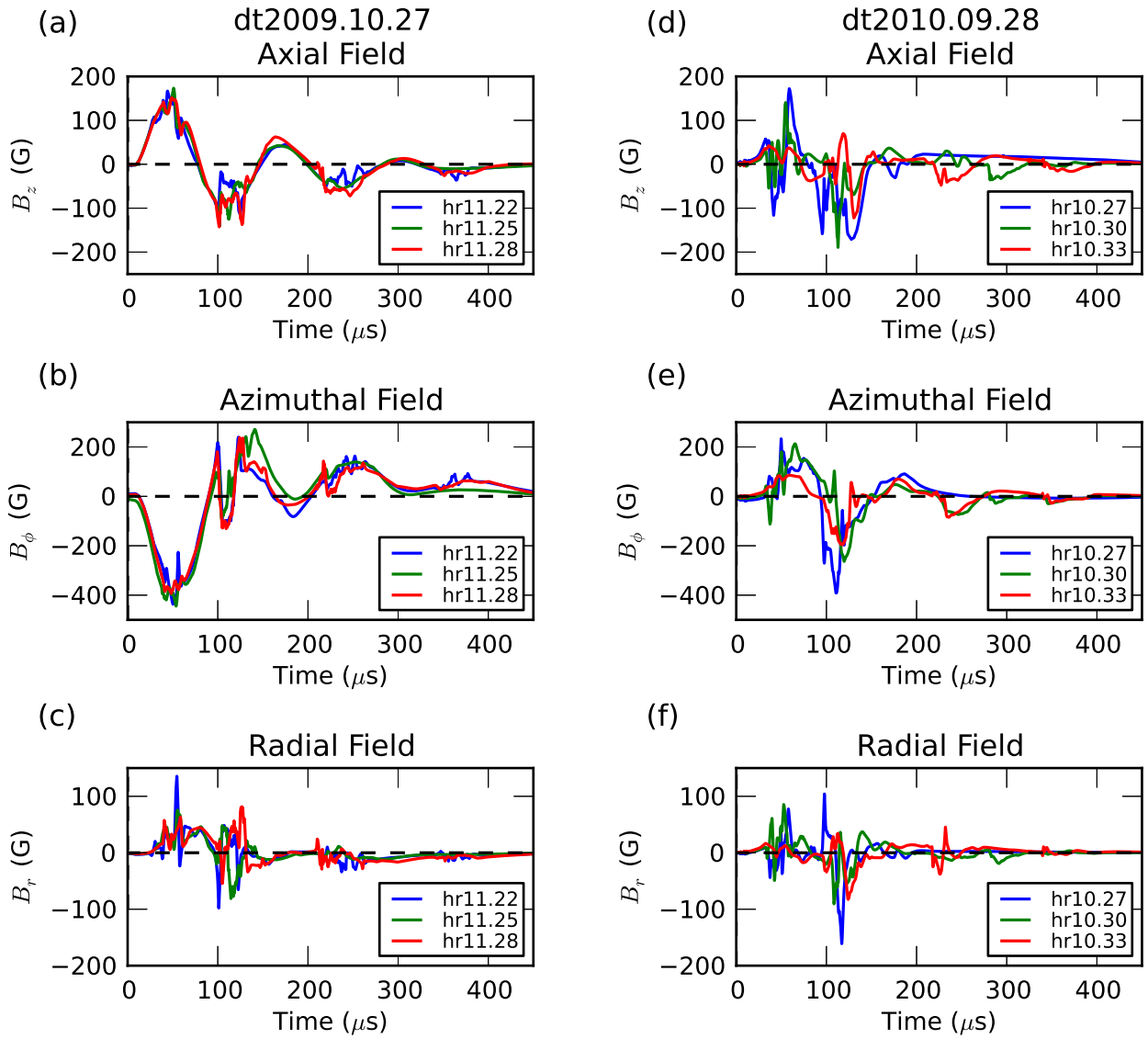


Figure 3.22: Comparison of magnetic field traces for a single triplet of coils at $r = 27$ cm (a)-(c) before and (d)-(f) after isolating the channel grounds from each other. The signals in the first column are dominated by pickup from the discharge current (cf. Fig. 3.26).

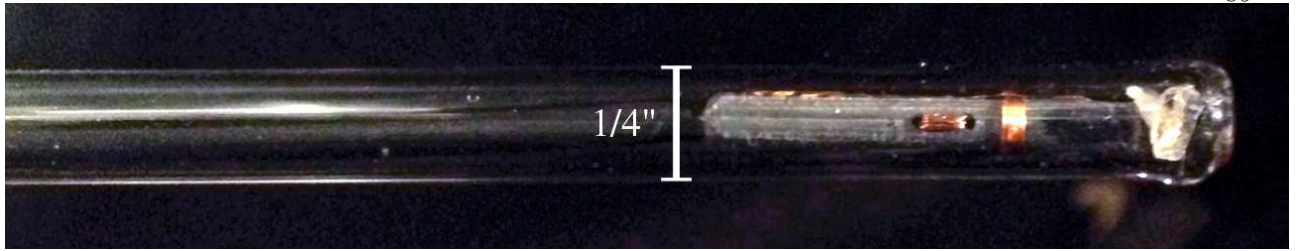


Figure 3.23: Photograph of single B-dot probe installed in machine.

negligible for simplicity and quick construction. Each coil consists of 8 turns of AWG 36 wound on a square PVC form $1/8''$ on a side, and the signal wires run the length of the probe tube as twisted pairs before being connected to RG-58 coaxial cables for transmission to the digitizer. A photograph of the probe is shown in Figure 3.23. The single bdot channels were calibrated in the same way as the channels for the multi-probe. The average measured NA value for these coils is $79 \pm 9 \mu\text{Vs}/\text{T}$, compared to a theoretical value of $80 \mu\text{Vs}/\text{T}$. A calibration curve versus frequency is shown in Figure 3.24.

3.3.4 CFRC Plasma Properties and Machine Status

As a new experiment, the CFRC was still in development and shakedown when it was put on hold due to lack of funding. This section describes the status of the machine at the time it was shut down, and the properties of the plasma it produced.

CFRC was designed to allow flexible configurations for the electrode and magnet polarities. A summary of the available merging configurations is shown in Figure 3.25. Each diagram indicates the poloidal (in-plane) and toroidal (out-of-plane) fields expected in the final configuration. The cases that do not correspond to a spheromak or FRC show the fields of the two spheromaks before merging. To date, the machine has been operated successfully in only configurations 1 and 2. We have been unable to fire the guns reliably with the center electrode negative. Much higher voltage is required for breakdown than with positive center electrodes, and the discharge is intermittent. Attempts to fire the guns in negative polarity often produced arcing outside the machine and damaged several components. At low negative voltages, a glow-like discharge sometimes formed,

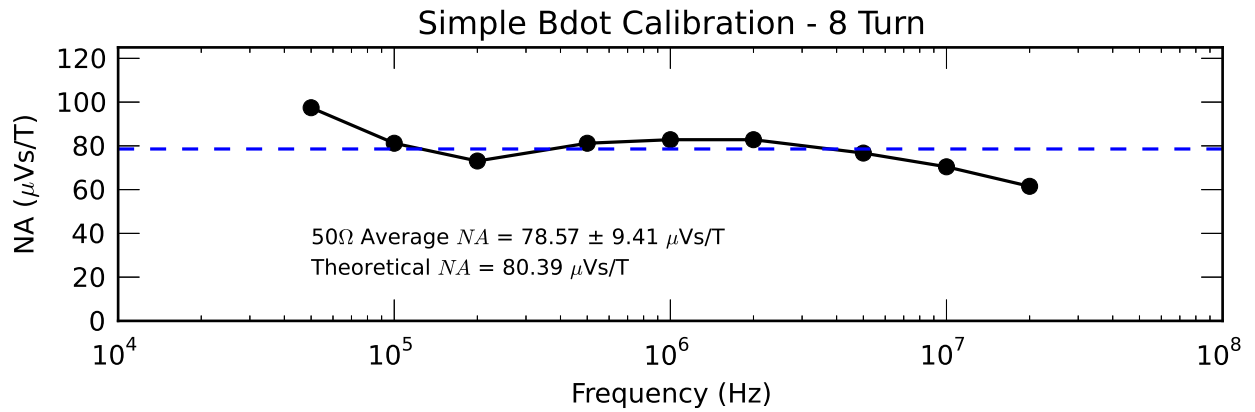


Figure 3.24: Calibration data for a single 8-turn coil.

persisting for large fractions of a second. Addition of free electrons via a hot filament did not improve success, nor did an attempt to increase the residence time of electrons in the gun gap by using permanent magnets. A high-current-density lanthanum-hexaboride cathode was acquired to flood the gun with electrons, but was never tested. Our inability to operate the guns with negative center electrodes is puzzling because other coaxial-gun devices operate **only** in negative polarity [131, 146]. In addition, the current during a discharge with a positive center electrode oscillates (see Fig. 3.26b), so that we know plasma can be sustained with current in the opposite direction. We believe our difficulties with negative polarity discharges are related to the initial breakdown, but the problem remains unsolved.

Plasma objects studied to date have been produced using configuration 2. We have attempted to form both spheromaks (using only one gun) and FRCs (using both). Typical waveforms for the stuffing magnet current and the gun discharge current, acquired using the Rogowski coils described in Section 3.3.2, are shown in Figure 3.26. The gun current rings at ~ 8 kHz. The stuffing flux is approximately constant during the plasma discharge.

The discharge is quite variable at all tested parameters. As an example, interferometer data is shown in Figure 3.27 for seven consecutive shots with identical settings. These discharges use both guns, and in principle should form FRCs. The signal behavior seems to be consistent during the first $50 \mu\text{s}$ of the shot, and then becomes subject to large shot-to-shot variations. The shape,

Looking @ Machine From the North

Magnetic Config	W Gun + W Mag +	W Gun + W Mag -	W Gun - W Mag +	W Gun - W Mag -
E Gun + E Mag +	1 X 	2 FRC 	3 X 	4 Spheromak
E Gun + E Mag -	5 FRC 	6 X 	7 Spheromak 	8 X
E Gun - E Mag +	9 X 	10 Spheromak 	11 X 	12 FRC
E Gun - E Mag -	13 Spheromak 	14 X 	15 FRC 	16 X

Figure 3.25: Matrix of possible merging arrangements for CFRC. Each diagram indicates poloidal (in-plane) and toroidal (out-of-plane) fields. Only the final object is indicated for cases where merging is expected.

timing, and amplitude of the signals are all somewhat variable. Some shots even lack the sharp peak we identified with a merged structure (consistently absent from single-gun shots), resulting in a peak amplitude disparity of more than a factor of four. When this peak is present, the time at which it occurs can vary by as much as $50 \mu\text{s}$.

Given this large variation in a quantity somewhat insensitive to local values (line-integrated), it is not surprising that local measurements from single-point probes are also variable. Figure 3.28 shows the magnetic field evolution for a set of consecutive shots for a single-gun discharge at similar

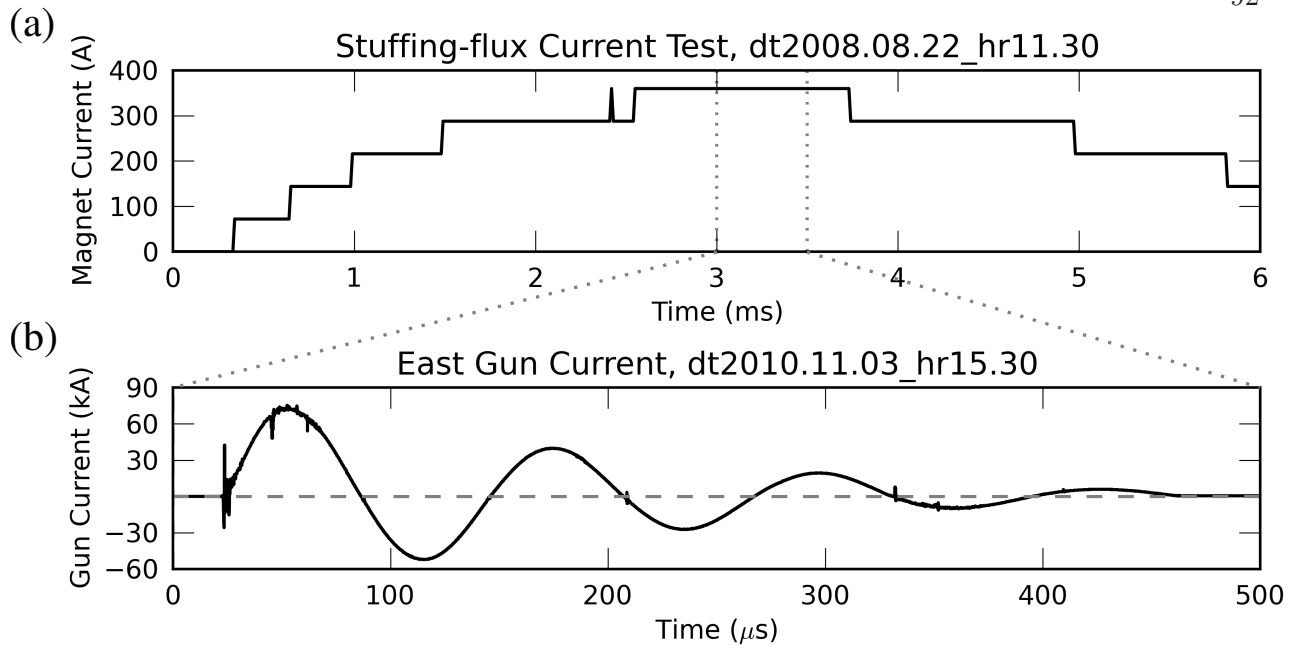


Figure 3.26: Typical waveforms of the current (a) for the stuffing flux magnet and (b) for the gun discharge. The stuffing flux is approximately constant on the timescale of the gun. The stuffing flux current appears quantized because the amplitude of the signal is only ~ 10 digitizer bits peak-to-peak (Rogowski coils designed for the high current in the guns).

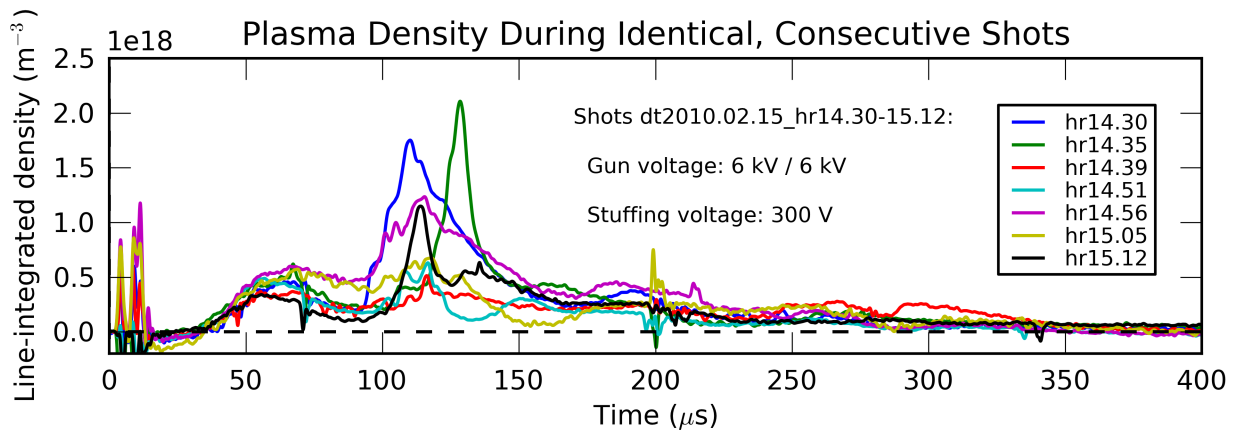


Figure 3.27: Most recent interferometer traces, demonstrating shot-to-shot variation in line-integrated density during seven identical, consecutive shots.

parameters. Although the general timing of events has some consistency, and shape of the individual traces is quite variable. Some shots demonstrate consistently-shaped traces with variable timing, while others are only vaguely similar.

Single Gun at 6kV, dt2010.09.28

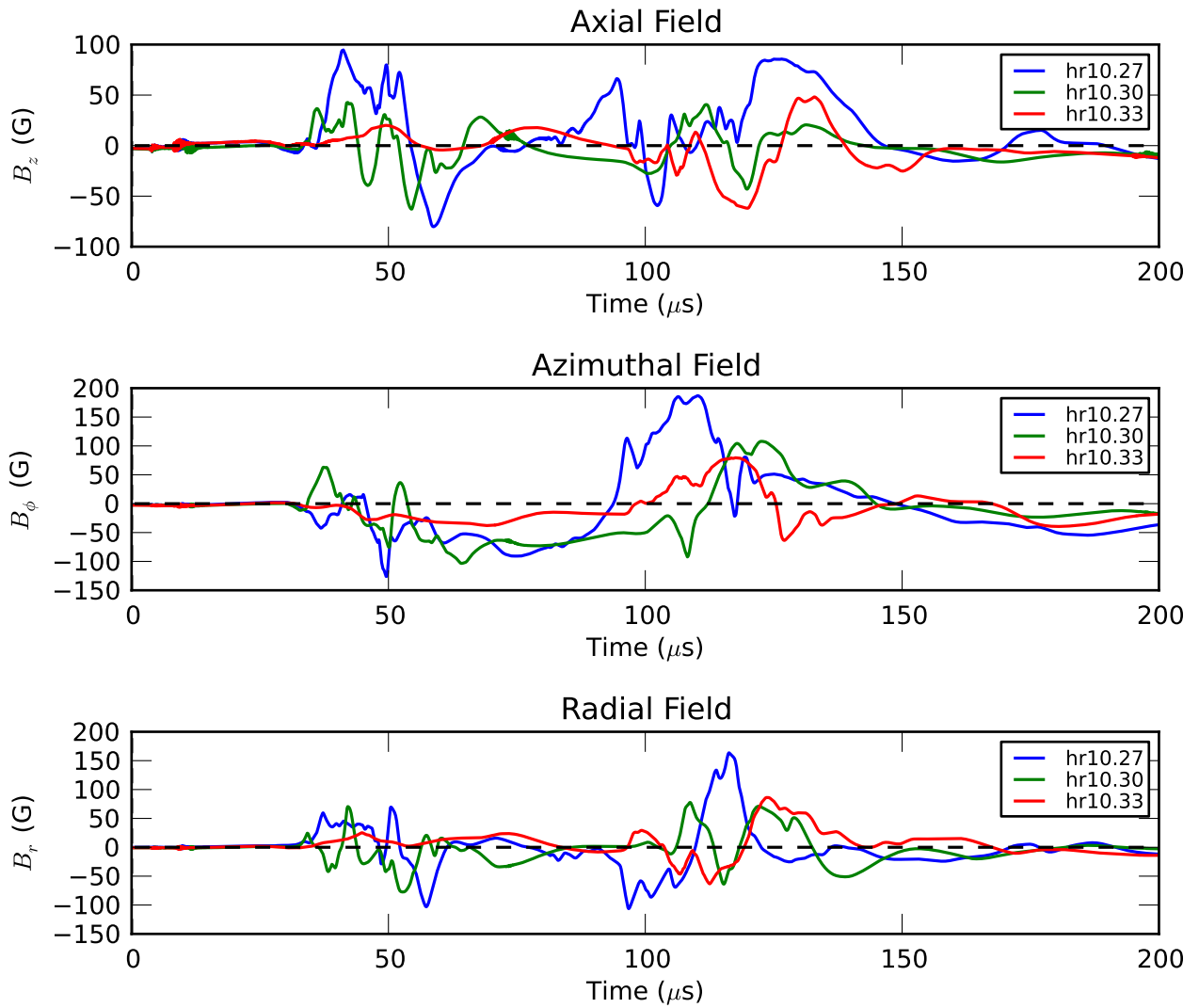


Figure 3.28: Magnetic field traces for one channel of the 48-channel probe array located at $r = 23.4 \text{ cm} = 0.6r_w$ in the midplane. Three consecutive shots at the same parameters are shown and field components are labeled in cylindrical (chamber) geometry.

Plasma objects are being launched from the guns, as evidenced by correlations between the simple b-dot probe and the 48-channel probe. Figure 3.29 shows the time-lag correlation function between the toroidal field component measured by each probe, measured at the same radius during a single-gun discharge. The simple b-dot probe is located 32 cm in front of the east gun ($z = -45.5 \text{ cm}$), while the 48-channel probe is located 77.9 cm in front of the gun at the

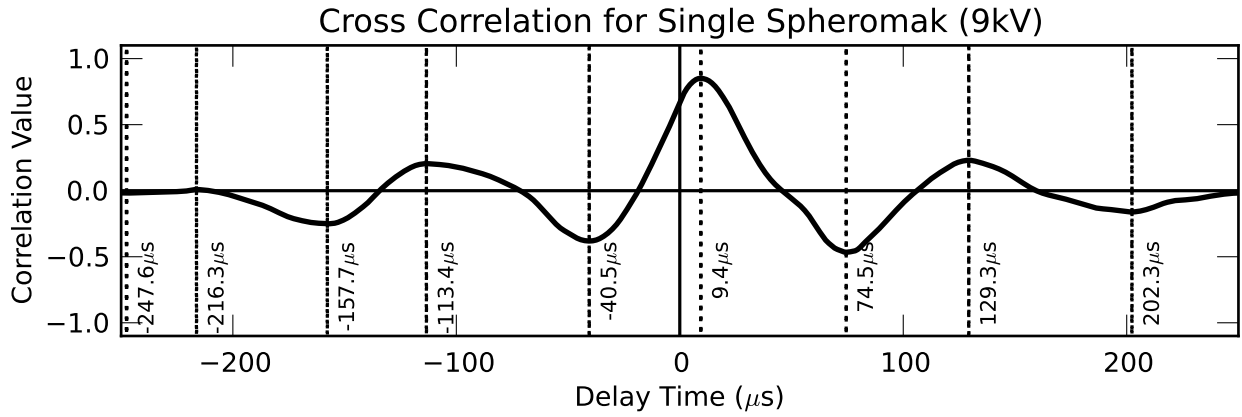


Figure 3.29: Time-lag correlation function for toroidal field measurements separated by 45.5 cm. Positive delay indicates that the probe farther from the gun receives the signal later in time.

midplane ($z = 0$). Given the spacing between them, the object measured in this discharge was moving at $v_z \approx 48$ km/s. This velocity corresponds to a propagation time of $16.2 \mu\text{s}$ between the gun and the midplane. For reference, the Alfvén transit time to the midplane estimated using the line-averaged density and measured magnetic field values is on the order of $\tau_A = r_w/v_A \sim 1 - 10 \mu\text{s}$.

Calculating the time history of the gun eigenvalue gives some indication that the Taylor formation paradigm applies. Figure 3.30 shows the calculated value of $\lambda(t) = \mu_0 I_{\text{gun}}(t)/\Phi_{\text{gun}}$, assuming that all of the flux generated by the stuffing magnet links the two electrodes. The dashed horizontal line represents the threshold gun value, $\lambda_c = 20.1 \text{ m}^{-1}$, calculated in Section 3.3.1. The dotted horizontal line represents the threshold value calculated for the chamber outside the gun, $\lambda_w = 10.2 \text{ m}^{-1}$. Dashed and dotted vertical lines indicate where $\lambda(t)$ exceeds each threshold as it increases in time. The time axis of the density (b) is shifted by the propagation time calculated above, so that increases in density may be tentatively identified with a λ value at the time of launch. There is a reasonable match between the identified threshold crossings and increases in the line-integrated density. It is interesting to note that the sharpest jump in density occurs without $\lambda(t)$ exceeding λ_c . Other experiments have found a formation threshold that is independent of the dimensions of the chamber or flux-conserver outside the gun [125] (depending only on λ_c). In our case, not all of the stuffing flux intercepts the electrodes (see Section 3.3.1), so that the calculation

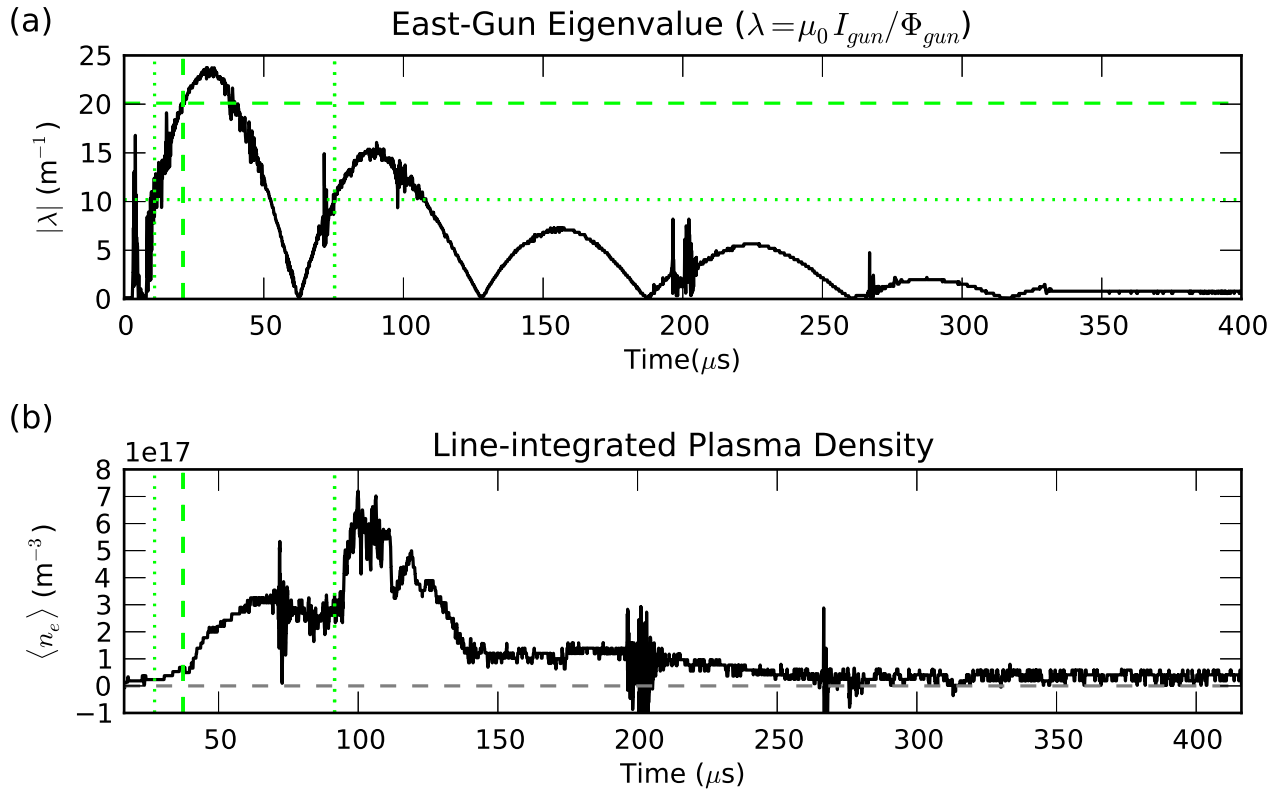


Figure 3.30: Comparison of spheromak launch threshold with plasma density. (a) Calculated spheromak eigenvalue, $\lambda(t)$. The dashed horizontal line represents the threshold gun value, $\lambda_c = 20.1 \text{ m}^{-1}$, calculated in Section 3.3.1. The dotted horizontal line represents the threshold value calculated for the chamber outside the gun, $\lambda_w = 10.2 \text{ m}^{-1}$. Dashed and dotted vertical lines indicate where $\lambda(t)$ exceeds each threshold as it increases in time. (b) Line-integrated density, shifted by the propagation time calculated from Figure 3.29. Density increases seem to coincide with eigenvalue threshold crossings.

of $\lambda(t)$ shown in Fig. 3.30(a) is likely an underestimate of the true value (perhaps even by a factor of two).

Another complication arises because the discharge oscillates. If indeed, multiple spheromaks are launched during a single shot, we are essentially performing counterhelicity merging experiments whether we use one gun or both. Since the sense of the toroidal field of the spheromak is determined by the sign of the discharge current, contiguous peaks in the lambda trace represent alternating helicity spheromaks. Thus the first rise in density in Figure 3.30b may correspond to a spheromak, while the second may correspond to a distinct, merged object. Even before λ crosses the launch

threshold a second time, the gun may be injecting (counter) helicity into the chamber, so that it may not be strictly correct to describe the first object observed as a standard spheromak.

Additional insight can be gleaned by observing the magnetic field evolution for a single-gun discharge. Because of the lack of overlap in diagnostic measurements (see Status Notes below), we are unable to analyze a simultaneous density trace. Figure 3.31 shows a zoomed-in view of the first λ_c crossing, with accompanying traces for the magnetic field components in the midplane at $r = 27.4 \text{ cm} = 0.73r_w$. For reference, the radial position of the magnetic null for an ideal spheromak, disconnected from the gun and in the lowest Taylor state, is $r_0 = 0.63r_w = 23.5 \text{ cm}$. Dashed and dotted lines are as in Figure 3.30, and the time axis of the magnetic field components is again shifted to take into account the measured propagation time for magnetic structures to reach the midplane. Several features are notable:

- (1) After the initial dynamic phase ($\sim 35 - 50 \mu\text{s}$), the toroidal field settles into a quasi-steady value.
- (2) The axial field assumes a value of one sign during the dynamic phase, then **reverses**.
- (3) The radial field remains small, with departures from zero occurring simultaneously with changes in the other components.

This data is potentially consistent with the formation of a ‘flipped’ spheromak [93], but more global diagnostics are required to identify the object’s magnetic structure. Further evolution is more complicated, due to the possibility of multiple launches. The full traces corresponding to Fig. 3.31 are shown in Figure 3.32. An abrupt change in the field structure near $t = 95 \mu\text{s}$ indicates that a second object has detached from the gun and displaced or merged with the first object.

Due to the small extent of the magnetic probe (optimized for localized wave measurements), there is limited information about the radial structure of the fields. Figure 3.33 shows a projection of \mathbf{B} for the same shot in the r - z plane as a function of time for all 16 positions of the 48-channel magnetic probe. The abrupt reversal of both components is suggestive of the ‘flipping’ of the spheromak that occurs when λ becomes large enough that open field lines are excluded from the

Single-Gun Magnetic Field Evolution,
dt2010.09.28_hr10.27 6kV/300V, $r = 27.4\text{cm}$

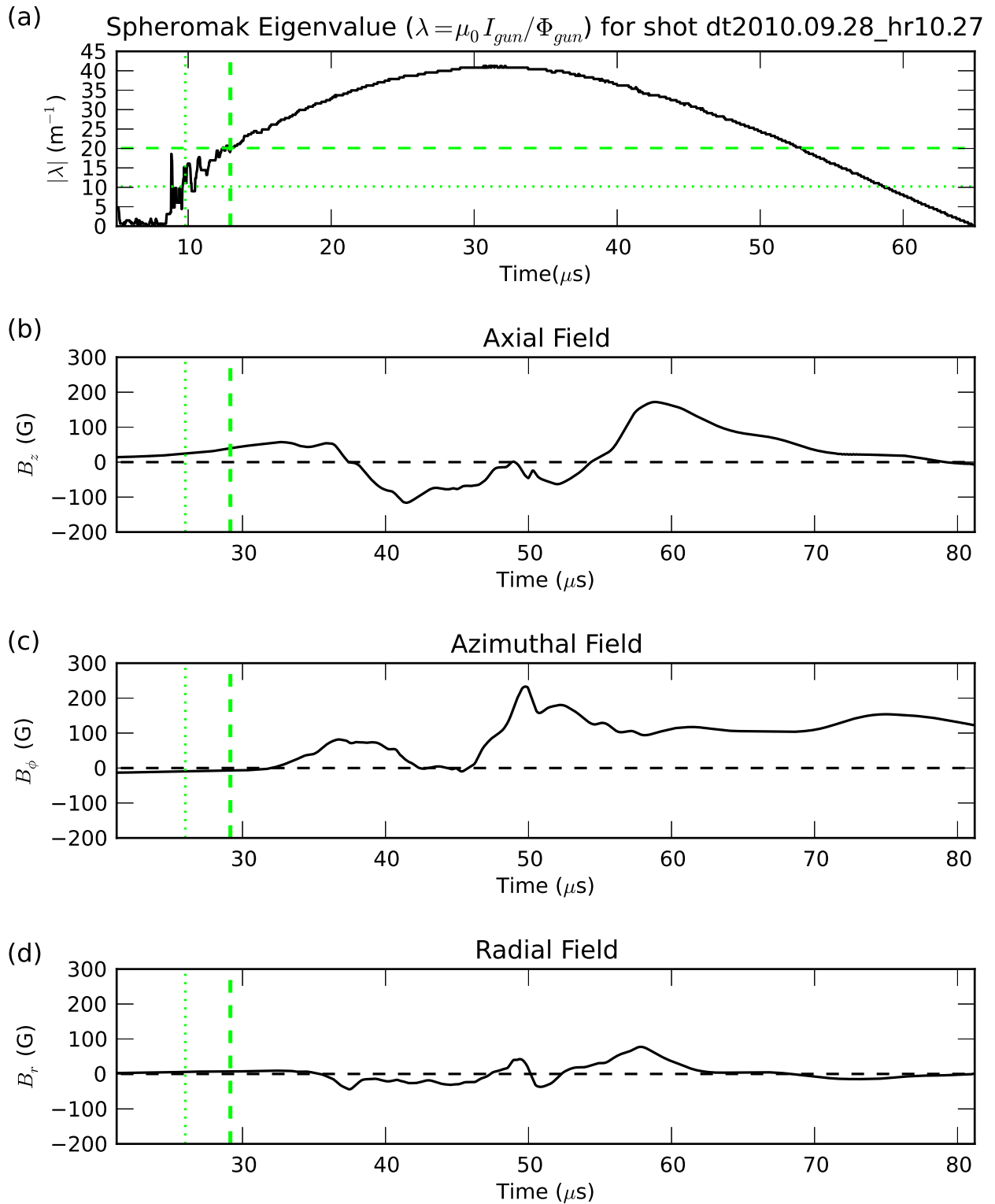


Figure 3.31: Magnetic traces in the midplane for $r = 27.4\text{cm}$. Data may be consistent with formation of a flipped spheromak equilibrium.

Single-Gun Magnetic Field Evolution,
dt2010.09.28_hr10.27 6kV/300V, $r = 27.4\text{cm}$

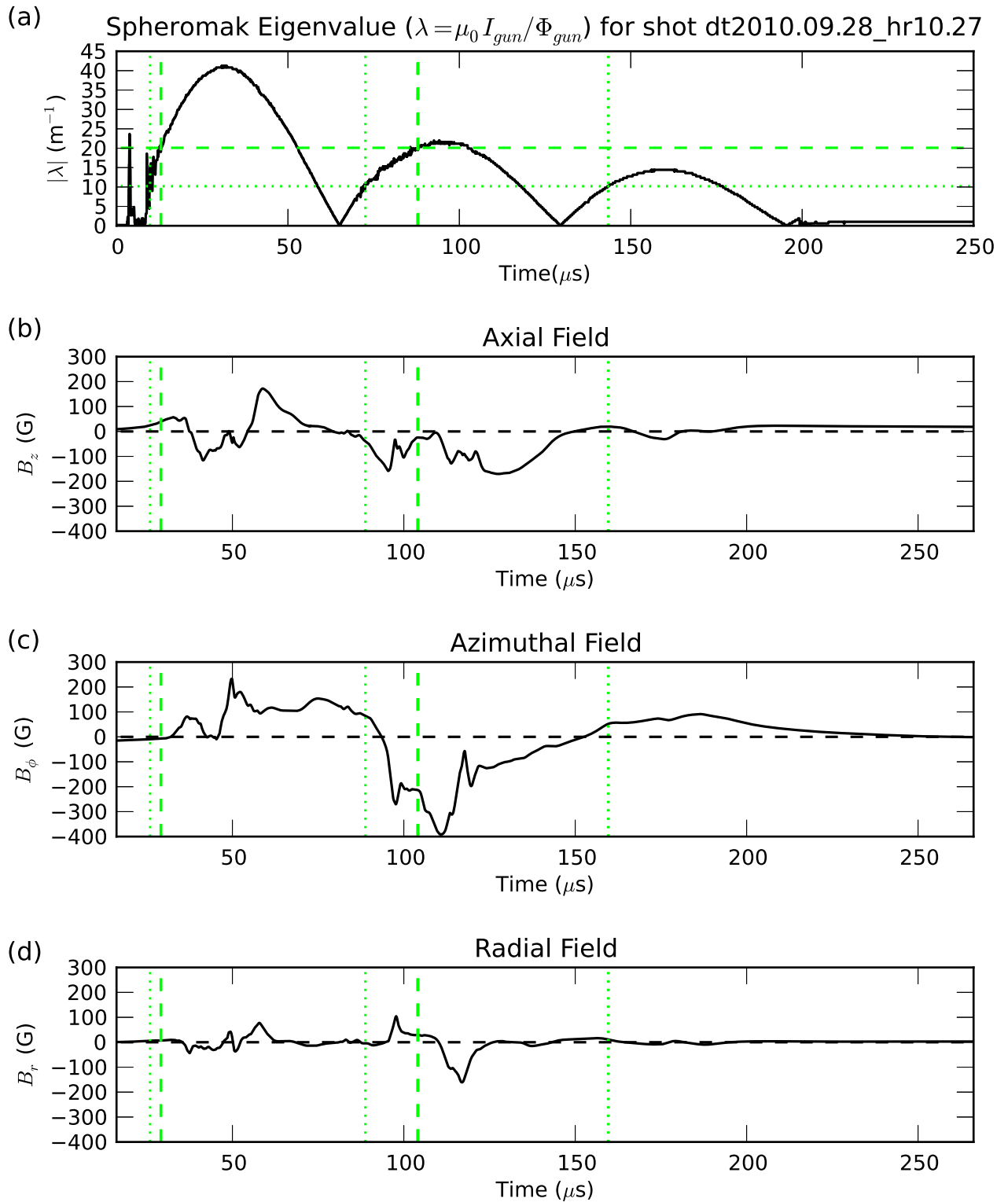


Figure 3.32: Magnetic traces in the midplane for $r = 27.4\text{ cm}$. The abrupt change in the azimuthal field direction near $t = 95\ \mu\text{s}$ may indicate the formation of a second spheromak.

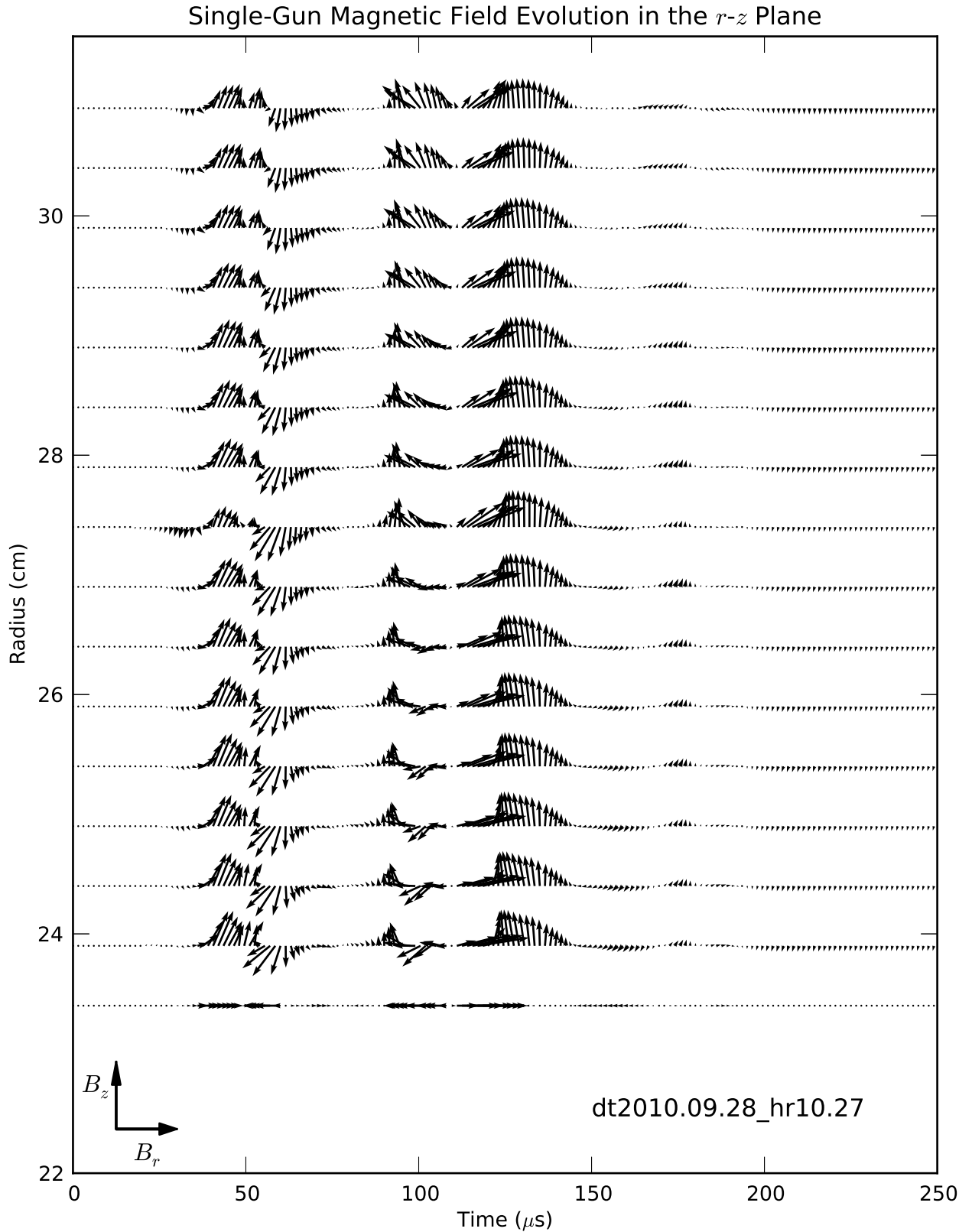


Figure 3.33: Projection of magnetic field in the r - z plane as a function of time and radius. The abrupt flip of both components near $t = 50 \mu\text{s}$ is present along the length of the probe. The axial field is not observed to reverse as a function of position, suggesting that the probe does not cross the magnetic axis.

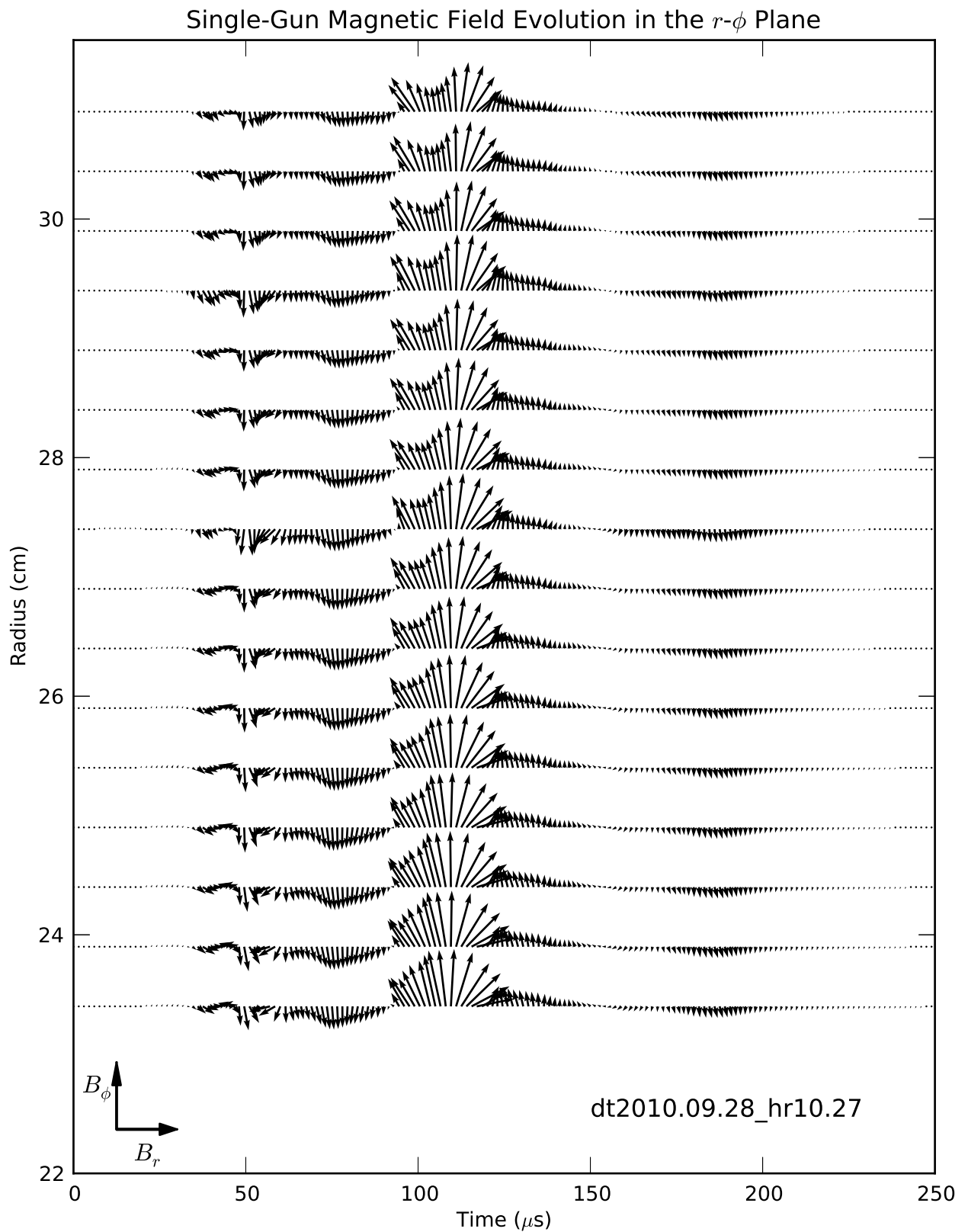


Figure 3.34: Projection of magnetic field in the r - ϕ plane as a function of time and radius. The field evolution appears nearly uniform over the measured radii.

center of the torus [93, 147]. The evolution of the field is relatively uniform along the probe, suggesting that the magnetic axis is not close to the measured radii. The toroidal field evolution also appears nearly uniform in radius. A projection of the field evolution in the r - ϕ plane is shown in Figure 3.34. The approximate uniformity of the time evolution on the spatial scale of the probe indicates that the magnetic probe is essentially a point measurement and cannot recover single-shot information about the global structure.

The above interpretation relies on the assumption that a spheromak-like object is forming. It is possible that the objects being formed are not volume-filling. Given that our gas injection is highly asymmetric, each gun may launch a pair of flux ropes, one forming near each gas inlet. Formation of distinct flux ropes has been observed [98], and in fact engineered [148] in the CalTech spheromak experiment.

The situation is similar during merged operation (firing both guns), although there is a marked density increase in most shots that we do not see during single-gun discharges. Figure 3.35 shows this behavior along with the concurrent λ value for one gun. The single shot magnetic data most easily interpreted in the FRC-merging model is shown in Figure 3.36, along with the λ traces for both guns. Again, there is no simultaneous density measurement. It is possible that the behavior of the magnetic field direction near $t = 150 \mu\text{s}$ indicates the formation of an FRC-like object. The azimuthal field decays as the axial field increases. This corresponds to a decay in the toroidal field of a (non-tilted) spheromak in the chamber and an increase the poloidal field of a (non-tilted) FRC. For completeness, plots of the spatio-temporal projections of \mathbf{B} (as above) are shown in Figures 3.37 and 3.38.

Unfortunately, there are no other magnetic measurements for this shot, so we cannot rule out a simple tilting of the structure. Both explanations seem somewhat unlikely, since the dynamics are slow (tens of estimated Alfvén times). Single-point measurements are simply insufficient to identify the objects created in CFRC.

Although we cannot describe the plasma objects created during two-gun operation in a global way, we can infer that these objects are distinct from the single-gun plasmas. Figure 3.39 shows the

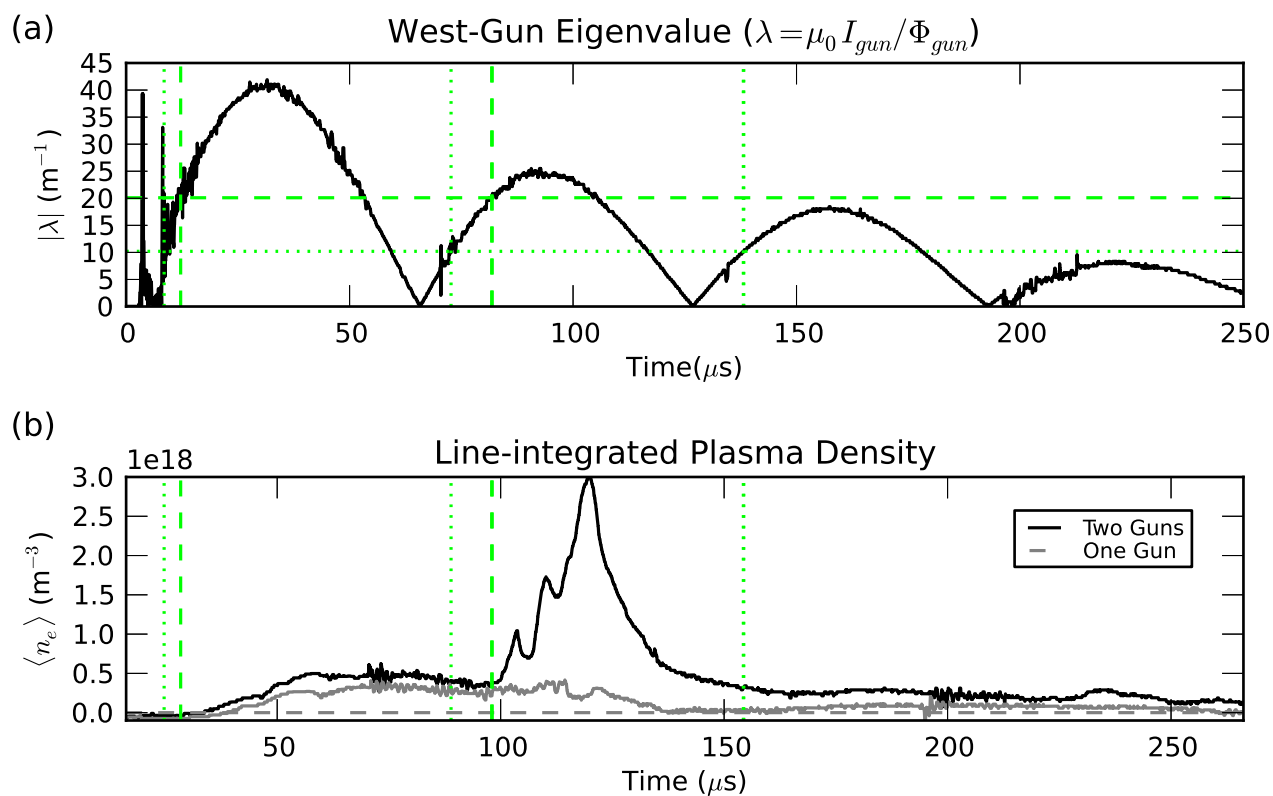


Figure 3.35: Evolution of line-average density for two-gun discharge (merged). (a) Time evolution of λ for west gun. (b) Time evolution of line-integrated plasma density. A trace for a single-gun discharge using the same gun parameters is shown for contrast in light gray. Merged timestamp = 'dt2009.10.27_hr14.18', single-gun timestamp = 'dt2009.10.27_hr11.22'.

Two-Gun Magnetic Field Evolution,
dt2010.10.05_hr11.49 4kV/4kV/300V, $r = 27.4\text{cm}$

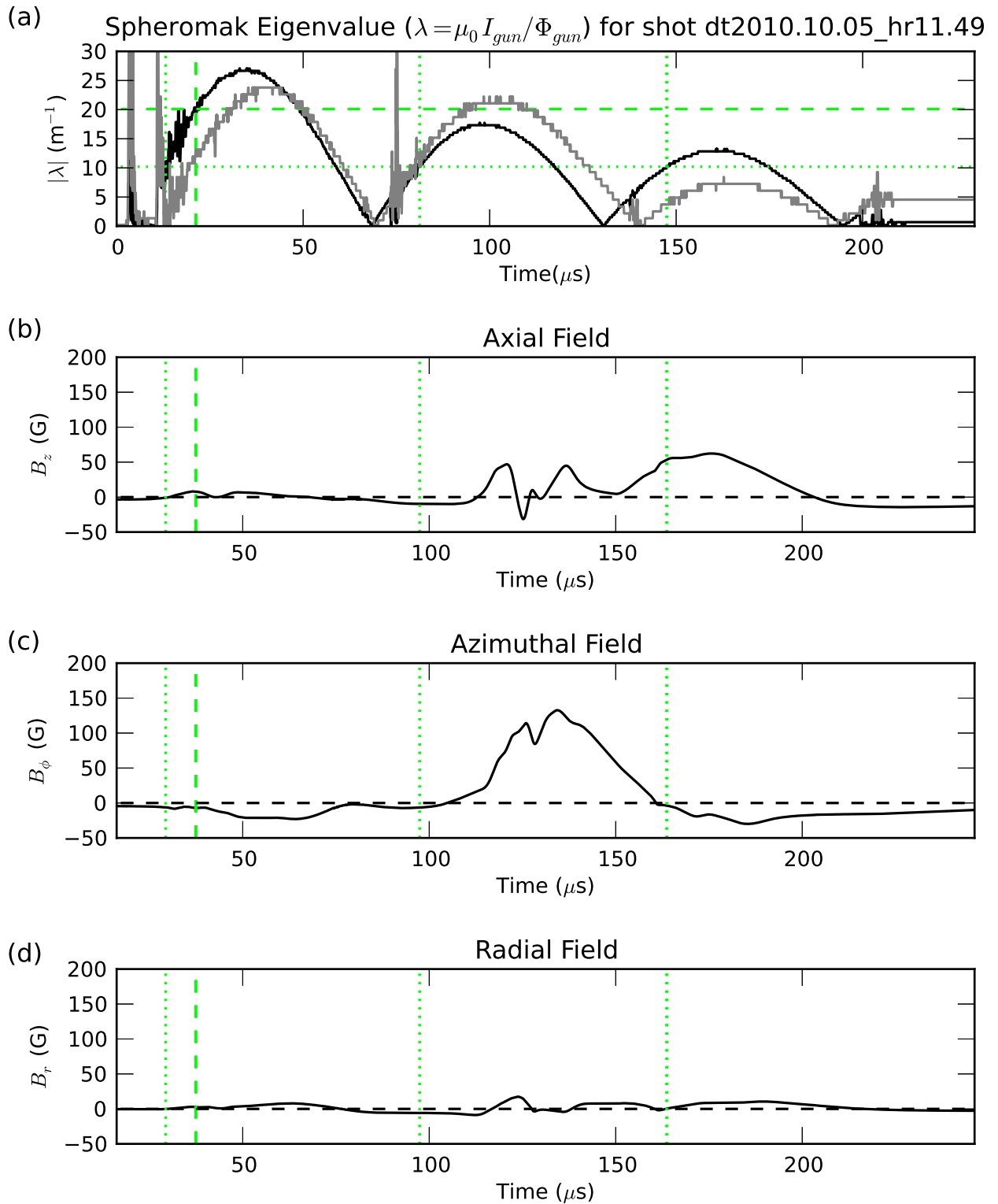


Figure 3.36: Magnetic traces in the midplane for $r = 27.4\text{cm}$. The lighter (grey) trace in (a) shows the λ value for the second gun. In the time period shortly after $t = 150\mu\text{s}$ axial field (b) increases while the azimuthal field (c) decays, indicating a possible FRC-like object with zero toroidal (azimuthal field) but finite poloidal (radial/axial) field.

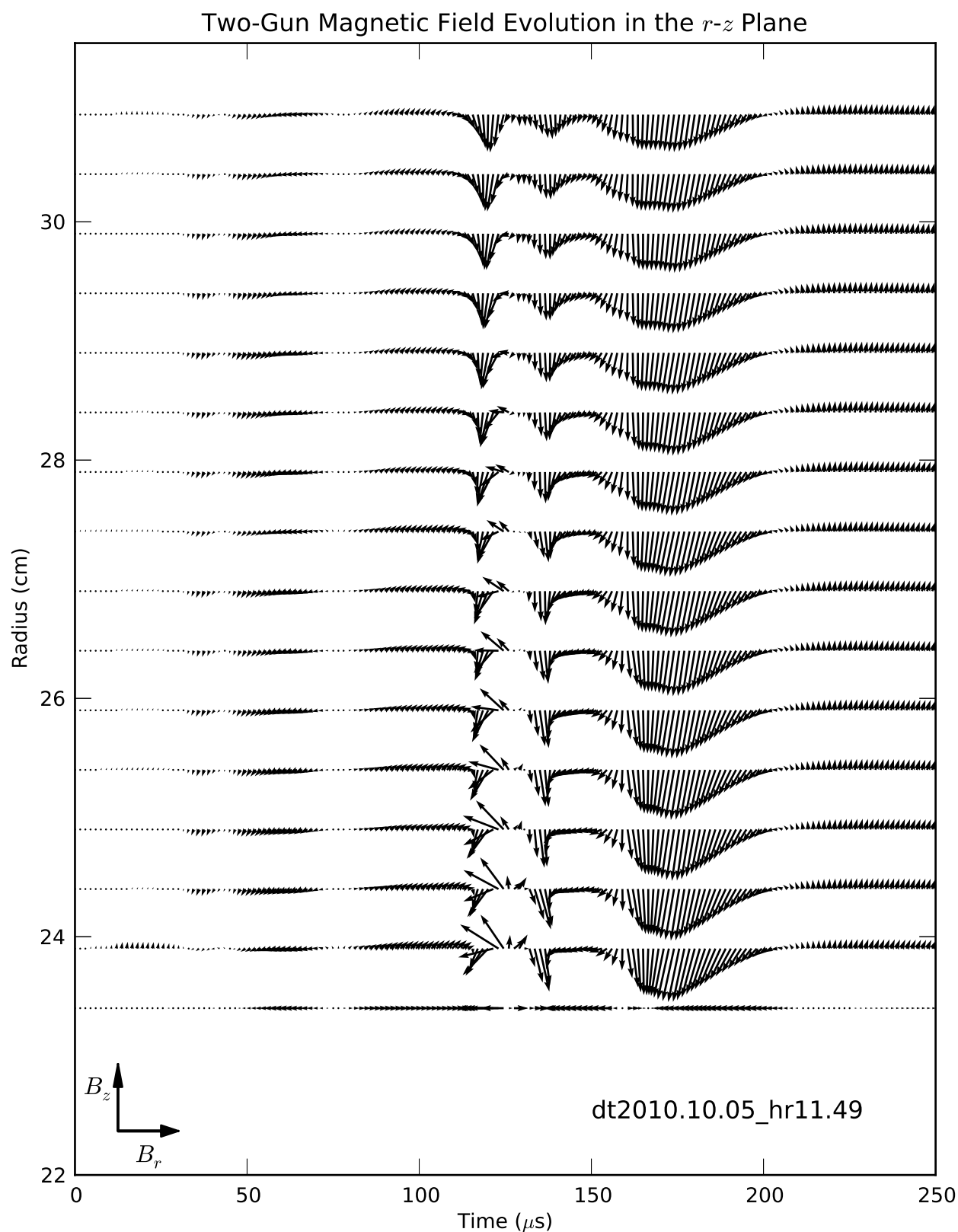


Figure 3.37: Projection of magnetic field in the r - z plane as a function of time and radius. The rotation of \mathbf{B} near $t = 125 \mu\text{s}$ varies strongly along the probe. Both the radial variation and the fast temporal scale for the motion suggest that a localized magnetic structure is passing by the probe. The increase in B_z after $t = 150 \mu\text{s}$ may indicate the formation of a merged object.

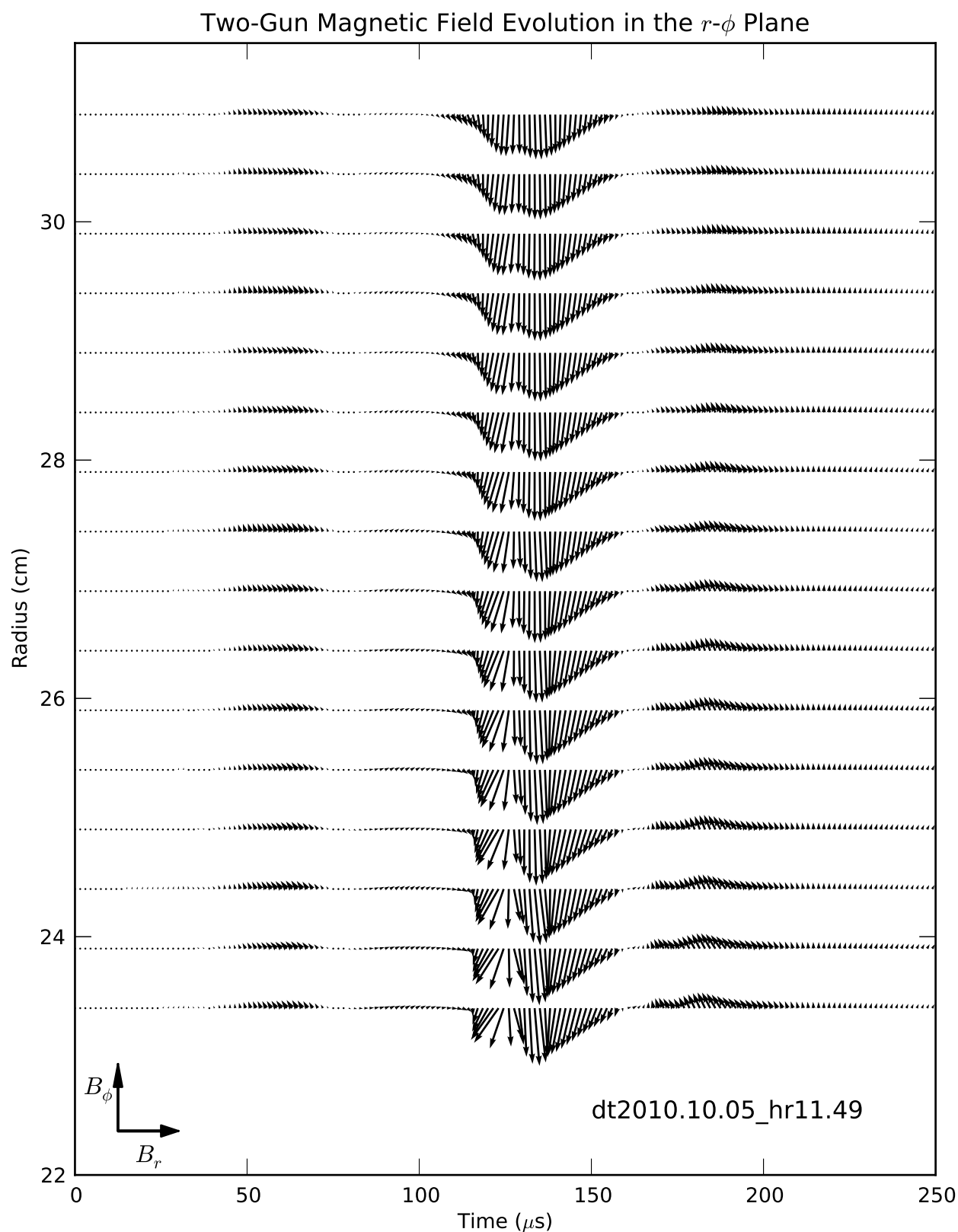


Figure 3.38: Projection of magnetic field in the r - ϕ plane as a function of time and radius. The change in B_r near $t = 125 \mu\text{s}$ is again visible, but B_ϕ is more or less uniform in radius. The strong reduction of B_ϕ just after $t = 150 \mu\text{s}$ may indicate annihilation of toroidal field.

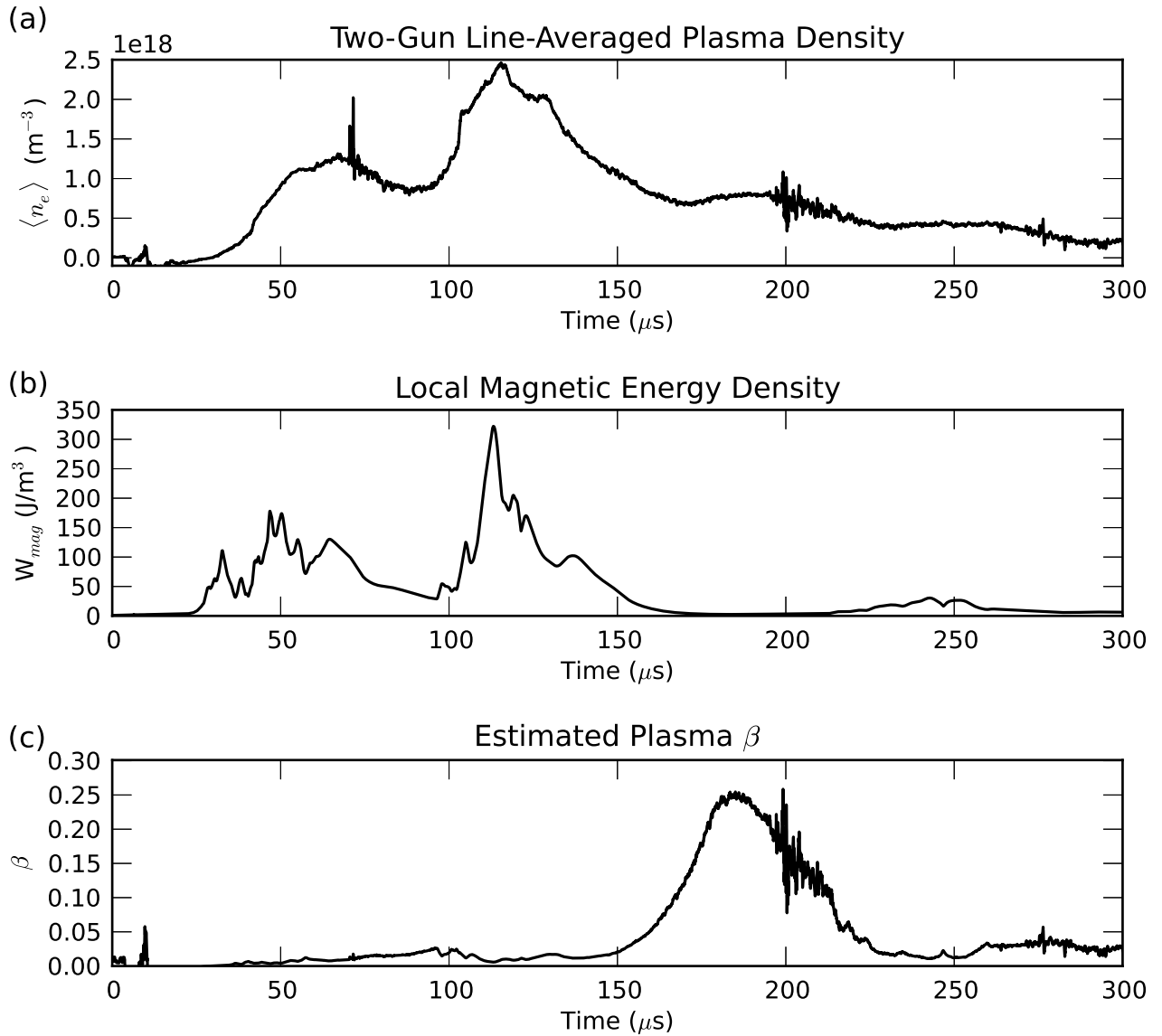


Figure 3.39: Evolution of (a) line-average density, (b) local magnetic energy density, and (c) plasma β . The temperature used for estimating β is 10 eV. Density timestamps = 'dt2010.02.15_hr + ['14.30','14.35','14.39','14.51','14.56','15.05','15.12','15.17','15.21','15.31']. Magnetic timestamps = 'dt2010.11.02_hr' + ['11.17','11.35','11.45','12.15','12.54'].

time history of the the density, magnetic energy, and estimated β value, averaged over a number of two-gun shots at parameters as similar as possible ($\lambda_{\max} \approx 30 \text{ m}^{-1}$). Density measurements are taking with gun voltages of 6 kV and magnet voltages of 300 V, while magnetic measurements are taken with gun voltages of 9 kV and magnet voltages of 500 V. Plasma β is estimated using the line averaged density and a temperature of 10 eV, similar to what is observed in SSX [126]. A change in temperature or density will change the overall scale of β , but not the time-evolution profile. Strong increases in density (e.g. Fig. 3.35) are only observed during two-gun shots. The local magnetic energy decays more quickly than the density, a potential indication of conversion of magnetic to kinetic energy. However, the plasma β (ratio of kinetic to magnetic pressure) does not reflect a high-beta, FRC-like equilibrium during the density peak ($t \sim 100 - 130 \mu\text{s}$).

For comparison, Figure 3.40 shows shot-averaged density, magnetic energy, and estimated β traces for single gun traces operating at 6 kV/300 V ($\lambda_{\max} \approx 30 \text{ m}^{-1}$). Note that the scales are the same as in Figure 3.39. The peak plasma density and magnetic energy density are both lower by a factor of 3 than the two-gun average. This indicates that the objects produced from two-gun merging are distinct from two single-gun objects.

The CFRC machine and diagnostics were still under development at the time of shutdown, which makes physical interpretation difficult at best. If the project is resumed in the future, one of the first steps to take will be construction and verification of a simple, but global, set of diagnostics. I suggest that a set of magnetic coils with large coil spacing should be constructed for measurements of the global magnetic field structure. Only after we are able to make a plausible identification of the objects formed in CFRC can we proceed with linking fluctuations to the configuration itself.

Status notes:

Data not known to be invalid is sparse. There are no shots combining the interferometer with the properly grounded/terminated 48-channel probe. The last interferometer data is from February 15th, 2010, and the 48-channel probe was not fixed until August 6th, 2010. It became almost impossible to run the vacuum system and the interferometer simultaneously once the building water pressure dropped in the spring of 2009. We installed a chiller for the diffusion pumps, the

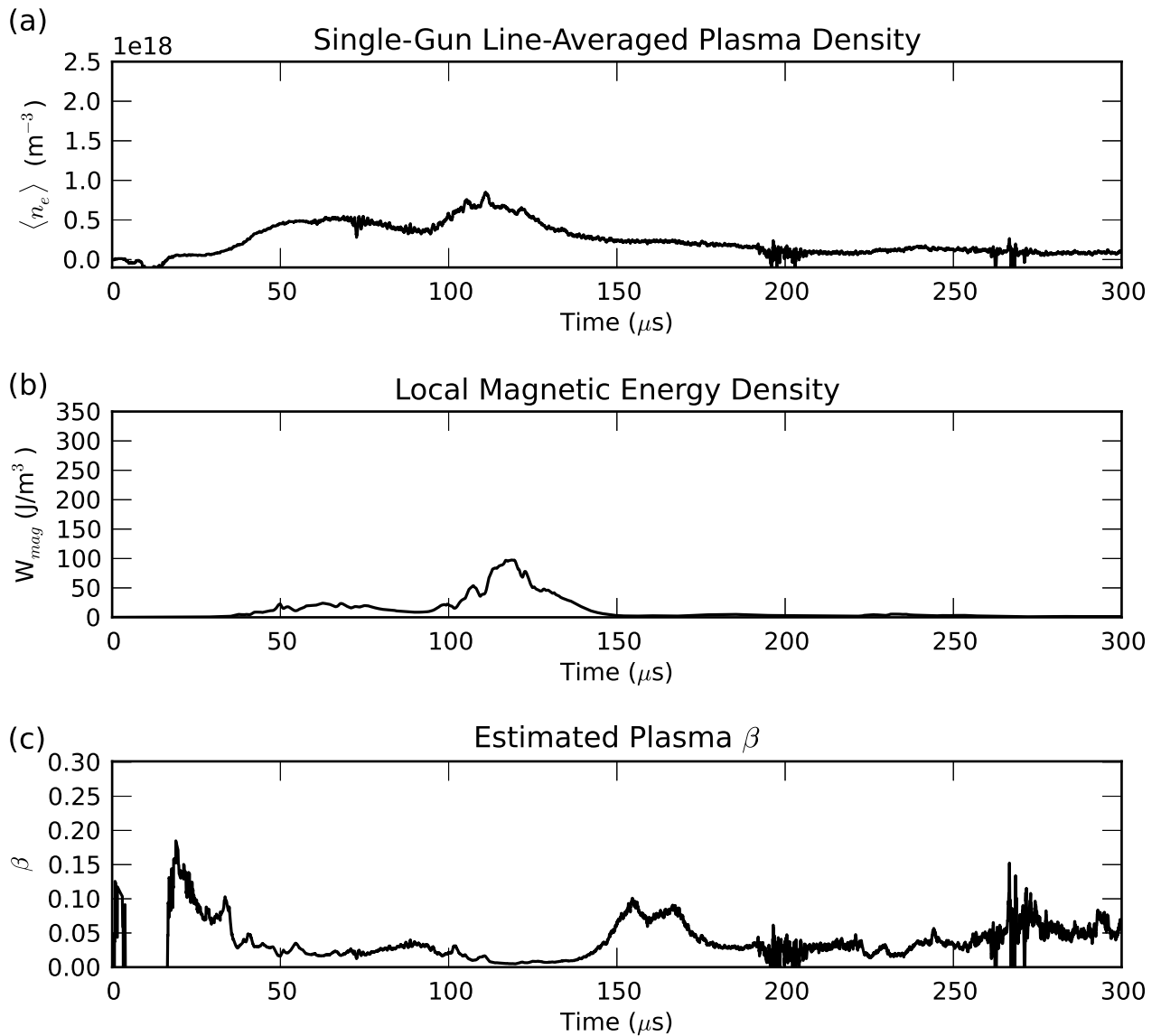


Figure 3.40: Evolution of (a) line-average density, (b) local magnetic energy density, and (c) plasma β . The temperature used for estimating β is 10 eV. Density timestamps = 'dt2009.10.27_hr' + ['10.34', '10.38', '10.41', '11.22', '11.25', '11.28', '11.31']. Magnetic timestamps = 'dt2010.09.28_hr' + ['10.27', '10.30', '10.33', '10.40', '10.44', '10.48'].

AOM, and the laser in August of 2009, but the output pressure is not high enough to run all three without small fluctuations tripping a flow interlock. In addition, the interferometer signal continued to degrade, but the obstruction of the lower windows by dust and debris was not diagnosed until the project had already ended. There are no shots at all with a functional triple probe (see status notes for section 3.3.3.1). The Mach probe tips were biased incorrectly (for electron collection) until

February 14th, 2010, and the circuit had a flaw that was not corrected until June of 2010 (see status notes for Section 3.3.3.2). Essentially, there is no overlap between density measurements and proper magnetic fluctuation measurements, there is no overlap between multiple density measurements, and there are no temperature measurements at all.

Grounding is an issue with any pulsed-power environment, and CFRC is no exception. An attempt was made to ground diagnostics only at the digitizer (no cable shields connected on the machine end). Nevertheless, noise from the discharge is an issue for all the diagnostics.

A simple flux conserver was built in an attempt to bring CFRC closer to SSX parameters, so that we might have better luck inferring spheromak formation by comparison with their results. Although the resistive time of the stainless wall is ~ 1 ms, the shape of the CFRC chamber outside the gun is not a simple cylinder (see Fig. 3.4). A simple calculation indicates that with the chamber volume, CFRC can only operate at approximately 10% of the magnetic energy of SSX spheromaks [131]. The flux conserver was meant to reduce the volume of the chamber by a factor of ~ 4 , increasing the magnetic energy density by the same factor. The full implementation involves two sections that can be bolted to the outer electrode of each gun. Each section is a $32'' \times 50'' \times 0.08''$ sheet of Cu 110 rolled into a cylinder and riveted at the seam. At one end, slits are cut in the sheet and the tabs in between bent 90-degrees outwards to form a flange attaching to the outer gun electrode. The thickness was chosen to match the upper limit of the roller in the professional department machine shop, and corresponds to three skin depths at a frequency of 10 kHz. Only one side has been constructed so far, and it was never installed or tested. The plan for installation was to place the flux conserver inside the chamber, re-install the gun and close the door, then bolt the flux conserver to the gun through the side ports.

3.4 Wave Measurements Using High-Resolution Magnetics

One of the major goals of CFRC was to estimate the spectral characteristics of fluctuations in an FRC. Although we cannot yet describe our observations in the context of FRC equilibrium or instability, we have developed a technique to extract the relevant spectral information. This

section describes the extraction of experimental dispersion plots (cf. Section 2.4.2) from magnetic probe data.

The extensive work by E.J. Powers and colleagues in the 1980s set the groundwork for spectral estimation from probe data. Various techniques were explored, including cross-spectral-density [16], maximum-entropy [149], and complex demodulation [150] methods. We have modified the standard cross-spectral-density estimate described in Ref. 16 to study non-time-stationary fluctuations by using channel-averaging instead of time-block-averaging. Conventional CSD analysis relies on the statistical time-stationarity of the fluctuations in the discharge [3]. Maximum entropy or maximum likelihood methods [149], which are well suited for spectral analysis of short time series, require a somewhat arbitrary optimization process that can be computationally intensive [151]. By using multiple spatial channels, we can avoid the time-block averaging typically used to weight CSD phase information. In this way, we can obtain spatial fluctuation spectra from a short time series with higher resolution than can be obtained by spatial Fourier transform of the same number of channels. The method employed here is direct, simple to implement, not limited by the spatial Nyquist frequency, and does not require intensive computation.

As described in Section 1.2.2, the typical two-point technique uses the CSD to estimate the spectral power and mean wavenumber associated with each frequency. The procedure involves calculating the cross-phase between two signals with known spatial locations. To facilitate a self-contained discussion, the relevant mathematics is summarized here. A single CSD estimate for the signals $x(t_j)$ and $y(t_j)$ is defined to be:

$$G_{xy}(f_j) = \frac{2}{T} X^*(f_j) Y(f_j), \quad (3.35)$$

where T is the length of the time record ($T = N\Delta t$), and X and Y represent the discrete Fourier transforms (FFTs) of x and y . Because the statistical uncertainty in this estimate is of order one, an average over multiple estimates is necessary to provide quantitative results. In the usual implementation [16], each signal is broken into n_d distinct time blocks of length T_d and the full

CSD is defined by Eq. 1.2:

$$\hat{G}_{xy}(f_j) = \frac{2}{n_d T_d} \sum_{i=1}^{n_d} X_i^*(f_j) Y_i(f_j). \quad (3.36)$$

$\hat{G}_{xy}(f_j)$ is a complex quantity, and the cross-phase as a function of frequency is given by the phase angle:

$$\tan \phi_{xy} = \text{Im } \hat{G}_{xy} / \text{Re } \hat{G}_{xy}. \quad (3.37)$$

For two probe signals (time series), a local wavenumber can be calculated for each frequency by dividing the cross-phase by the separation between the probe locations \mathbf{r}_x and \mathbf{r}_y :

$$K_l = \frac{\phi_{xy}}{(\mathbf{r}_x - \mathbf{r}_y)_l}, \quad (3.38)$$

where l indicates a vector component. For one pair of time-series, the above method produces a single K value at each frequency f_j . This limitation means that only the **average** K (power-weighted) and its uncertainty are measured. The statistical uncertainty in K comes from the uncertainty in the cross-phase (disregarding position and other measurement uncertainties), and is an estimate of the spectral width:

$$\sigma_\phi = \frac{(1 - \gamma_{xy}^2)^{1/2}}{|\gamma_{xy}| \sqrt{2n_d}} \quad (3.39)$$

Calculating the wavenumber in this way requires $n_d T_d$ to be smaller than the characteristic time for temporal variations in the spectrum, τ_s . This is a severe limitation in our case, since $\tau_s \sim 10 \mu s$. Our data acquisition (DAQ) rate of 40 MS/s is sufficient to allow a small number of blocks, but the frequency resolution is poor in this case.

In addition, we seek the full two-dimensional distribution of spectral power in frequency and wavenumber space, (not just the power and mean wavenumber versus frequency). If the local wavenumber at each frequency is calculated from each raw CSD estimate rather than from the smooth estimate, a two-dimensional result can be obtained. The ensemble of $(|G_{xy}|, K, \omega)$ triplets from the raw estimates are assembled into a histogram, summing the power in each bin (K_m, f_j) and dividing by n_d . Construction of the histogram is analogous to ensemble averaging and produces a smooth estimate $\hat{H}_{xy}(K_m, f_j)$. Although the histogram technique provides a two-dimensional result

(assuming sufficient statistical spread in K_m), it still reflects only the mean K and spectral width at each frequency. This is a fundamental limitation of using only two measurement locations; a single probe pair can provide only two constraints on the spatial properties [17]. While appropriate for cases where a single wave-like fluctuation is present, this technique cannot separate multiple bands of fluctuations (more than one distinct k at each frequency).

Instead of dividing our time series into smaller blocks, we instead average across multiple simultaneous measurement channels with varied spacings. By trading spatial resolution for time resolution, spectral estimates of sufficient frequency resolution and statistical uncertainty can be obtained from short-duration signals. We also collect non-redundant measurements in this way, circumventing the two-probe limitation described above (see Section 1.2.3). An estimate G_{xy} is calculated for each pair of probe channels over a time interval $N\Delta t$. These estimates are binned together by frequency and wavenumber, and the histogram values, $\hat{H}_{xy}(K_m, f_j)$, are weighted by the sum of the corresponding CSD amplitudes. This procedure averages out statistical errors in each estimate while retaining signals that are coherent across multiple channels. The primary limitation of the technique is that localized fluctuations are washed out (wavepackets with extent smaller than some of the pair spacings are diluted by the histogram).

The range of measurable k -values is bounded by the spacing of the coils and by the signal-to-noise ratio (SNR) of the measurement. The coil spacing of our probe gives an upper (Nyquist) limit of $k_{max} = 2\pi/\Delta z_{min} \approx 1200 \text{ m}^{-1}$. For a long wavelength fluctuation, being able to distinguish the signals at channels 1, 8, and 16 gives enough points to extract the amplitude, wavelength, and phase. For a given SNR $\sim B/\delta B$, $k_{min} \approx \sqrt{(8/L^2)(\delta B/B)}$, where L is the largest channel separation (\sim probe length). Using the best case ($\delta B/B \sim 0.002 = 4\text{-bit signal} / \text{digitizer range}$) and worst case ($\delta B/B = 1$) scenarios, we have $1 \text{ m}^{-1} < k_{min} < 30 \text{ m}^{-1}$. Since our noise level is relatively consistent, the minimum k value is determined primarily by the amplitude of the fluctuations. The spectral intensity maps calculated from data generally have a band of noise at low k due to this measurement floor.

A variety of interesting spectral signatures are observed using this technique, but it is difficult

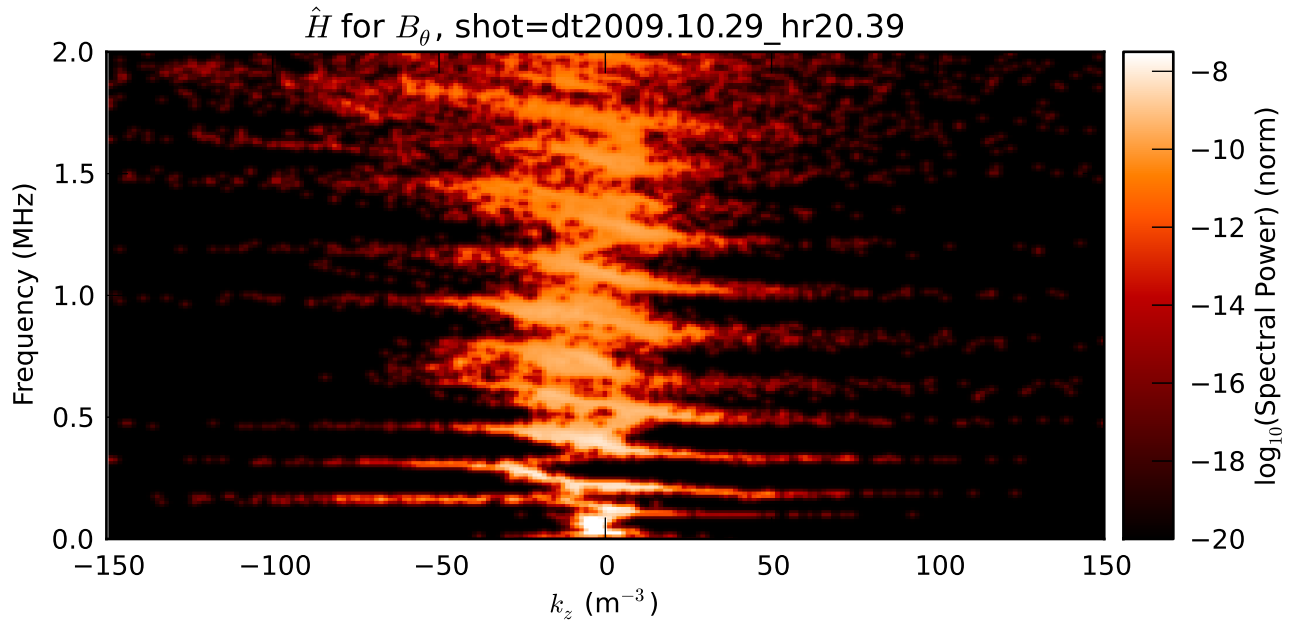


Figure 3.41: Spectral intensity plot demonstrating fluctuations suggestive of ion-cyclotron-harmonic or ion Bernstein waves. The time frame used is $[130,210] \mu s$.

to make any connection to a physical process. As discussed in Section 3.3.4, we do not know the global structure or dynamics of the plasma objects produced in CFRC, so we cannot do more than guess at what kinds of fluctuations are likely. From an empirical standpoint, there are few observations where a separation of mean and fluctuation timescales can be made (dynamics are non-stationary), which makes a discussion of waves in the traditional, linear sense inapplicable. Nevertheless, as an example of the application of the technique, the two-dimensional spectral density from an interesting case is shown in Figure 3.41. This shot was chosen because there exists a simultaneous interferometer trace, although 48-channel probe was not properly grounded at this time (see Section 3.3.3.4). The effects of ground loops on time scales much faster than the discharge current are assumed to be negligible. Signatures of spectral power at approximate multiples of a frequency in the ion-cyclotron range suggests that the fluctuations are associated with ion cyclotron harmonics. Ion Bernstein waves [152, 153] and ion-cyclotron-harmonic waves [154, 155, 156] have both been discussed in the context of reconnection and particle heating [157, 158, 159]. If we are forming a merged object, we might expect either or both of these waves to be driven by the merging

process.

Despite our attempt to improve the effective time resolution of our spectral-density analysis technique (eliminating time-block averaging), we still do not have a sufficient acquisition rate to localize the result on the time scale of the evolution of CFRC plasma objects with adequate frequency resolution. The above plot was constructed using a time window much longer than the duration of the oscillations observed. A minimum signal length of $\sim 50 \mu\text{s} = 200$ points is required to obtain sufficiently fine frequency resolution to detect the shape of the dispersion curves ($\sim 0.1 f_{ci}$). By shifting the time window and observing the change in the spectral density, we can verify that the fluctuations whose dispersion pattern is shown in Figure 3.41 occur in the range $t = 130 - 140 \mu\text{s}$. Care is needed to extract the spectral signature of fluctuations from a particular time window (during an equilibrium phase or the linear growth phase of an instability, for example).

An illustration of the sensitivity of our technique to the non-stationarity of our data is given in Figure 3.42. The density trace shown in (a) indicates an abrupt change in the plasma over a period of a few microseconds. A dashed vertical line is drawn to indicate the onset of the abrupt rise in density at $t = 131 \mu\text{s}$ [also indicated in (b) and (c)]. There is an accompanying change in the magnetic signals for the azimuthal field component (b), although the magnetics indicate a significant event beginning several microseconds before the density change. A zoomed-in plot of the raw $\partial_t B_\phi$ data for the magnetic ‘event’ is shown in (c). Two features are particularly noteworthy. First, there is a strong, slanted peak between 129 and $130 \mu\text{s}$, indicating a localized structure passing across the probe. The constant slant of this peak (time location versus channel position) corresponds to a velocity on the order of 50 km/s , consistent with the transit velocity of plasma launched from the gun (see Figure 3.29 and accompanying discussion). Second, the fluctuations following the onset of the density increase are non-uniform along the probe.

The spectral intensity corresponding to the entire magnetic event is shown in (d). In order to obtain sufficient frequency resolution a large time window is used, centered on the event [indicated by 45° hashed region in (b)]. The spectral signature is dominated by the propagating feature described above. This is no longer true if only the latter part of the event is considered (after the

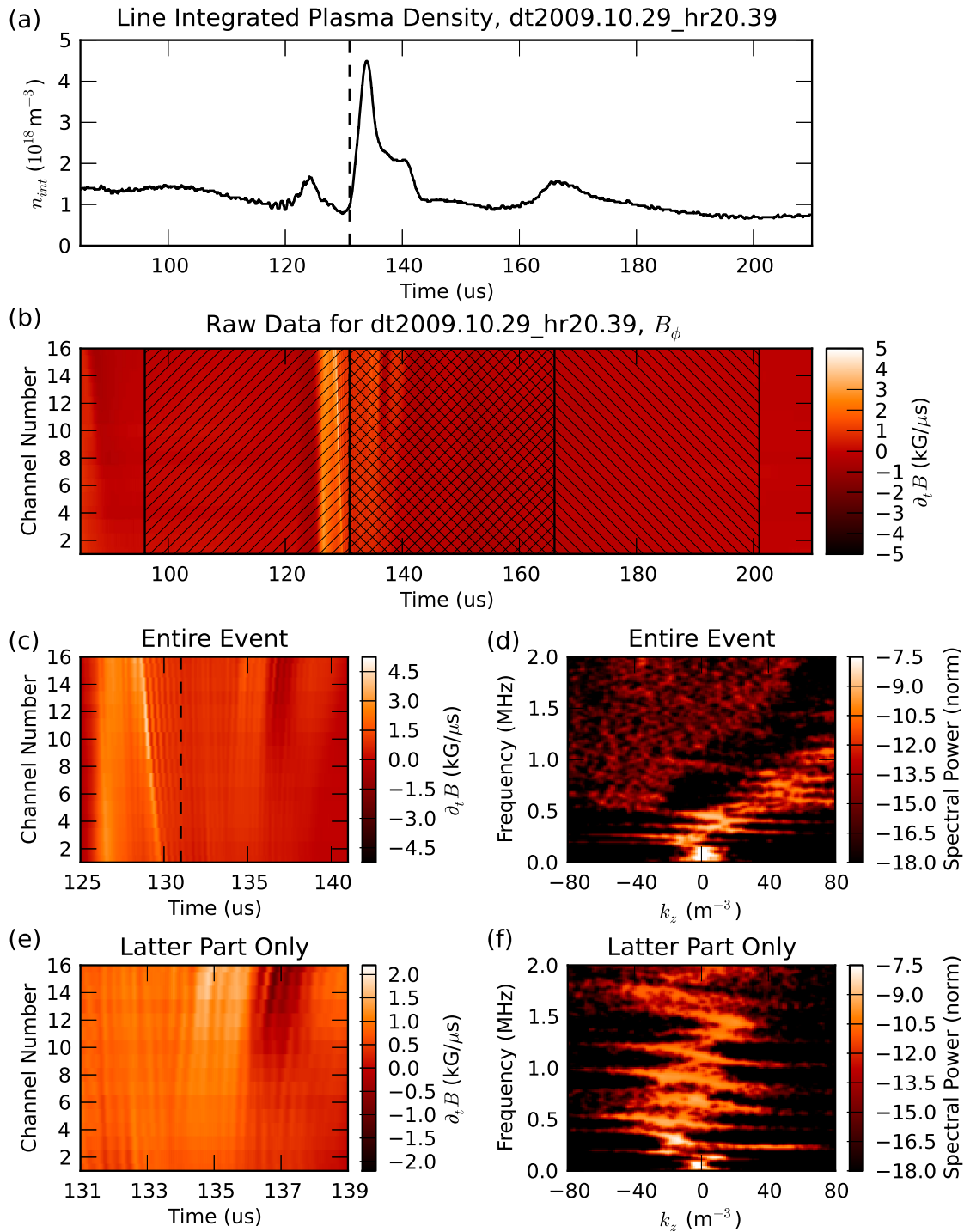


Figure 3.42: Comparison of spectral intensity derived from different time windows. (a) Line-average density trace. The vertical dashed line indicates the onset time of the density rise in (a)-(c). (b) Intensity plot of raw $\partial_t B_\phi$ data surrounding a single magnetic ‘event’. Hashed regions indicate the two different time blocks used for spectral intensity calculations. (c) Zoomed in plot of data during the event. (d) Spectral intensity derived from a time window centered on the event, $t = 93 - 153 \mu\text{s}$ (45° hash). (e) Zoomed in plot of data after signature of propagating structure subsides. (f) Spectral intensity derived from a time window including only the latter part of the event, $t = 131 - 191 \mu\text{s}$ (135° hash).

propagating feature occurs). A further zoomed-in plot of the raw data is shown in (e), and the spectral signature corresponding to the (equal-length) time window indicated by the 135° hashed region in (b) is shown in (f). The spectrum is no longer dominated by the propagating feature.

The data in Figure 3.41 is calculated using all possible pairs of probe channels. Given the non-uniformity along the probe apparent in Figure 3.42(e), it is useful to compare spectral intensities derived from a smaller number of pairs (higher statistical uncertainty) localized in radius. Figure 3.43 compares the spectral intensity calculated using only the outer (a) or inner (b) half of the probe channels. It is clear that the cyclotron-harmonic spectral feature is localized primarily on the inner probe channels ($r \leq 27.5$ cm).

The above example makes explicit the limitations of the 48-channel probe and of our analysis technique. Many of the fluctuations observed to date on CFRC are non-stationary on both the temporal and spatial scales of interest. In the current mode of operation, where brief magnetic events are separated by large zero-signal regions, it is still possible to extract some spectral information with appropriate frequency resolution. In the future, an optimized time-frequency technique, such as wavelet analysis [160], should be adapted to extract two-dimensional spectral intensity from the magnetic probe data. By choosing an appropriate wavelet, the balance between frequency resolution and time-localization can be adjusted as necessary. We are optimistic that continued development of the method presented here can allow the identification of modes driven by spheromak merging, as well as signatures of instability.

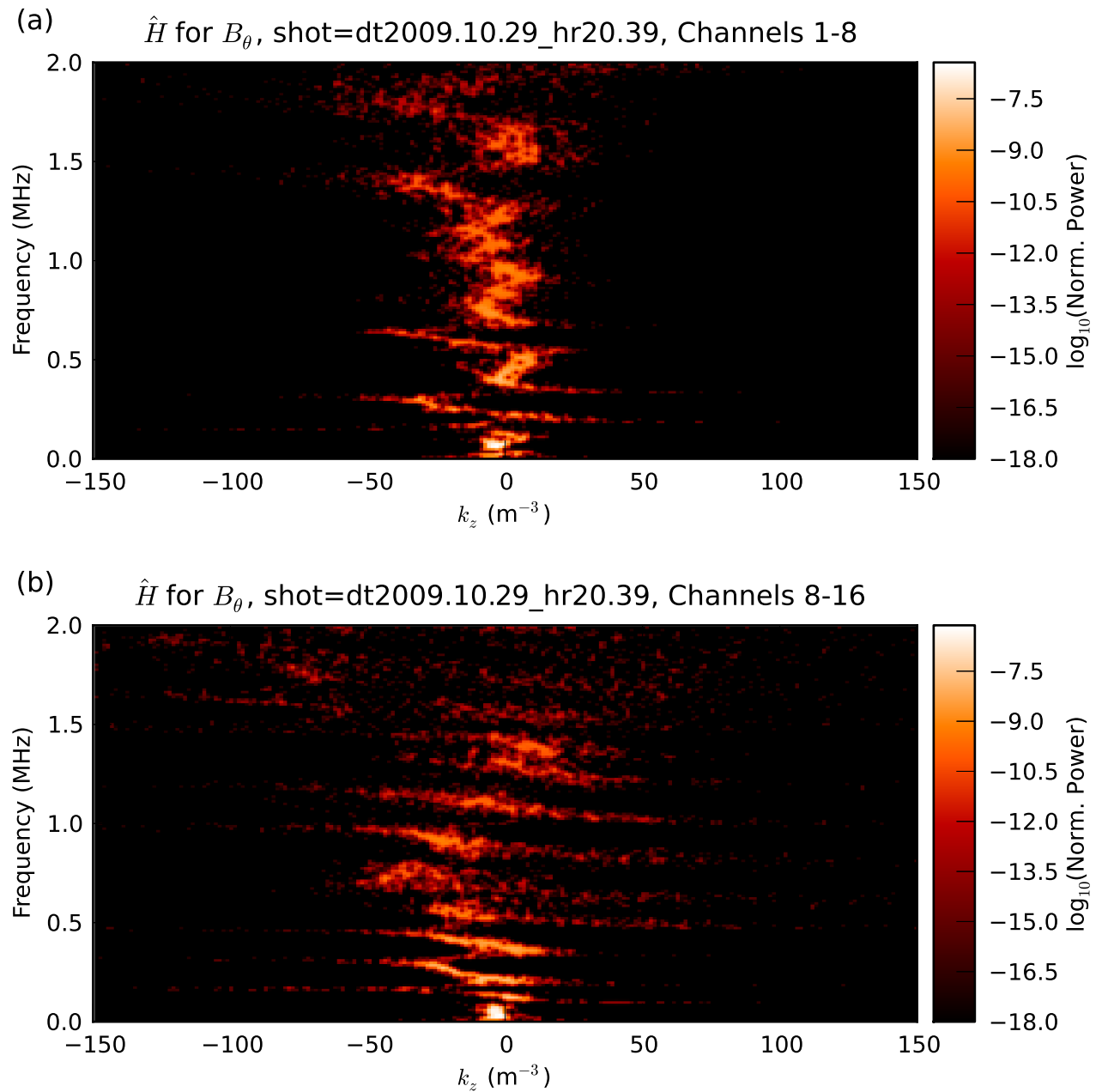


Figure 3.43: Comparison of spectral intensity plots using (a) only the outer 8 channels and (b) only the inner 8 channels. The time frame used is $[130,210] \mu s$. The feature with harmonic features in the ion-cyclotron frequency range is localized to the inner half of the probe.

Bibliography

- [1] Thomas Howard Stix. Waves in Plasmas. American Institute of Physics, New York, 2 edition, 1992.
- [2] Stephen B. Pope. Turbulent Flows. Cambridge University Press, New York, 2000.
- [3] J.S. Bendat and A.G. Piersol. Random Data. Wiley, New York, 3rd edition, 2000.
- [4] D. L. Brower, W. A. Peebles, N. C. Luhmann, and R. L. Savage. Multichannel scattering studies of the spectra and spatial distribution of tokamak microturbulence. Physical Review Letters, 54(7):689–692, Feb 1985.
- [5] S.J. Levinson, J.M. Beall, E.J. Powers, and R.D. Bengtson. Space/time statistics of the turbulence in a tokamak edge plasma. Nuclear Fusion, 24(5):527–539, May 1984.
- [6] U. Kauschke, G. Oelerich-Hill, and A. Piel. Experimental investigation of coherent drift waves in low magnetic fields. Physics of Fluids B: Plasma Physics, 2(1):38–43, Jan 1990.
- [7] C. X. Yu, D. L. Brower, S. J. Zhao, W. A. Peebles, N. C. Luhmann, R. V. Bravenec, J. Y. Chen, H. Lin, Ch P. Ritz, P. M. Schoch, and X. Z. Yang. Comparison of the density fluctuation spectrum and amplitude in text with expectations for electron drift waves. Physics of Fluids B: Plasma Physics, 4(2):381–385, Feb 1992.
- [8] R. Jha, P. K. Kaw, S. K. Mattoo, C. V. S. Rao, Y. C. Saxena, and the ADITYA Team. Intermittency in tokamak edge turbulence. Physical Review Letters, 69(9):1375–1378, Aug 1992.
- [9] G. Prasad, D. Bora, Y. C. Saxena, and S. D. Verma. Experimental study of lowfrequency turbulence in a toroidal plasma. Physics of Plasmas, 1(6):1832–1840, Jun 1994.
- [10] A. Latten, T. Klinger, A. Piel, and Th Pierre. A probe array for the investigation of spatiotemporal structures in drift wave turbulence. Review of Scientific Instruments, 66(5):3254–3262, May 1995.
- [11] C. Riccardi, D. Xuantong, M. Salierno, L. Gamberale, and M. Fontanesi. Experimental analysis of drift waves destabilization in a toroidal plasma. Physics of Plasmas, 4(11):3749–3758, Nov 1997.
- [12] B. H. Deng, D. L. Brower, G. Cima, C. W. Domier, N. C. Luhmann, and C. Watts. Mode structure of turbulent electron temperature fluctuations in the texas experimental tokamak upgrade. Physics of Plasmas, 5(12):4117–4120, Dec 1998.

- [13] A. Fasoli, B. Labit, M. McGrath, S. H. Müller, G. Plyushchev, M. Podestà, and F. M. Poli. Electrostatic turbulence and transport in a simple magnetized plasma. Physics of Plasmas, 13(5):055902–0559029, May 2006.
- [14] T Lan, A D Liu, C X Yu, L W Yan, W Y Hong, K J Zhao, J Q Dong, J Qian, J Cheng, D L Yu, and et al. Spectral characteristics of geodesic acoustic mode in the hl-2a tokamak. Plasma Physics and Controlled Fusion, 50(4):045002, Apr 2008.
- [15] C Silva, P Duarte, H Fernandes, and H Figueiredo. Interaction between mean and fluctuating eb shear flows on the isttok edge plasma. Plasma Physics and Controlled Fusion, 54(8):085013, Aug 2012.
- [16] J. M. Beall, Y. C. Kim, and E. J. Powers. Estimation of wavenumber and frequency spectra using fixed probe pairs. Journal of Applied Physics, 53(6):3933–3940, Jun 1982.
- [17] A. W. Carlson. The distribution of fluctuation measurements within the randomphase model. Journal of Applied Physics, 70(8):4028–4032, Oct 1991.
- [18] B. Tobias, A. J.H Donné, H. K Park, J. E Boom, M. J Choi, I. G.J Classen, C. W Domier, X. Kong, W. Lee, T. Liang, N.C Luhmann, Jr., T. Munsat, L. Yu, and G.S. Yun. Imaging techniques for microwave diagnostics. Contributions to Plasma Physics, 51(23):111–118, Mar 2011.
- [19] Tobin Munsat, Calvin W. Domier, Xiangyu Kong, Tianran Liang, Jr. Luhmann, Benjamin J. Tobias, Woochang Lee, Hyeon K. Park, Gunsu Yun, Ivo. G. J. Classen, and Anthony J.H. Donné. Electron cyclotron emission imaging in tokamak plasmas. Applied Optics, 49(19):E20–E30, Jul 2010.
- [20] G. R. McKee, C. Fenzi, R. J. Fonck, and M. Jakubowski. Turbulence imaging and applications using beam emission spectroscopy on DIII-D (invited). Review of Scientific Instruments, 74(3):2014, 2003.
- [21] D.H.J. Goodall. High speed cine film studies of plasma behaviour and plasma surface interactions in tokamaks. Journal of Nuclear Materials, 111–112(0):11–22, Nov 1982.
- [22] S. J. Zweben and S. S. Medley. Visible imaging of edge fluctuations in the TFTR tokamak. Physics of Fluids B: Plasma Physics, 1(10):2058–2065, Oct 1989.
- [23] R. J. Maqueda, G. A. Wurden, S. Zweben, L. Roquemore, H. Kugel, D. Johnson, S. Kaye, S. Sabbagh, and R. Maingi. Edge turbulence measurements in NSTX by gas puff imaging. Review of Scientific Instruments, 72:931, 2001.
- [24] S.J Zweben, R.J Maqueda, D.P Stotler, A Keese, J Boedo, C.E Bush, S.M Kaye, B LeBlanc, J.L Lowrance, V.J Mastrocola, R. Maingi, N. Nishino, G. Renda, D.W. Swain, J.B. Wilgen, and the NSTX Team. High-speed imaging of edge turbulence in NSTX. Nuclear Fusion, 44(1):134–153, Jan 2004.
- [25] A Kirk, N Ben Ayed, G Counsell, B Dudson, T Eich, A Herrmann, B Koch, R Martin, A Meakins, S Saarelma, R Scannell, S Tallents, M Walsh, Wilson H.R, and the MAST team. Filament structures at the plasma edge on MAST. Plasma Physics and Controlled Fusion, 48(12B):B433–B441, Dec 2006.

- [26] S. J. Zweben, R. J. Maqueda, J. L. Terry, T. Munsat, J. R. Myra, D. D'Ippolito, D. A. Russell, J. A. Krommes, B. LeBlanc, T. Stoltzfus-Dueck, D.P. Stotler, K.M. Williams, C.E. Bushe, R. Maingi, O. Grulke, S.A. Sabbagh, and A.E. White. Structure and motion of edge turbulence in the National Spherical Torus Experiment and Alcator C-Mod. Physics of Plasmas, 13(5):056114, 2006.
- [27] N. Ben Ayed, A. Kirk, B. Dudson, S. Tallents, R. G. L. Vann, H. R. Wilson, and the MAST team. Inter-ELM filaments and turbulent transport in the Mega-Amp Spherical tokamak. Plasma Physics and Controlled Fusion, 51(3):035016, Mar 2009.
- [28] J. H. Yu, M. A. Van Zeeland, M. S. Chu, V. A. Izzo, and R. J. La Haye. Fast imaging of transients and coherent magnetohydrodynamic modes in DIII-D. Physics of Plasmas, 16(5):056114, Apr 2009.
- [29] Mengzhou Zhu, Ge Zhuang, Zhijiang Wang, Yonghua Ding, Li Gao, Xiwei Hu, and Yuan Pan. A visible light imaging system for the estimation of plasma vertical displacement in J-TEXT. Plasma Science and Technology, 12(6):641–645, Dec 2010.
- [30] E. de la Cal, J. Guasp, and the TJ-II Team. Two-dimensional imaging of edge plasma electron density and temperature by the passive helium emission ratio technique in TJ-II. Plasma Physics and Controlled Fusion, 53(8):085006, Aug 2011.
- [31] Y. Sechrest, T. Munsat, D. A. D'Ippolito, R. J. Maqueda, J. R. Myra, D. Russell, and S. J. Zweben. Flow and shear behavior in the edge and scrape-off layer of L-mode plasmas in National Spherical Torus Experiment. Physics of Plasmas, 18(1):012502, 2011.
- [32] E.W. Hemsing, I. Furno, and T.P. Intrator. Fast camera images of flux ropes during plasma relaxation. IEEE Transactions on Plasma Science, 33(2):448 – 449, Apr 2005.
- [33] G. Y. Antar, J. H. Yu, and G. Tynan. The origin of convective structures in the scrape-off layer of linear magnetic fusion devices investigated by fast imaging. Physics of Plasmas, 14:022301, 2007.
- [34] J.H. Yu, C. Holland, G.R. Tynan, G. Antar, and Z. Yan. Examination of the velocity time-delay-estimation technique. Journal of Nuclear Materials, 363-365(0):728–732, Jun 2007.
- [35] S H Müller, C Theiler, A Fasoli, I Furno, B Labit, G R Tynan, M Xu, Z Yan, and J H Yu. Studies of blob formation, propagation and transport mechanisms in basic experimental plasmas (torpex and csdx). Plasma Physics and Controlled Fusion, 51:055020, May 2009.
- [36] G R Tynan, P H Diamond, C Holland, S H Müller, M Xu, Z Yan, and J Yu. Nonlinear dynamics of shear flows and plasma rotation in a simple laboratory plasma system. Plasma Physics and Controlled Fusion, 51:124055, Dec 2009.
- [37] D. Iraj, I. Furno, A. Fasoli, and C. Theiler. Imaging of turbulent structures and tomographic reconstruction of TORPEX plasma emissivity. Physics of Plasmas, 17(12):122304, 2010.
- [38] S. Oldenbürger, C. Brandt, F. Brochard, N. Lemoine, and G. Bonhomme. Spectroscopic interpretation and velocimetry analysis of fluctuations in a cylindrical plasma recorded by a fast camera. Review of Scientific Instruments, 81(6):063505, Jun 2010.

- [39] Z. Yan, G. R. Tynan, C. Holland, M. Xu, S. H. Müller, and J. H. Yu. Shear flow and drift wave turbulence dynamics in a cylindrical plasma device. Physics of Plasmas, 17:032302, 2010.
- [40] S. Oldenbürger, F. Brochard, and G. Bonhomme. Investigation of mode coupling in a magnetized plasma column using fast imaging. Physics of Plasmas, 18(3):032307, 2011.
- [41] M. Xu, G. R. Tynan, P. H. Diamond, C. Holland, J. H. Yu, and Z. Yan. Generation of a sheared plasma rotation by emission, propagation, and absorption of drift wave packets. Physical Review Letters, 107(5):055003, Jul 2011.
- [42] H. Tanaka, N. Ohno, Y. Tsuji, K. Okazaki, and S. Kajita. Statistical analysis of the spatial behavior of plasma blobs around the plasma column in a linear plasma device. Contributions to Plasma Physics, 52(5-6):424–428, 2012.
- [43] T. Ito and M. A. Cappelli. Electrostatic probe disruption of drift waves in magnetized microdischarges. Applied Physics Letters, 94:211501, 2009.
- [44] J. B. Parker, Y. Raitses, and N. J. Fisch. Transition in electron transport in a cylindrical Hall thruster. Applied Physics Letters, 97(9):091501, Sep 2010.
- [45] M.S. McDonald and A.D. Gallimore. Rotating spoke instabilities in Hall thrusters. IEEE Transactions on Plasma Science, 39(11):2952–2953, Nov 2011.
- [46] M Ramisch, F Greiner, N Mahdizadeh, K Rahbarnia, and U Stroth. Observation of large-scale coherent structures under strong exb shear in the torsatron TJ-K. Plasma Physics and Controlled Fusion, 49(6):777–789, Jun 2007.
- [47] M Ramisch, E Häberle, N Mahdizadeh, and U Stroth. Investigation of the perpendicular dynamics of drift-wave turbulence in a toroidal plasma with multi-probe arrays. Plasma Sources Science and Technology, 17(2):024007, May 2008.
- [48] A. D. Light, S. C. Thakur, C. Brandt, Y. Sechrest, G. R. Tynan, and T. Munsat. Direct extraction of coherent mode properties from imaging measurements in a linear plasma column. Physics of Plasmas, 20(8):082120, Aug 2013.
- [49] G R Tynan, C Holland, J H Yu, A James, D Nishijima, M Shimada, and N Taheri. Observation of turbulent-driven shear flow in a cylindrical laboratory plasma device. Plasma Physics and Controlled Fusion, 48(4):S51–S73, Apr 2006.
- [50] F. W. Perkins and D. L. Jassby. Velocity shear and lowfrequency plasma instabilities. Physics of Fluids, 14(1):102115, Jan 1971.
- [51] D. L. Jassby. Transverse velocity shear instabilities within a magnetically confined plasma. Physics of Fluids, 15(9):1590–1604, September 1972.
- [52] Max Light, Francis F. Chen, and P. L. Colestock. Low frequency electrostatic instability in a helicon plasma. Physics of Plasmas, 8(10):46754689, Oct 2001.
- [53] R F Ellis, E Marden-Marshall, and R Majeski. Collisional drift instability of a weakly ionized argon plasma. Plasma Physics, 22(2):113131, Feb 1980.

- [54] Albert Simon. Instability of a partially ionized plasma in crossed electric and magnetic fields. Physics of Fluids, 6(3):382–388, March 1963.
- [55] F. C. Hoh. Instability of PenningType discharges. Physics of Fluids, 6(8):1184–1191, August 1963.
- [56] John Wesson. Tokamaks. Oxford University Press, Inc., New York, 2 edition, 1997.
- [57] M. J. Burin, G. R. Tynan, G. Y. Antar, N. A. Crocker, and C. Holland. On the transition to drift turbulence in a magnetized plasma column. Physics of Plasmas, 12:052320, 2005.
- [58] P. Bellan. Fundamentals of Plasma Physics. Cambridge University Press, New York, 2006.
- [59] W. Horton. Drift waves and transport. Reviews of Modern Physics, 71(3):735, Apr 1999.
- [60] Ferdinand Cap. Handbook on Plasma Instabilities. Academic Press, Inc., New York, 1976.
- [61] Y.-Q. Tao, R. W. Conn, L. Schmitz, and G. Tynan. Collisionless simonhoh instability in a strongly doublesheared electric field. Physics of Plasmas, 1(10):31933198, Oct 1994.
- [62] Rayleigh. Investigation of the character of the equilibrium of an incompressible heavy fluid of variable density. Proceedings of the London Mathematical Society, s1-14(1):170177, Nov 1882.
- [63] Geoffrey Taylor. The instability of liquid surfaces when accelerated in a direction perpendicular to their planes. i. Proceedings of the Royal Society of London. Series A. Mathematical and Physical Sciences, 201(1065):192196, Mar 1950.
- [64] S. Chandrasekhar. Hydrodynamic and Hydromagnetic Stability. Dover Publications, Inc., New York, 1981 [Original 1961].
- [65] H. Hora, G. Min, Shalom Eliezer, P. Lalouis, R.S. Pease, and H. Szichman. On the surface tension of plasmas. IEEE Transactions on Plasma Science, 17(2):284289, 1989.
- [66] P. G. Drazin. Introduction to Hydrodynamic Stability. Cambridge University Press, Sep 2002.
- [67] G. K. Batchelor. An Introduction to Fluid Dynamics. Cambridge University Press, Feb 2000.
- [68] G R Tynan, M J Burin, C Holland, G Antar, and P H Diamond. Radially sheared azimuthal flows and turbulent transport in a cylindrical helicon plasma device. Plasma Physics and Controlled Fusion, 46:A373–A379, May 2004.
- [69] G. R. Tynan, M. J. Burin, C. Holland, G. Antar, N. Crocker, and P. H. Diamond. Radially sheared azimuthal flows and turbulent transport in a cylindrical plasma. Physics of Plasmas, 11:5195, 2004.
- [70] C. Holland, J. H. Yu, A. James, D. Nishijima, M. Shimada, N. Taheri, and G. R. Tynan. Observation of turbulent-driven shear flow in a cylindrical laboratory plasma device. Physical Review Letters, 96(19):195002, May 2006.
- [71] M. Xu, G. R. Tynan, C. Holland, Z. Yan, S. H. Müller, and J. H. Yu. Study of nonlinear spectral energy transfer in frequency domain. Physics of Plasmas, 16:042312, 2009.

- [72] M. Xu, G. R. Tynan, C. Holland, Z. Yan, S. H. Müller, and J. H. Yu. Fourier-domain study of drift turbulence driven sheared flow in a laboratory plasma. Physics of Plasmas, 17:032311, 2010.
- [73] G. R. Tynan, A. D. Bailey III, G. A. Campbell, R. Charatan, A. de Chambrier, G. Gibson, D. J. Hemker, K. Jones, A. Kuthi, C. Lee, and et al. Characterization of an azimuthally symmetric helicon wave high density plasma source. Journal of Vacuum Science & Technology A: Vacuum, Surfaces, and Films, 15(6):2885–2892, 1997.
- [74] I. D. Sudit and F. F. Chen. Rf compensated probes for high-density discharges. Plasma Sources Science and Technology, 3(2):162, May 1994.
- [75] I. H. Hutchinson. Principles of Plasma Diagnostics. Cambridge University Press, New York, 2002.
- [76] P.C. Stangeby. The disturbing effect of probes inserted into edge plasmas of fusion devices. Journal of Nuclear Materials, 121(0):36–40, May 1984.
- [77] C Holland, G R Tynan, J H Yu A James, D Nishijima, M Shimada, and N Taheri. Numerical simulations of collisional drift-wave turbulence in a magnetized plasma column. Plasma Physics and Controlled Fusion, 49:A109–A119, May 2007.
- [78] Nazli Taheri. Experimental study of the maxwell stress in electromagnetic collisional drift turbulence. Master’s thesis, University of California, San Diego, 2008.
- [79] Michael Burin. On Structure Formation and the Transition to Turbulence in a Magnetized Plasma Column. PhD thesis, University of California, San Diego, 2003.
- [80] Christian Brandt, Olaf Grulke, Thomas Klinger, José Negrete, Guillaume Bousselein, Frédéric Brochard, Gérard Bonhomme, and Stella Oldenbürger. Spatiotemporal mode structure of nonlinearly coupled drift wave modes. Physical Review E, 84(5):056405, Nov 2011.
- [81] Steven H. Strogatz. From Kuramoto to Crawford: exploring the onset of synchronization in populations of coupled oscillators. Physica D: Nonlinear Phenomena, 143(14):1 – 20, 2000.
- [82] Isaac D. Sudit and Francis F. Chen. Discharge equilibrium of a helicon plasma. Plasma Sources Science and Technology, 5(1):43, Feb 1996.
- [83] B. Nold, T. T. Ribeiro, M. Ramisch, Z. Huang, H. W. Müller, B. D. Scott, U. Stroth, and the ASDEX Upgrade Team. Influence of temperature fluctuations on plasma turbulence investigations with langmuir probes. New Journal of Physics, 14(6):063022, Jun 2012.
- [84] David D. Blackwell and Francis F. Chen. Two-dimensional imaging of a helicon discharge. Plasma Sources Science and Technology, 6(4):569, Nov 1997.
- [85] Jorge Manuel Muñoz Burgos. Atomic data generation and collisional radiative modeling of Ar II, Ar III, and Ne I for laboratory and astrophysical plasmas. PhD thesis, Auburn University, 2009.
- [86] Akira Hasegawa and Masahiro Wakatani. Plasma edge turbulence. Physical Review Letters, 50(9):682686, Feb 1983.

- [87] Akira Hasegawa and Kunioki Mima. Pseudothreedimensional turbulence in magnetized nonuniform plasma. Physics of Fluids (1958-1988), 21(1):8792, 1978.
- [88] R. Balbín, C. Hidalgo, M. A. Pedrosa, I. GarcíaCortés, and J. Vega. Measurement of density and temperature fluctuations using a fast swept langmuir probe. Review of Scientific Instruments, 63(10):46054607, Oct 1992.
- [89] G. Chiodini, C. Riccardi, and M. Fontanesi. A 400 khz, fast-sweep langmuir probe for measuring plasma fluctuations. Review of Scientific Instruments, 70(6):26812688, Jun 1999.
- [90] O. Troll, L. Conde, E. Criado, J. M. Donoso, and G. Herdrich. Measurements of plasma properties using fast sweep langmuir probes in unmagnetized weakly ionized plasmas. Contributions to Plasma Physics, 50(9):819823, 2010.
- [91] D. L. Rudakov, J. A. Boedo, R. A. Moyer, R. D. Lehmer, G. Gunner, and J. G. Watkins. Fast electron temperature diagnostic based on langmuir probe current harmonic detection on diii-d. Review of Scientific Instruments, 72(1):453456, Jan 2001.
- [92] H. Bruhns. Recent compact toroid research. Plasma Physics and Controlled Fusion, 28(9A):1389, September 1986.
- [93] P. Bellan. Spheromaks. Imperial College Press, London, 2000.
- [94] T. R. Jarboe. Review of spheromak research. Plasma Physics and Controlled Fusion, 36(6):945, June 1994.
- [95] M. Tuszewski. Field reversed configurations. Nuclear Fusion, 28(11):2033, November 1988.
- [96] Loren C. Steinhauer. Review of field-reversed configurations. Physics of Plasmas (1994-present), 18(7):070501, July 2011.
- [97] P. M. Bellan, J. Yee, and J. F. Hansen. Spheromaks, solar prominences, and alfvn instability of current sheets. Earth, Planets, and Space, 53:495499, Jun 2001.
- [98] Paul M. Bellan, Setthivoine You, and Scott C. Hsu. Simulating astrophysical jets in laboratory experiments. Astrophysics and Space Science, 298(1-2):203209, Jul 2005.
- [99] M. R. Brown. Experimental studies of magnetic reconnection. Physics of Plasmas, 6(5):17171724, May 1999.
- [100] Masaaki Yamada. Review of controlled laboratory experiments on physics of magnetic reconnection. Journal of Geophysical Research: Space Physics, 104(A7):1452914541, 1999.
- [101] Y. Ono, A. Morita, M. Katsurai, and M. Yamada. Experimental investigation of threedimensional magnetic reconnection by use of two colliding spheromaks. Physics of Fluids B: Plasma Physics (1989-1993), 5(10):36913701, Oct 1993.
- [102] Y. Ono, Y. Hayashi, T. Ii, H. Tanabe, S. Ito, A. Kuwahata, T. Ito, Y. Kamino, T. Yamada, M. Inomoto, and et al. Intermittent magnetic reconnection in ts-3 merging experiment. Physics of Plasmas, 18:111213, 2011.
- [103] L. C. Steinhauer, D. C. Barnes, and M. Binderbauer. Frc 2001: A white paper on frc development in the next five years. Fusion Technology, 30(1), Sep 1996.

- [104] P. W. Terry. Suppression of turbulence and transport by sheared flow. Reviews of Modern Physics, 72(1):109, Jan 2000.
- [105] P H Diamond, S-I Itoh, K Itoh, and T S Hahm. Zonal flows in plasmas a review. Plasma Physics and Controlled Fusion, 47(5):R35–R161, May 2005.
- [106] Akihide Fujisawa. A review of zonal flow experiments. Nuclear Fusion, 49(1):013001, Jan 2009.
- [107] S. Lundquist. Magneto-hydrostatic fields. Arkiv Fysik, 2(4):361365, 1950.
- [108] Walter M. Elsasser. Hydromagnetic dynamo theory. Reviews of Modern Physics, 28(2):135163, Apr 1956.
- [109] L. Woltjer. A theorem on force-free magnetic fields. Proceedings of the National Academy of Sciences of the United States of America, 44(6):489491, Jun 1958. PMID: 16590226, PMCID: PMC528606.
- [110] Michael R. Brown, Richard C. Canfield, and Alexei A. Editors Pevtsov, editors. Magnetic Helicity in Space and Laboratory Plasmas. American Geophysical Union, 2013.
- [111] J. B. Taylor. Relaxation of toroidal plasma and generation of reverse magnetic fields. Physical Review Letters, 33(19):11391141, Nov 1974.
- [112] Michael R. Brown. Experimental evidence of rapid relaxation to large-scale structures in turbulent fluids: selective decay and maximal entropy. Journal of Plasma Physics, 57(1):203229, Jan 1997.
- [113] S. Chandrasekhar and P. C. Kendall. On force-free magnetic fields. The Astrophysical Journal, 126:457, Sep 1957.
- [114] J. T. Slough, A. L. Hoffman, R. D. Milroy, E. A. Crawford, M. Cecik, R. Maqueda, G. A. Wurden, Y. Ito, and A. Shiokawa. Confinement and stability of plasmas in a field-reversed configuration. Physical Review Letters, 69(15):22122215, Oct 1992.
- [115] J. T. Slough, A. L. Hoffman, R. D. Milroy, R. Maqueda, and L. C. Steinhauer. Transport, energy balance, and stability of a large field-reversed configuration. Physics of Plasmas, 2:22862291, Jun 1995.
- [116] W. T. Armstrong. Field-reversed experiments (frx) on compact toroids. Physics of Fluids, 24(11):2068, 1981.
- [117] R. L. Morse and J. P. Freidberg. Rigid drift model of high-temperature plasma containment. Physics of Fluids (1958-1988), 13(2):531533, 1970.
- [118] Loren Steinhauer. Equilibrium rotation in field-reversed configurations. Physics of Plasmas (1994-present), 15(1):012505, Jan 2008.
- [119] Loren C. Steinhauer and T. P. Intrator. Equilibrium paradigm for field-reversed configurations and application to experiments. Physics of Plasmas, 16(7):072501, Jul 2009.

- [120] C. D. Cothran, A. Falk, A. Fefferman, M. Landreman, M. R. Brown, and M. J. Schaffer. Spheromak merging and field reversed configuration formation at the Swarthmore Spheromak Experiment. Physics of Plasmas (1994-present), 10(5):17481754, Apr 2003.
- [121] Y. Ono, H. Tanabe, T. Yamada, M. Inomoto, T. Ii, S. Inoue, K. Gi, T. Watanabe, M. Gryaznevich, R. Scannell, C. Michael, and C. Z. Cheng. Ion and electron heating characteristics of magnetic reconnection in tokamak plasma merging experiments. Plasma Physics and Controlled Fusion, 54(12):124039, Dec 2012.
- [122] Yasushi Ono. Slow formation of field-reversed configuration by use of two merging spheromaks. Fusion Technology, 27, Apr 1995.
- [123] M. Yamada, Y. Ono, A. Hayakawa, M. Katsurai, and F. W. Perkins. Magnetic reconnection of plasma toroids with cohelicity and counterhelicity. Physical Review Letters, 65(6):721724, Aug 1990.
- [124] S. P. Gerhardt, E. Belova, M. Inomoto, M. Yamada, H. Ji, Y. Ren, and A. Kuritsyn. Equilibrium and stability studies of oblate field-reversed configurations in the Magnetic Reconnection Experiment. Physics of Plasmas (1994-present), 13(11):112508, Nov 2006.
- [125] C. G. R. Geddes, T. W. Kornack, and M. R. Brown. Scaling studies of spheromak formation and equilibrium. Physics of Plasmas, 5(4):1027, 1998.
- [126] Cameron Geddes. Spheromak equilibrium studies on SSX. Senior honors thesis, Swarthmore College, 1997.
- [127] Michael J. Schaffer. Exponential Taylor states in circular cylinders. Physics of Fluids, 30(1):160, 1987.
- [128] M G Rusbridge, S J Gee, P K Browning, G Cunningham, R C Duck, A al Karkhy, R Martin, and J W Bradley. The design and operation of the SPHEX spheromak. Plasma Physics and Controlled Fusion, 39(5):683–714, May 1997.
- [129] E. B. Hooper, R. H. Bulmer, B. I. Cohen, D. N. Hill, C. T. Holcomb, B. Hudson, H. S. McLean, L. D. Pearlstein, C. A. Romero-Talams, C. R. Sovinec, B. W. Stallard, R. D. Wood, and S. Woodruff. Sustained Spheromak Physics Experiment (SSPX): design and physics results. Plasma Physics and Controlled Fusion, 54(11):113001, November 2012.
- [130] Thomas W. Kornack. Magnetic reconnection studies on SSX. Senior honors thesis, Swarthmore College, 1998.
- [131] M. R. Brown. Private communication, 2010.
- [132] J. C. Thomas, D. Q. Hwang, R. D. Horton, J. H. Rogers, and R. Raman. A simple fast pulse gas valve using a dynamic pressure differential as the primary closing mechanism. Review of Scientific Instruments, 64(6):14101413, Jun 1993.
- [133] S. E. Wurzel. Parker valve characterization. Internal report, 2006.
- [134] W. Rogowski and W. Steinhaus. Die messung der magnetischen spannung. Archiv fr Elektrotechnik, 1(4):141–150, April 1912.

- [135] Kenneth L. Kaiser. Electromagnetic Compatibility Handbook. CRC Press, Boca Raton, 2005.
- [136] Kyu-Sun Chung. Mach probes. Plasma Sources Science and Technology, 21(6):063001, Dec 2012.
- [137] X. Zhang, D. Dandurand, T. Gray, M. R. Brown, and V. S. Lukin. Calibrated cylindrical mach probe in a plasma wind tunnel. Review of Scientific Instruments, 82(3):033510, Mar 2011.
- [138] I. H. Hutchinson. The invalidity of a mach probe model. Physics of Plasmas (1994-present), 9(5):18321833, Apr 2002.
- [139] Charles Lee Ellison. Multi-channel CO_2 interferometer diagnostic for the Colorado FRC experiment. Senior honors thesis, University of Colorado Boulder, 2009.
- [140] A. R. Jacobson. Heterodyne quadrature interferometer for simultaneous measurements of plasma density along several chords. Review of Scientific Instruments, 49(5):673–674, May 1978.
- [141] Jongsoo Yoo, Masaaki Yamada, Hantao Ji, and Clayton E. Myers. Observation of ion acceleration and heating during collisionless magnetic reconnection in a laboratory plasma. Physical Review Letters, 110(21):215007, May 2013.
- [142] D. J. Drake, J. W. R. Schroeder, G. G. Howes, C. A. Kletzing, F. Skiff, T. A. Carter, and D. W. Auerbach. Alfvén wave collisions, the fundamental building block of plasma turbulence. IV. laboratory experiment. Physics of Plasmas, 20(7):072901, 2013.
- [143] T. Munsat, C. L. Ellison, A. Light, and J. Nuger. The Colorado FRC Experiment. J Fusion Energy, 27:82–86, 2008.
- [144] C. A. Romero-Talamás, P. M. Bellan, and S. C. Hsu. Multielement magnetic probe using commercial chip inductors. Review of Scientific Instruments, 75(8):2664–2667, August 2004.
- [145] Christian M. Franck, Olaf Grulke, and Thomas Klinger. Magnetic fluctuation probe design and capacitive pickup rejection. Review of Scientific Instruments, 73(11):3768, 2002.
- [146] D. Kumar, A.L. Moser, and P.M. Bellan. Energy efficiency analysis of the discharge circuit of Caltech spheromak experiment. IEEE Transactions on Plasma Science, 38(1):4752, Jan 2010.
- [147] M. R. Brown, D. M. Cutrer, and P. M. Bellan. Motion and equilibrium of a spheromak in a toroidal flux conserver. Physics of Fluids B: Plasma Physics (1989-1993), 3(5):11981213, May 1991.
- [148] E. V. Stenson and P. M. Bellan. Magnetically driven flows in arched plasma structures. Physical Review Letters, 109(7):075001, Aug 2012.
- [149] S. J. Levinson, S. B. Kim, T. Koh, and E. J. Powers. Plasma fluctuation diagnostics via maximum entropy spectral estimation. Review of Scientific Instruments, 59(8):1754–1756, Aug 1988.

- [150] E. J. Powers, H. S. Don, J. Y. Hong, Y. C. Kim, G. A. Hallock, and R. L. Hickok. Spectral analysis of nonstationary plasma fluctuation data via digital complex demodulation. Review of Scientific Instruments, 59(8):1757–1759, Aug 1988.
- [151] N. Wu. The Maximum Entropy Method. Springer-Verlag, Berlin, 1997.
- [152] Ira Bernstein. Waves in a plasma in a magnetic field. Physical Review, 109(1):10–21, 1958.
- [153] A.P.H. Goede, P. Massmann, H.J. Hopman, and J. Kistemaker. Ion bernstein waves excited by an energetic ion beam in a plasma. Nuclear Fusion, 16(1):85–96, February 1976.
- [154] H. Böhmer. Excitation of ion cyclotron harmonic waves with an ion beam of high perpendicular energy. Physics of Fluids, 19(9):1371, 1976.
- [155] P. M. Kintner. On the distinction between electrostatic ion cyclotron waves and ion cyclotron harmonic waves. Geophysical Research Letters, 7(8):585–588, August 1980.
- [156] H. E. J. Koskinen, P. M. Kintner, G. Holmgren, B. Holback, G. Gustafsson, M. Andre, and R. Lundin. Observations of ion cyclotron harmonic waves by the viking satellite. Geophysical Research Letters, 14(4):459–462, April 1987.
- [157] Dingyi Li, Deyu Wand, Shihtung Tsai, Minjian Xu, and Dingyi Mao. Ion-cyclotron instability and electron acceleration in coronal loops. Solar Physics, 143(2):235–245, February 1993.
- [158] Michiaki Inomoto, Akihiro Kuwahata, Hiroshi Tanabe, Yasushi Ono, and T. S. Group. Excitation and propagation of electromagnetic fluctuations with ion-cyclotron range of frequency in magnetic reconnection laboratory experiment. Physics of Plasmas (1994-present), 20(6):061209, June 2013.
- [159] John J. Podesta. The need to consider ion bernstein waves as a dissipation channel of solar wind turbulence. Journal of Geophysical Research, 117(A7), July 2012.
- [160] Christopher Torrence and Gilbert P. Compo. A practical guide to wavelet analysis. Bulletin of the American Meteorological Society, 79(1):6178, Jan 1998.